Bernhard Wedl

Structure and Morphology
of
Dihexyl-terthiophene Thin Films

MASTER THESIS

For obtaining the academic degree
Diplom-Ingenieur

Diploma Programme of
Technical Physics

TU Graz
Graz University of Technology
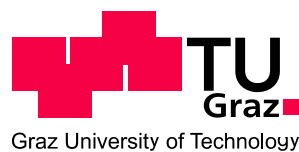
Graz University of Technology

Supervisor:

a.o. Univ-Prof. Dr. Roland Resel

Institute of Solidstate Physics

Graz, October 2010

» The ultimate proof of theory is experiment[1] «

---
[1] Richard Phillips Feynman

Acknowledgments

Abstract

The formation of polymorph crystal structures of the molecule dihexyl-terthiophene is investigated within thin films. Different thin film preparation methods were used: on one hand films are prepared by solution processing: spin-coating and drop-casting. The films are investigated in terms of their crystallographic structure and thin film morphology by different x-ray scattering and microscopy methods. Three different types of polymorph crystal structures are found. Their appearance depends on the thin film preparation method. The evaporation rate of the solvent during the crystallisation process determines which type of phase is prefered. In case of a slow crystallisation process two different stable bulk structures are formed, which also grow by crystallisation from the melt. One of these stable bulk structures is fully solved by single crystal X-ray diffraction. In case of a fast crystallisation process a specific phase appears. This phase is metastable, since it is formed under non-equilibrium conditions. The formation of the metastable phase is studied starting from the monolayer coverage: highly aligned crystallites grow on top of a closed monolayer which acts as a template for the subsequent crystal growth. This reveals that the metastable phase is mediated by the presence of a surface during the crystallisation process.

Kurzfassung

Diese Arbeit beschäftigt sich mit der Entstehung von polymorphen Kristallstrukturen des Moleküls Dihexyl-terthiophene in dünnen Filmen. Zwei Herstellungsmethoden wurden angewandt. DROPCASTING und SPINCOATING. Die Filme wurden hinsichtlich ihrer kristallographischen Struktur mittels Röntgenstreuungsexperimente und ihre Morpholgie durch mikroskopischen Methoden untersucht.

Drei verschiedene kristalline Polymorphe wurden gefunden. Die Untersuchungen ergaben dass die resultierende Phase von der Herstellungmethode abhängig ist. Im Speziellen von der Verdampfungsrate des Lösungsmittels während des Kristallisationsvorganges. Diese bestimmt welche der drei Phasen bevorzugt entsteht. Im Falle einer sehr langsamen Verdampfung des Lösungsmittels treten bevorzugt zwei als BULK-Strukturen titulierte Phasen auf. Zusätzlich entstehen diese beiden auch bei der Kristallisation aus der Schmelze und werden daher als thermodynamisch stabil behandelt. Bei sehr schneller Verdampfung des Lösungsmittels tritt eine spezielle Phase auf. Da sie nicht unter Bedingungen im thermodynamischen Gleichgewicht entsteht wird sie als metastabil angesehen. Die Entstehung dieser metastabilen Phase wurde ausgehend von einer Monolage bis zu größeren Schichtdicken untersucht. Die experimentellen Ergebnisse implizieren, dass zuerst eine Monolage ausgebildet wird. Auf dieser wachsen weitergehend sehr gut ausgerichtete Kristallite mit hoher Qualität. Es wird angenommen dass das Vorhanden sein einer Oberfläche und/oder die Geschwindigkeit der Kristallisation das Kriterium für die Entstehung dieser Phase ist.

III

Contents

Chapter 1

Basics of X-ray diffraction experiments

X-rays are electromagnetic waves which, since their discovery in 1895 by Wilhelm Röntgen, are used in a variety of applications ranging from medicine and security over lithography on to material science and many others. The energy of X-rays is typically in the range of 120 eV to 120 keV, which corresponds to a wavelength range of $0.01\,nm$ to $10\,nm$. At these high energies, electromagnetic waves are relatively weakly interacting with matter, allowing them to penetrate several mm to cm into solid materials. This low adsorption coefficient for X-rays is exploited in transmission experiments like medical X-ray or computer tomography. The ability of X-rays to be diffracted, as first discovered by MAX VON LAUE, allows an even deeper insight into material properties with a resolution as small as the atomic scale, e.g., the double-helix arrangement of the acid-base pairs in DNA as one of the most important results.

In this work, the results of X-ray diffraction experiments performed at a variety of experimental setups are used to elucidate the internal and crystal structure of the molecule *DH3T*. In the next sections, a brief summary of the theory of diffraction experiments together with the experimental setups will be given. For more detailed explanations of the theoretical description of X-ray diffraction and its application see for instance [25][4][18][1].

1.1   The Direct Lattice and its Unit Cell

Many materials are crystalline in their soldid state, i.e., they consist of more or less "*periodic repetitions in three dimensions of a motive composed of atoms* [25]". Most experiments with X-rays are using this periodic property of the solid. This part will give a brief introduction to how an ideal crystal is described [7].

1.1.1   The Lattice

The direct lattice consisting of atoms or molecules is a periodic repetition of a property $f(\mathbf{r}) = f(\mathbf{r} + \mathbf{R_n})$ and can be described as a linear combination of a set of basis vectors a_1, a_2, a_3 in real space. In general, we are dealing with non-unitary systems. The lattice points $\mathbf{R}_n$ represent this latice

$$\mathbf{R_n} = \sum_i n_i \mathbf{a_i} \tag{1.1}$$

$n = (n_1, n_2, n_3)$ is a triple of integers. The basis vectors can be varied in multiple ways to describe the same lattice and, therefore, a *unit cell* is defined as the set of a_i with the smallest volume

$$\mathbf{V_{UC}} = \mid \mathbf{a_1} \ (\mathbf{a_2} \times \mathbf{a_3}) \mid \tag{1.2}$$

These unit cells can be categorized in *crystal systems* and BRAVAIS *lattices* with specific properties and are discussed in detail in literature [25][7].
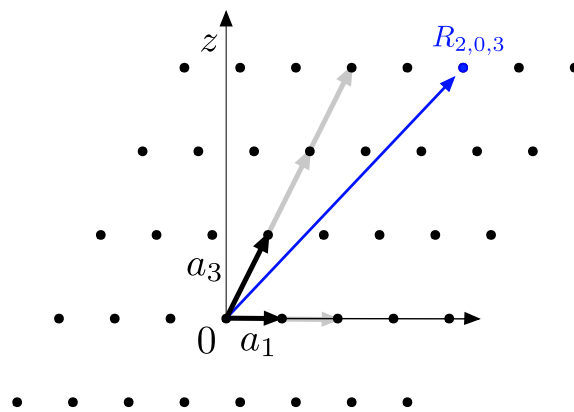
Figure 1.1: lattice point $2a_1$, a_2, $3a_3$ view along a_2
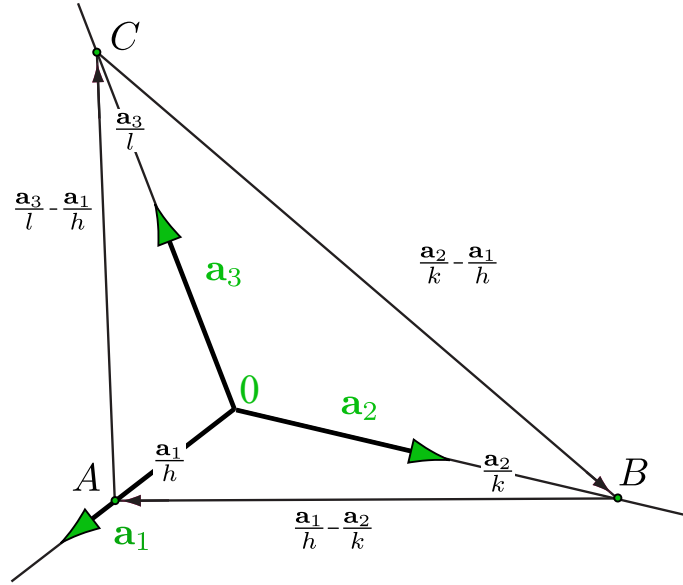
Figure 1.2: A lattice plane described by $h \cdot u + k \cdot v + l \cdot w = 1$ in a non-unitary system

1.1.2 Lattice Planes

A plane generally can be represented by 3 points not lying on the same line. Within the lattice, planes can be identified by its axis intersections in multiples of $\mid \mathbf{a}_i \mid$. For unitary and non-unitary systems, equation. 1.3 defines a plane where the reciprocal values of the h, k, l (MILLER indices) are the distances from the origin to the intersections with the according axis (A, B, C) in units of $\mathbf{a}_i$ (figure 1.2)[25]. The length from 0 to A, for example, is $\mathbf{a}_1/h$.

$$h \cdot u + k \cdot v + l \cdot w = 1 \tag{1.3}$$

The normal vector to the plane can be calculated from the vector product

$$
\begin{aligned}
\mathbf{N} &= (sign\,of\,hkl)\left[\left(\frac{\mathbf{a}_1}{h} - \frac{\mathbf{a}_2}{k}\right) \times \left(\frac{\mathbf{a}_2}{k} - \frac{\mathbf{a}_3}{l}\right)\right] \\
&= \left(\frac{\mathbf{a}_1 \times \mathbf{a}_2}{hk}\right) - \left(\frac{\mathbf{a}_2 \times \mathbf{a}_2}{kk}\right) - \left(\frac{\mathbf{a}_1 \times \mathbf{a}_3}{hl}\right) + \left(\frac{\mathbf{a}_2 \times \mathbf{a}_3}{kl}\right) \\
&= \left\{\left(\frac{\mathbf{a}_2 \times \mathbf{a}_3}{kl}\right) + \left(\frac{\mathbf{a}_3 \times \mathbf{a}_1}{hl}\right) + \left(\frac{\mathbf{a}_1 \times \mathbf{a}_2}{hk}\right)\right\} \\
&= \frac{1}{\mid hkl \mid} \left\{h(\mathbf{a}_2 \times \mathbf{a}_3) + k(\mathbf{a}_3 \times \mathbf{a}_1) + l(\mathbf{a}_1 \times \mathbf{a}_2)\right\}
\end{aligned}
$$

and the length $|\mathbf{N}|$ of the normal vector $\mathbf{N}$ is [25]

$$|\mathbf{N}| \;=\; \frac{1}{d}\frac{\mathbf{V_{UC}}}{|\,hkl\,|}$$

with d as the shortest distance from the origin to the plane. We therefore have a unit vector pointing from the origin towards the plane of

$$\hat{\mathbf{n}} \;=\; d\left\{h\frac{(\mathbf{a_2}\times\mathbf{a_3})}{\mathbf{V_{UC}}} + k\frac{(\mathbf{a_3}\times\mathbf{a_1})}{\mathbf{V_{UC}}} + l\frac{(\mathbf{a_1}\times\mathbf{a_2})}{\mathbf{V_{UC}}}\right\}$$

In a more compact formulation

$$
\begin{aligned}
\hat{\mathbf{n}} &= d\,\mathbf{r}^* \\
\mathbf{r}^* &= h\frac{(\mathbf{a_2}\times\mathbf{a_3})}{\mathbf{V_{UC}}} + k\frac{(\mathbf{a_3}\times\mathbf{a_1})}{\mathbf{V_{UC}}} + l\frac{(\mathbf{a_1}\times\mathbf{a_2})}{\mathbf{V_{UC}}} \qquad (1.4) \\
|\,\mathbf{r}^*\,| &= \frac{1}{d} \qquad\qquad\qquad\qquad\qquad\qquad\qquad\qquad (1.5)
\end{aligned}
$$

So we have three important results:

1. A lattice plane is described by 3 MILLER indices (hkl)

2. The vector $\mathbf{r}^*$ is perpendicular to the defined lattice plane (hkl)

3. The length $|\,\mathbf{r}^*\,|$ of the vector is the reciprocal value of the lattice-plane spacing

$$|\,\mathbf{r}^*\,| \;=\; \frac{1}{d}$$

Figure 1.3 shows this schematically.

1.2 The Reciprocal Lattice

Beside the real lattice, a reciprocal lattice can be defined as (cf. eq. 1.4):
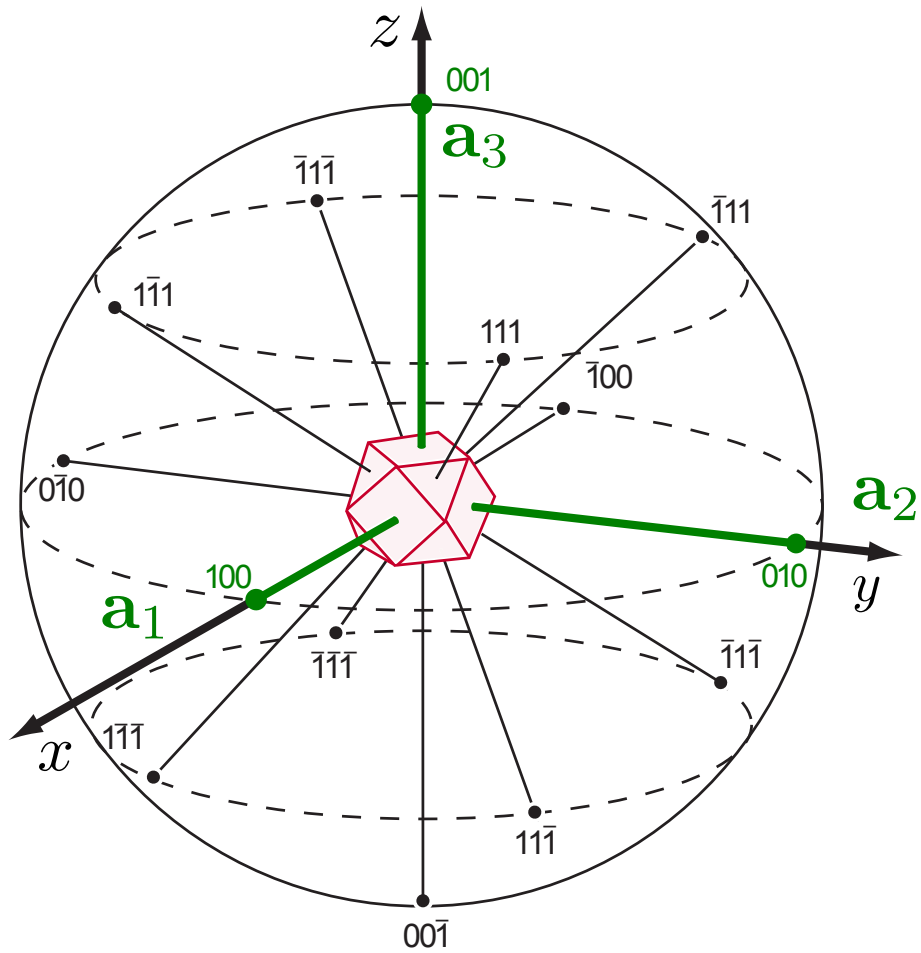
Figure 1.3: The hkl directions of a cubic crystal structure ($\mid a_1 \mid = \mid a_2 \mid = \mid a_3 \mid$ and 90° between them). The normal vectors of all sketched planes in this figure are intersected with the unit sphere for simplicity.

$$\mathbf{R}_m^* \;=\; \sum_i m_i \mathbf{a_i^*} \tag{1.6}$$

The reciprocal basis vectors a_i^* are defined as:

$$\begin{aligned}
\mathbf{a}_1^* &= \frac{2\pi}{V_{UC}}\,(\mathbf{a}_2 \times \mathbf{a}_3) \\
\mathbf{a}_2^* &= \frac{2\pi}{V_{UC}}\,(\mathbf{a}_3 \times \mathbf{a}_1) \\
\mathbf{a}_3^* &= \frac{2\pi}{V_{UC}}\,(\mathbf{a}_1 \times \mathbf{a}_2)
\end{aligned}$$

and the reciprocal cell volume is simply:

$$\mathbf{V_{rUC}} = \frac{2\pi}{\mathbf{V_{UC}}} \tag{1.7}$$

The two systems are orthogonal and, consequently

$$\mathbf{a}_i \mathbf{a}_j^* \;=\; 2\pi\,\delta_{ij} \tag{1.8}$$

The reciprocal vector $\mathbf{Q}$

$$\mathbf{Q} \;=\; h\,\mathbf{a}_1^* + k\,\mathbf{a}_2^* + l\,\mathbf{a}_3^*$$

is perpendicular to a set of parallel lattice planes of the direct lattice and unambiguously describes this family:

$$\hat{\mathbf{n}} \;=\; \frac{d}{2\pi}\,\mathbf{Q}$$

$$d \;=\; \frac{2\pi}{|\,\mathbf{Q}\,|} \tag{1.9}$$

$\hat{\mathbf{n}}$ is the unit vector perpendicular to a set of lattice planes and d is the distance between the lattice planes. This is schematically shown in figure 1.4.
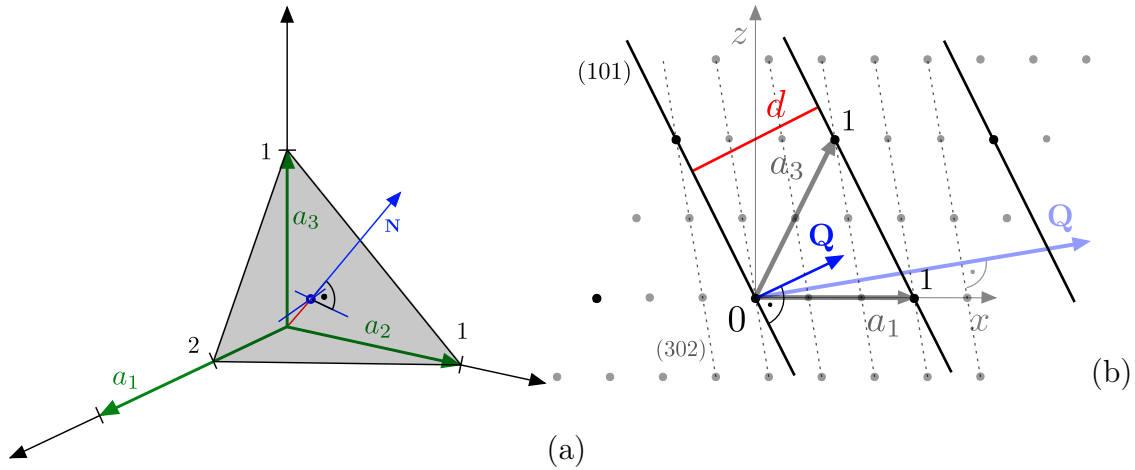
Figure 1.4: (a) A lattice plane defined by $(2, 1, 1)$. (b) Lattice-plane families $(1\,0\,1)$ and $(3\,0\,2)$; view along a_2.

1.3 X-ray Scattering and Diffraction

The electric field of an X-ray beam traveling through vaccum is described as:

$$\mathbf{E}(\mathbf{r}) = \mathbf{E_0} \cdot e^{i(\mathbf{kr} - \omega t)} \tag{1.10}$$

and it is the transversal component of an electromagnetic wave. It is the mainly interacting part with the lattice [29]. $\mathbf{E_0}$ is the electrical field, k is the wave vector, ω the angular frequency. During the experiment, the detector measures an intensity $I \sim \mid E'(\mathbf{r}) \mid^2$ so the time-depending factor is neglected in the following steps. The length of the wave vector is

$$k = |\mathbf{k}| \quad = \quad \frac{\omega}{c}$$

and is called the *wave number*, which is connected to the wavelength λ via

$$k \quad = \quad \frac{2\pi}{\lambda}$$

Therefore, $\mathbf{k}$ can be separated in a unit vector $\mathbf{s}$, which defines its direction, and its length k.

$$\mathbf{k} \quad = k \cdot \mathbf{s} = \quad \frac{2\pi}{\lambda} \cdot \mathbf{s}$$

The photon energy is given by

$$E[keV] = \frac{h \cdot c}{\lambda} = \frac{12.398}{\lambda[\text{Å}]}$$

The electric field of the X-rays can interact with electrons, force them to oscillate, and therefore to radiate an electromagnetic spherical wave. If no energy transfer occurs (elastic or *Thomson scattering*), an electromagnetic wave with the same wavelength as the incoming electromagnetic field is generated. So $\mid \mathbf{k} \mid = \mid \mathbf{k}' \mid$ and $\mid \omega \mid = \mid \omega' \mid$.

The origin $\hat{r} = 0$ is set somewhere within an atom described by his electronic density $\rho(\hat{r})$. The field E' at an observation point $\mathbf{r}'$ is a superposition of contributions from different scattering centers and is proportional to (fig. 1.5(a)) :

$$E'\left(\mathbf{r}'\right) \quad \sim \quad -r_0 \int d^3\hat{r}\, \rho(\hat{r})\, e^{i\Delta\phi(\mathbf{r}')} \tag{1.11}$$

r_0 is the *Thomson scattering length* [1].

The phase factor $e^{i\Delta\phi(\mathbf{r}')}$ is important for constructive interference and is different for every scattering center. It is defined by the position of the scattering center $\hat{r}$ and the direction of the wave vectors $\mathbf{s}$ and $\mathbf{s}'\left(\mathbf{r}', \hat{r}\right)$ (fig. 1.5(b)) When setting the observation point to infinity so the $\mathbf{s}'\left(\mathbf{r}', \hat{r}\right) = \mathbf{s}'$ get parallel (Frauenhofer approximation) the phase factor is

$$\Delta\phi \quad = \quad \frac{2\pi}{\lambda}\left(\mathbf{s}' - \mathbf{s}\right)\hat{r} = \frac{2\pi}{\lambda}\,\mathbf{S}\,\hat{r} = \left(\mathbf{k}' - \mathbf{k}\right)\hat{r} = \mathbf{q} \cdot \hat{r}$$

and equation 1.11 denotes to

$$E'(\mathbf{q}) \quad \sim \quad -r_0 \int d^3\hat{r}\, \rho(\hat{r})\, e^{i\,\mathbf{q}\hat{r}} \tag{1.12}$$

The *scattering vector* $\mathbf{q}$ (momentum transfer) is defined as

$$\hbar\mathbf{q} = \hbar\mathbf{k}' - \hbar\mathbf{k} \tag{1.13}$$

where $\hbar\mathbf{k}$ and $\hbar\mathbf{k}'$ are the initial and final momenta of the photon .

For describing the whole lattice one has to sum up all contributing scattering centers and keep track of the phase $e^{i\Delta\phi_c(\hat{r})}$ of the incident wave as it interacts with the scattering center.

$$E'(\mathbf{q}) \quad \sim \quad -r_0 \int_{V_c} d^3\hat{r}\, \rho(\hat{r})\, e^{i\,\mathbf{q}\hat{r}}\, e^{i\Delta\phi_c(\hat{r})} \tag{1.14}$$

Where V_c is the volume of the whole lattice.
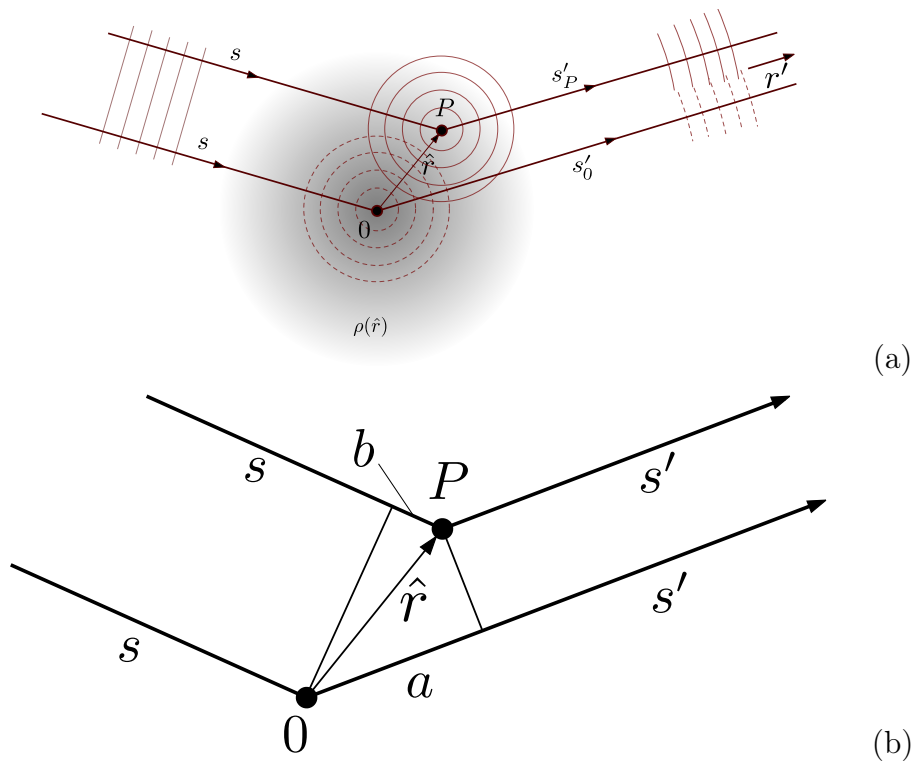
Figure 1.5: (a) Illustration of superposition of the scattered waves. (b) Illustration of interference. When assuming the scattered waves meet in infinity, they are parallel (Frauenhofer approximation). Then the path difference between $\mathbf{s}'$ scattered by 0 and P is $a - b = \hat{r}\left(\mathbf{s}' - \mathbf{s}\right)$.
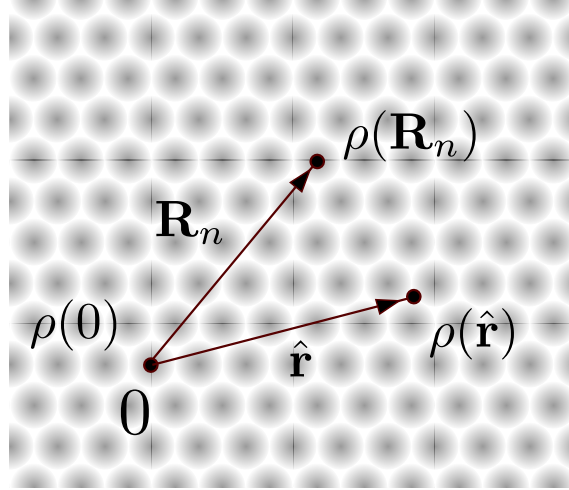
Figure 1.6: The gray spots symbolize the $\mathbf{R_n}$-periodic $\rho(\hat{r})$ proportional to the electronic density around an atom. The wave amplitude at points $\mathbf{R_n}$ relative to the same origin equal; i.e. $\rho(0) = (\mathbf{R_n})$ or in general $\rho(\hat{r}) = \rho(\hat{r} + \mathbf{R_n})$ respectively. 2 Points at positions $\hat{r}$ do not equal in general instead.

As mentioned above in section 1.1 a crystal per definition is a defined arrangement of a periodic property like $\rho(\hat{r})$, i.e. those $\rho(\hat{r})$ are the same for any $\hat{r} + \mathbf{R_n}$ (fig. 1.6(a)) . Note that all $\rho(\hat{r})$ are therefore represented within only one unit cell. Equation 1.12 subsequently can be written as

$$E'(\mathbf{q}) \sim \sum_{\mathbf{R_n}} \left\{ -r_0 \int_{V_{uc}} d^3\hat{r}_{uc}\, \rho(\hat{r}_{uc})\, e^{i\,\mathbf{q}\hat{r}} \right\} e^{i\,\mathbf{q}\,\mathbf{R_n}}$$

$$E'(\mathbf{q}) \sim \underbrace{-r_0 \int_{V_{uc}} d^3\hat{r}\, \rho(\hat{r}_{uc})\, e^{i\,\mathbf{q}\hat{r}}}_{structur\ factor} \underbrace{\sum_{\mathbf{R_n}} e^{i\,\mathbf{q}\,\mathbf{R_n}}}_{lattice\ sum}$$

The structure factor $f_S(\mathbf{q})$ in detail is irrelevant as long as we only consider the theoretical directions of the maximal intensity and not the absolute value of scattered intensity. So the integral denotes to a constant and a sum over all $\mathbf{R_n}$ within the crystal.

Now $E'(\mathbf{q})$ is:

$$E'(\mathbf{q}) = f_S(\mathbf{q}) \sum_{\mathbf{R_n}} e^{i\,\mathbf{q}\cdot\mathbf{R_n}}$$

$$= f_S(\mathbf{q}) \sum_{n_1} e^{i\,n_1(\mathbf{q}\,\mathbf{a_1})} \cdot \sum_{n_2} e^{i\,n_2(\mathbf{q}\,\mathbf{a_2})} \cdot \sum_{n_3} e^{i\,n_3(\mathbf{q}\,\mathbf{a_3})} \qquad (1.15)$$

Constructive interference occurs when the phase difference is a multiple of 2π. Therefore, the following equations, called LAUE equations, have to be fullfilled. The $\left(\hat{h}, \hat{k}, \hat{l}\right)$ denote the order of the diffraction maxima and are called LAUE indices.

$$\mathbf{a}_1 \cdot \mathbf{q} = 2\pi \cdot \hat{h} \tag{1.16}$$

$$\mathbf{a}_2 \cdot \mathbf{q} = 2\pi \cdot \hat{k} \tag{1.17}$$

$$\mathbf{a}_3 \cdot \mathbf{q} = 2\pi \cdot \hat{l} \tag{1.18}$$

When choosing $\mathbf{q}$ as any of the $\mathbf{Q}$ defined in subsection 1.2, one automatically gets constructive interference due to the fact that

$$\mathbf{a}_i \mathbf{a}_j^* = 2\pi \, \delta_{ij} \tag{1.19}$$

So equation 1.15 can be rewritten as

$$
\begin{aligned}
E'(\mathbf{Q}) &= f_S(\mathbf{q}) \sum_n e^{i\,\mathbf{Q}\mathbf{R_n}} \\
&= f_S(\mathbf{q}) \sum_{n_1} e^{i\,n_1 h\left(\mathbf{a}_1^* \mathbf{a_1}\right)} \cdot \sum_{n_2} e^{i\,n_2 k\left(\mathbf{a}_2^* \mathbf{a_2}\right)} \cdot \sum_{n_3} e^{i\,n_3 l\left(\mathbf{a}_3^* \mathbf{a_3}\right)}
\end{aligned}
\tag{1.20}
$$

and the exponents of the phase factors are

$$\mathbf{a}_1 \cdot \mathbf{Q} = 2\pi \cdot h \tag{1.21}$$

$$\mathbf{a}_2 \cdot \mathbf{Q} = 2\pi \cdot k \tag{1.22}$$

$$\mathbf{a}_3 \cdot \mathbf{Q} = 2\pi \cdot l \tag{1.23}$$

I.e., the reciprocal lattice is a mapping of the direct lattice.

The MILLER and LAUE indices just differ in a factor n;

$$\left(\hat{h}, \hat{k}, \hat{l}\right) = n\,(h, k, l)$$

So we have three important results:

1. In a diffraction experiment *the scattering vector has to simultaneously equal in length and direction a reciprocal lattice vector* to observe enhanced intensity

$$\mathbf{q} = \mathbf{Q}$$

2. The peak maximum occurs when the scattering vector $\mathbf{q}$ is perpendicular to a lattice plane (hkl)

3. The length $|\mathbf{Q}|$ of the vector is the reciprocal value of the lattice-plane spacing

$$d \;=\; \frac{2\pi}{|\mathbf{Q}|}$$

1.3.1 Slit Interference Function

Another interesting result deriving from the lattice sum is the so called slit inter-ference function that describes the scattered intensity around a crystal Bragg peak and writes as [4]:

$$I(\mathbf{q}) = \frac{sin^2(N_1 a_1 \mathbf{q}/2)}{sin^2(a_1 \mathbf{q}/2)} \cdot \frac{sin^2(N_2 a_2 \mathbf{q}/2)}{sin^2(a_2 \mathbf{q}/2)} \cdot \frac{sin^2(N_3 a_3 \mathbf{q}/2)}{sin^2(a_3 \mathbf{q}/2)} \tag{1.24}$$

with N_i as the lattice extension in the i-th direction (in numbers of unit cells). The formula reveals two important results. First, strong maxima at $|\mathbf{q}| = |\mathbf{Q}| = \frac{n*2\pi}{a_i}$ which correspond to Bragg peaks. Second, side maxima around strong maxima occur (*Laue oscillations*). These side maxima are, in general, observable only for high quality crystals and allow for an accurate determination of the crystal extension. Figure 1.7 shows a simulation of the slit interference function.
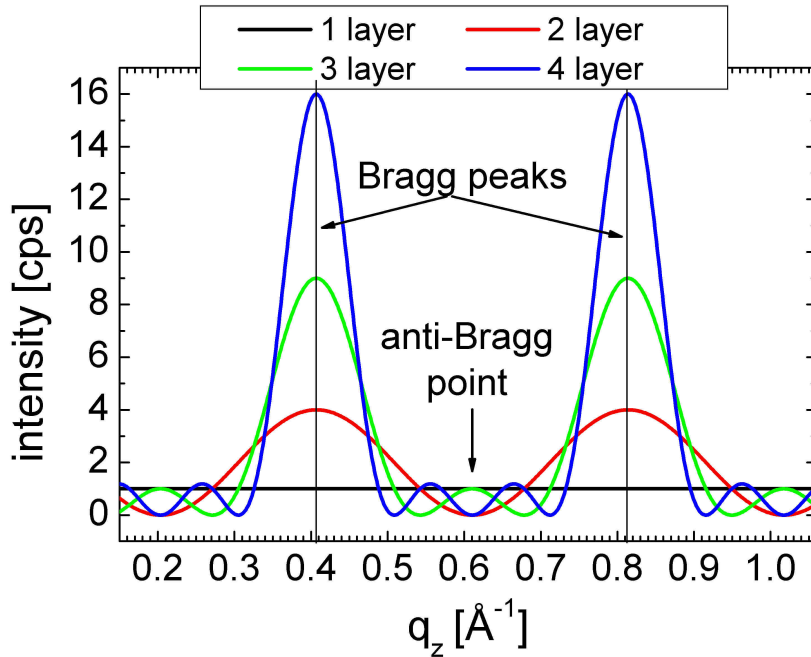
Figure 1.7: Peak simulation of multilayer arising from a crystal with a d-spacing of 15.4 Å The peak positions remain the same and are independent of the layer thickness. As the number of layers increases, the full width at half maximum is reduced and the number of Laue oscillations in between the Bragg peaks increases. Image reproduced from [31]

1.4 Geometric Considerations

The incident wave vector $\mathbf{k_0}$ in most experimental setups is fixed and the detector and the sample are shifted and rotated to adjust the crystals to fulfill the Laue condition. We choose a coordinate system in a way that $\mathbf{k_0}$ is along the x-axis (1). We call it the laboratory system. So $\mathbf{k}_0^{\mathrm{L}}$ in the laboratory system is given by

$$\mathbf{k}_0^{\mathrm{L}} \quad = \quad \frac{2\pi}{\lambda}(1,0,0) \tag{1.25}$$

The detector rotates on two axes to scan for scattered waves. The rotation axis $\underset{1}{\mathbf{A}} = (0,1,0)$ of Θ_1 is the y-axis (2) and $\underset{2}{\mathbf{A}} = (0,0,1)$ for Θ_2 is the z-axis (3). The starting position of the detector is set in a way that $\Theta_1 = \Theta_2 = 0$. In that case $\mathbf{k}^{\mathrm{L}}$ is

$$\mathbf{k}^{\mathrm{L}} \quad = \quad \frac{2\pi}{\lambda}(1,0,0) \tag{1.26}$$

and the detector is on a vector in direction $\mathbf{d}^0 = (1,0,0)$. The mathematical description of a clockwise rotation by an angle Θ around a given axis $\mathbf{A}$ is given by [26]:

$$D_{ij}\left(\Theta, \mathbf{A}\right) \quad = \quad A_i A_j \left(1 - \cos\Theta\right) + \delta_{ij}\cos\Theta + \epsilon_{ipj}A_p sin\Theta \tag{1.27}$$

$$D\left(\Theta, \mathbf{A}\right) \quad = \quad \begin{pmatrix} (A_1)^2\left(1-\cos\Theta\right)+\cos\Theta & A_1 A_2\left(1-\cos\Theta\right)+A_3\sin\Theta & A_1 A_3\left(1-\cos\Theta\right)-A_2\sin\Theta \\ A_2 A_1\left(1-\cos\Theta\right)-A_3\sin\Theta & (A_2)^2\left(1-\cos\Theta\right)+\cos\Theta & A_2 A_3\left(1-\cos\Theta\right)+A_1\sin\Theta \\ A_3 A_1\left(1-\cos\Theta\right)+A_2\sin\Theta & A_3 A_2\left(1-\cos\Theta\right)-A_1\sin\Theta & (A_3)^2\left(1-\cos\Theta\right)+\cos\Theta \end{pmatrix}$$

When rotating the detector arm by Θ_1 we are observing for a wave in direction of

$$\mathbf{k}^{\mathrm{L}} \quad = \quad D_1\left(\Theta_1, \underset{1}{\mathbf{A}}\right) \cdot \frac{2\pi}{\lambda} \cdot \mathbf{d}^0$$

When rotating the detector arm by Θ_1 and Θ_2, we are observing a wave with

$$\mathbf{k}^{\mathrm{L}} \;=\; \left[\prod_{n=m_1 \ldots m_2} D_n\left(\Theta_n, \underset{n}{A}\right) \right] \cdot \mathbf{d}^0 \tag{1.28}$$

$$=\; D_{m_1}\left(\Theta_{m_1}, \underset{m_1}{\mathbf{A}}\right) D_{m_2}\left(\Theta_{m_2}, \underset{m_2}{\mathbf{A}}\right) \cdot \frac{2\pi}{\lambda} \cdot \mathbf{d}^0$$

$$\mathbf{m} \;\overset{\wedge}{=}\; \{m_1, m_2\}$$

In a more compact version the resulting rotation matrix Λ for M axes is

$$\Lambda\left(\mathbf{\Theta}, \mathbf{A}, \mathbf{m}\right) \;=\; \prod_{n=m_1, \ldots, m_M} D_n\left(\Theta_n, \underset{n}{A}\right) \tag{1.29}$$

$$\Lambda\left(\mathbf{\Theta}\right) \;=\; \Lambda\left(\mathbf{\Theta}, \mathbf{A}, \mathbf{m}\right)$$

$$\mathbf{\Theta} \;=\; \{\Theta_1, \ldots, \Theta_n, \ldots, \Theta_M\}$$

$$\mathbf{A} \;=\; \left\{\underset{1}{\mathbf{A}}, \ldots, \underset{n}{\mathbf{A}}, \ldots, \underset{M}{\mathbf{A}}\right\}$$

$$\mathbf{m} \;=\; \{m_1, \ldots, m_i, \ldots, m_M\}$$

and rembering the axes configuration

$$\Lambda\left(\mathbf{\Theta}\right) \;=\; \Lambda\left(\mathbf{\Theta}, \mathbf{A}, \mathbf{m}\right)$$

The rotations are not commutative, which means that it matters how the M rotation axes are coupled. The order has to be taken into account. $\mathbf{m}$ is a list which defines the order of the rotations. From right to left; axis m_M is mounted on axis m_{M-1}, is mounted on axis m_{M-2}, is mounted on .... . In the case of $\mathbf{m}$ is $\{1, 2\}$ the rotation axes $\underset{2}{\mathbf{A}}$ gets tilted for Θ_1. So when rotating by Θ_2, the detector is moving on a circle on the rotation sphere towards $(0, 1, 0)$ (figure 1.8) . When rotating by Θ_2 in the case $\mathbf{m} = \{2, 1\}$, we get a horizontal circle with constant height. Figure 1.9(a) shows the principle of the rotation for the case $\mathbf{m} = \{2, 1\}$,$\underset{1}{\mathbf{A}} = (0, 1, 0)$,$\underset{2}{\mathbf{A}} = (0, 0, -1)$. The scattering vector is $\mathbf{q}^{\mathrm{L}} = \mathbf{k}^{\mathrm{L}} - \mathbf{k}_o^{\mathrm{L}}$.

So the overall rotation is defined by $M \cdot 3$ parameters[1].

As next step, a sample is illuminated along $\mathbf{k}_0$ and we want to scan through the $\mathbf{k}$ for detecting the waves scattered by the according lattice planes. The sample has its own coordinate system (sample system). It is rotatetable for Θ_0 on an axis along the y-axis $(2')$ $\underset{0}{\mathbf{A}} = (0, 1, 0)$. Relative to the laboratory system it is chosen in a way that for $\Theta_0 = 0$ the axes of the sample system and the laboratory system have the

---

[1]One also has to consider the rotation directions. This can be done by defining the rotation axes by choosing the values ± 1 suitable.
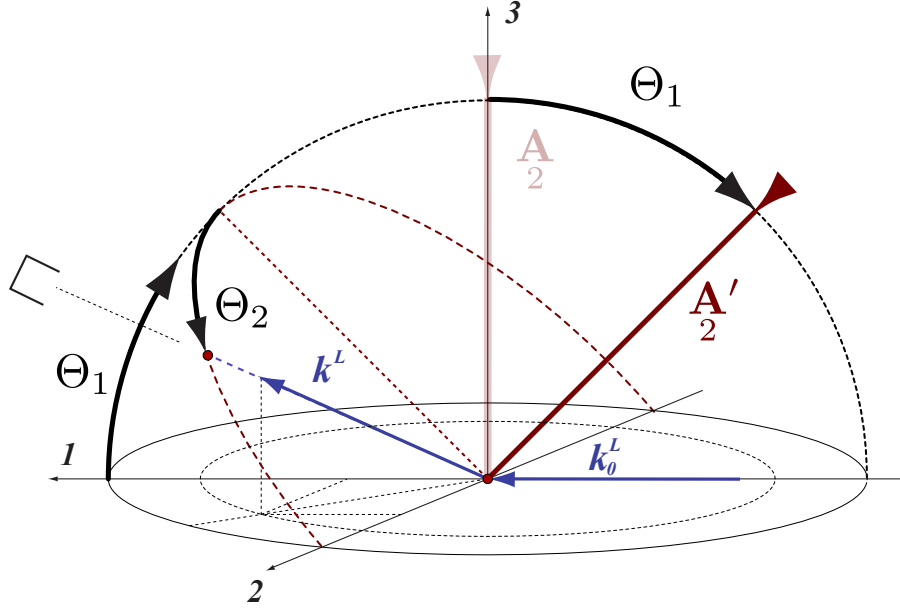
Figure 1.8: (a) Rotation of the detector in the laboratory system for the case $\mathbf{m} = \{1, 2\}$, $\underset{1}{\mathbf{A}} = (0, 1, 0)$, $\underset{2}{\mathbf{A}} = (0, 0, -1)$.

same directions and both have the same origin. Through rotating by Θ_0, we vary the incident angle of the beam and the sample system gets tilted with respect to the laboratory system (Figure 1.9(b)). For transforming $\mathbf{k}^L$ and $\mathbf{k}_0^L$ into the sample system it is obvious that we have to rotate them for Θ_0 somehow. To tansform from a cartesian system into a cartesian system, the transformation is the inverse of the rotation [26]. The inverse of a rotation matrix is simply the transposed rotation matrix. Therefore the transformation can be described as

$$\mathbf{k}^S = D_0^{-1}\left(\Theta_0, \underset{0}{\mathbf{A}}\right) \cdot \mathbf{k}^L$$

$$\mathbf{k}_0^S = D_0^{-1}\left(\Theta_0, \underset{0}{\mathbf{A}}\right) \cdot \mathbf{k}_0^L$$

and the observed scattering vector is

$$\begin{aligned}
\mathbf{q}^S &= \mathbf{k}^S - \mathbf{k}_o^S \\
&= D_0^{-1}\left(\Theta, \underset{0}{\mathbf{A}}\right) \cdot \left(\mathbf{k}^L - \mathbf{k}_o^L\right) \\
&= D_0^{-1}\left(\Theta_0, \underset{0}{\mathbf{A}}\right) \cdot \mathbf{q}^L
\end{aligned}$$

Note that $\mid \mathbf{q}^L \mid = \mid \mathbf{q}^S \mid$.

In the case that the sample is rotatetable around more axes, equation 1.29 can be used to formulate a transformation matrix for transforming a vector $\mathbf{r}^L$ from the laboratory system into to the sample system $\mathbf{r}^S$.
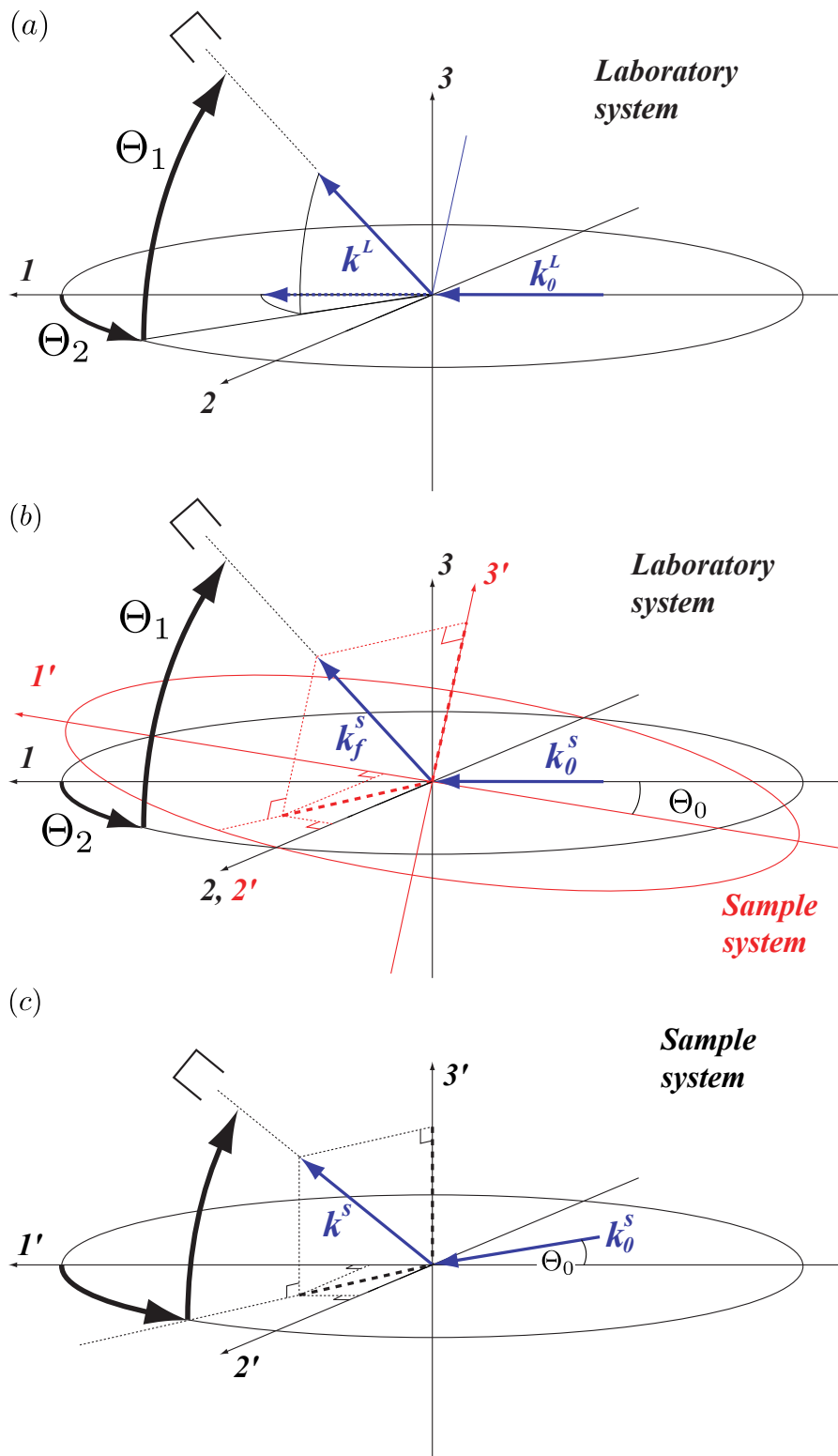
Figure 1.9: (a) Rotation of the detector in the laboratory system for the case $\mathbf{m} = \{2, 1\}$, $\mathbf{A}_1 = (0, 1, 0), \mathbf{A}_2 = (0, 0, -1)$. (b) Transformation from the laboratory system to the sample system. (c) Wavevectors in the sample system after rotation.

$$\mathbf{r}^{\mathrm{S}} \;=\; \Lambda^{-1}\left(\boldsymbol{\Theta}, \mathbf{A}, \mathbf{m}\right) \cdot \mathbf{r}^{\mathrm{L}} \tag{1.30}$$

All together now:

$$\mathbf{q}^{\mathrm{S}} \;=\; \Lambda^{-1}\left(\boldsymbol{\Theta}_0\right) \Lambda\left(\Theta_1, \Theta_2\right) \mathbf{d}^0$$

1.4.1 $\Theta/2\Theta$ Scan

Let's assume for example the case that $\Theta_1 = 2\Theta_0 = 2\Theta$. We get

$$D_1\left(2\Theta, \mathbf{A}_1\right) \;=\; \begin{pmatrix} \cos 2\Theta & 0 & -\sin 2\Theta \\ 0 & 1 & 0 \\ \sin 2\Theta & 0 & \cos 2\Theta \end{pmatrix}$$

and therefore

$$\mathbf{q}^{\mathrm{L}} \;=\; \frac{2\pi}{\lambda}\begin{pmatrix} \cos 2\Theta - 1 \\ 0 \\ \sin 2\Theta \end{pmatrix} = \frac{2\pi}{\lambda}\begin{pmatrix} -2\sin^2\Theta \\ 0 \\ 2\sin\Theta\cos\Theta \end{pmatrix}$$

with the identities

$$\begin{aligned} \sin 2\Theta &= 2\sin\Theta\cos\Theta \\ \cos 2\Theta &= 1 - 2\sin^2\Theta \end{aligned}$$

The length of the scatttering vector is

$$\begin{aligned} |\,\mathbf{q}^{\mathrm{L}}\,| &= \frac{2\pi}{\lambda}\sqrt{4\sin^2\Theta\left(\sin^2\Theta + \cos^2\Theta\right)} \\ |\,\mathbf{q}^{\mathrm{L}}\,| &= \frac{4\pi}{\lambda}\sin\Theta \end{aligned}$$

Transforming into the sample system reveals

$$D_0^{-1}\left(\Theta, \underset{0}{\mathbf{A}}\right) = \begin{pmatrix} \cos\Theta & 0 & \sin\Theta \\ 0 & 1 & 0 \\ -\sin\Theta & 0 & \cos\Theta \end{pmatrix}$$

$$\mathbf{q}^{\mathrm{S}} = \frac{2\pi}{\lambda} \begin{pmatrix} -2\sin^2\Theta\cos\Theta + 2\sin^2\Theta\cos\Theta \\ 0 \\ \sin\Theta 2\sin^2\Theta + \cos^2\Theta 2\sin\Theta \end{pmatrix}$$

$$\mathbf{q}^{\mathrm{S}} = \frac{2\pi}{\lambda} \begin{pmatrix} 0 \\ 0 \\ 2\sin\Theta(\sin^2\Theta + \cos^2\Theta) \end{pmatrix}$$

$$\mathbf{q}^{\mathrm{S}} = \frac{2\pi}{\lambda} \begin{pmatrix} 0 \\ 0 \\ 2\sin\Theta \end{pmatrix}$$

So we just get components perpendicular to the substrate and the norm of $\mathbf{q}^{\mathrm{S}}$ is

$$|\mathbf{q}^{\mathrm{S}}| = q_z = \frac{4\pi}{\lambda}\sin\Theta$$

At angles where the laue condition is fullfilled, we can expect enhanced intensities[2]
:

$$\begin{aligned} |\mathbf{q}^{\mathrm{S}}| &= \frac{2\pi}{d} \\ \lambda &= 2d\sin\Theta \end{aligned} \tag{1.31}$$

That's Bragg's law . $\mathbf{k}^{\mathrm{S}}$ and $\mathbf{k}_0^{\mathrm{S}}$ are

$$\mathbf{k}_0^{\mathrm{S}} = \frac{2\pi}{\lambda} \begin{pmatrix} \cos\Theta \\ 0 \\ -\sin\Theta \end{pmatrix}$$

$$\mathbf{k}^{\mathrm{S}} = \frac{2\pi}{\lambda} \begin{pmatrix} \cos\Theta \\ 0 \\ \sin\Theta \end{pmatrix}$$

So when performing a measurement in that way we scan for $|\mathbf{q}| = q_z$ perpendicular

---

[2]Note that the quantitative amount of photons reaching the detector dependens on factors like the structure factors.
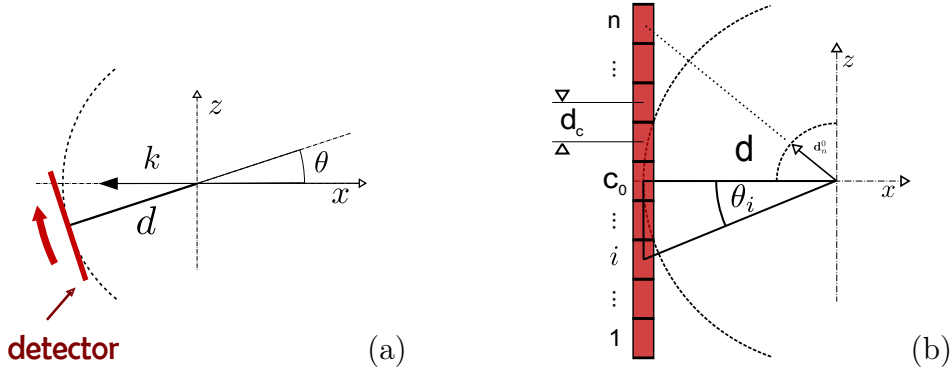
Figure 1.10: (a) Rotation of the detector through the beam to determine the center channel c_0 and the channel per degree cpd. (b) Angular relationship for the calculations.

to the x-y plane of the sample system. So for (hkl) parallel to the xy-plane. The incident angle equals the angle of the scattered wave relative to the latice plane. This type of scan is named *Specular Scan* or $\Theta/2\Theta$. This scan type is very useful and is described more in detail below.

1.4.2   1D Detector

1.4.2.1   The 1D Detector

A 1D detector consists of $i = 1, 2, \ldots, N$ pixels with a spacing d_c and pixel width d_w and is mounted on an arm at a distance d from the origin. We assume the pixels on a plane with the y-axis as the normal vector $(\mathbf{n}_d^0 = (0, 1, 0)$ and the point for defining the position in space is the center of rotation. The pixel hitted by the beam when $\Theta_1 = \Theta_2 = 0$ is denoted as c_0, i.e. the pixel that is on the x-axis. So the absolute pixel position p_i of the i'th pixel in the laboratory system is given by (schematic see figure 1.10(b)).

$$
\begin{aligned}
p_i &= (x_i, y_i, z_i) \\
z_i &= (i - c_0)\, d_c \\
x_i &= d \\
y_i &= 0
\end{aligned}
$$

1.4.2.2   Calibration

The parameters c_0 and d are not known a priori so they have to be evaluated. To determine c_0 and d the detector is rotated through the beam by varying Θ_1 . This

is illustrated in figure 1.10(b). So the beam hits a certain pixel at the angel $\theta_i = \Theta_1$ when

$$\tan \theta_i = \frac{z_i}{x_i}$$

$$\tan \theta_i = \frac{(i - c_0) \, d_c}{d}$$

and therefore the relation for the i-th pixel at the angle θ_i is

$$i \, (\theta_i) = c_0 + \frac{d}{d_c} \tan \theta_i$$

$\frac{d}{d_c}$ is called channel per degree (cpd) and is the slope of the function

$$i \, (\theta_i) = c_0 + cpd \tan \theta_i \tag{1.32}$$

The parameters c_0 and cpd are obtained from a fit of the experimental data with the model function 1.32, so the exact distance does not have to be known but can be calculated via $d = cpd \cdot d_c$.

Note that in most cases θ is varied in a region where $\tan (x)$ can be assumed as linear, and θ instead of $\tan (\theta)$ as independent variable is taken in the model function 1.32 to obtain the parameters c_0 and channel per degree $cpd°$ respectively. This has to be considered when comparing or communicating these parameters. The formalism is then different from the shown one. Instead of channel per degree it should be named channel per radian cpr in this context. θ as independent variable is suitable as long as the distance d between detector and origin is large enough. A conversion from cpd to $cpd°$ is performed via

$$cpd° = cpd \, \frac{\pi}{180}$$

So every pixel is looking at the origin under an angle

$$\theta_i = \arctan \left(\frac{i - c_0}{cpd} \right)$$

The theoretical angular resolution $\triangle\Theta_1 \, (i) = \theta_{i+1} - \theta_i$ of the detector[3] therefore is

---

[3]For the effective resolution the beam geometry has to be considered.

not linear in general.

$$\frac{d}{dx} \arctan(x) \quad = \quad \frac{1}{1+x^2} = \cos^2(\arctan(x))$$

The angular resolution $\delta\Theta_1$ deriving from the height of the pixel and linear behavior can be calculated as:

$$\delta\Theta_1 \quad = \quad \frac{1}{cpd} \tag{1.33}$$

The angular resolution $\delta\Theta_2$ deriving from the width d_w of the pixel:

$$\delta\Theta_2 \quad = \quad \frac{d_w}{cpd\, d_c} \tag{1.34}$$

The cartesian directions $\mathbf{d}_i^0$ represented by the now known θ_i (or the parameters c_0 and cpd) end on a circle with radius 1. This is shown schematically in figure 1.10(b).

$$\mathbf{d}_i^0 \quad = \quad (\cos\theta_i, 0, \sin\theta_i) \tag{1.35}$$

$$\mathbf{d}_i^0 \quad = \quad (\cos\left[\arctan\left(\frac{i-c_0}{cpd}\right)\right], 0, \sin\left[\arctan\left(\frac{i-c_0}{cpd}\right)\right]) \tag{1.36}$$

$$\mathbf{d}_i^0 \quad = \quad (\cos\left[\frac{i-c_0}{cpd°}\right], 0, \sin\left[\frac{i-c_0}{cpd°}\right]) \tag{1.37}$$

Another usefull way to generate the $\mathbf{d}_i^0$ is by rotating the starting point (1,0,0) for the θ_i on the rotation axis $\mathbf{n}_d^0$.

$$\mathbf{d}_i^0 \quad = \quad D_d\left(\theta_i, \mathbf{n}_d^0\right) \cdot \begin{pmatrix} 1 \\ 0 \\ 0 \end{pmatrix} \tag{1.38}$$

The wave vectors $\mathbf{k}_0^L(i)$ at the initial position subsequently can be written as:

$$\mathbf{k}_0^L(i) \quad = \quad \frac{2\pi}{\lambda}\, \mathbf{d}_i^0$$

Note   To simplify $\cos[\arctan(x)]$ we have to express $\cos(x)$ in $\tan(x)$.

$$\begin{aligned}
\cos^2(x) + \sin^2(x) &= 1 \\
\frac{\sin^2(x)}{\cos^2(x)} + 1 &= \frac{1}{\cos^2(x)} \\
\tan^2(x) + 1 &= \frac{1}{\cos^2(x)}
\end{aligned}$$
(1.39)

So the cosine gets

$$\begin{aligned}
\cos(x) &= \frac{1}{\sqrt{\tan^2(x) + 1}} \\
\cos(\arctan(x)) &= \frac{1}{\sqrt{x^2 + 1}}
\end{aligned}$$

and the sinus respectively

$$\sin(\arctan(x)) = \frac{1}{\sqrt{\frac{1}{x^2} + 1}}$$

Equation 1.36 now is

$$d_i^0 = \left(\frac{1}{\sqrt{\left(\frac{i-c_0}{cpd}\right)^2 + 1}}, 0, \frac{1}{\sqrt{\left(\frac{cpd}{i-c_0}\right)^2 + 1}} \right)$$

1.4.2.3 Rotation of the 1D detector

The direct aproach to calculate the end positions is to applie the rotations defined in section 1.4.

$$\mathbf{d}_i = \Lambda(\boldsymbol{\Theta}) \cdot \mathbf{d}_i^0$$

For example when rotating just for Θ_1 the position of the $\mathbf{d}_i$ is given by.

$$
\begin{aligned}
\mathbf{d}_i &= \Lambda\left(\Theta_1, 0\right) \cdot \mathbf{d}_i^0 \\
&= \begin{pmatrix} \cos\Theta_1 & 0 & -\sin\Theta_1 \\ 0 & 1 & 0 \\ \sin\Theta_1 & 0 & \cos\Theta_1 \end{pmatrix} \begin{pmatrix} \cos\theta_i \\ 0 \\ \sin\theta_i \end{pmatrix} \\
&= \begin{pmatrix} \cos\Theta_1\cos\theta_i - \sin\Theta_1\sin\theta_i \\ 0, \\ \sin\Theta_1\cos\theta_i + \cos\Theta_1\sin\theta_i \end{pmatrix} \\
&= \begin{pmatrix} \cos\left(\Theta_1 + \theta_i\right) \\ 0, \\ \sin\left(\Theta_1 + \theta_i\right) \end{pmatrix}
\end{aligned}
$$

There is a more elegant way when rembering that at the initial position $\Theta_1 = \Theta_2 = 0$ the directions $\mathbf{d}_i^0$ are unit vectors ending on a circle around the center of rotation. They all are on a plane defined by the normal vector $\mathbf{n}_d$.$\mathbf{n}_d^0$ is (0,1,0) at $\Theta_1 = \Theta_2 = 0$.

So the endpositions of the $\mathbf{d}_i$ is a rotation of a point $(1,0,0)$ and then for θ_i on the circle around $\mathbf{n}_d$ afterwards.

$$
\begin{aligned}
\mathbf{d}_i &= D_d\left(\theta_i, \mathbf{n}_d^0\right) \cdot D_1\left(\Theta_1\right) \cdot \begin{pmatrix} 1 \\ 0 \\ 0 \end{pmatrix} \\
&= \begin{pmatrix} \cos\theta_i & 0 & -\sin\theta_i \\ 0 & 1 & 0 \\ \sin\theta_i & 0 & \cos\theta_i \end{pmatrix} \begin{pmatrix} \cos\Theta_1 & 0 & -\sin\Theta_1 \\ 0 & 1 & 0 \\ \sin\Theta_1 & 0 & \cos\Theta_1 \end{pmatrix} \begin{pmatrix} 1 \\ 0 \\ 0 \end{pmatrix} \\
&= \begin{pmatrix} \cos\theta_i\cos\Theta_1 - \sin\theta_i\sin\Theta_1 & 0 & -\sin\theta_i\cos\Theta_1 - \cos\theta_i\sin\Theta_1 \\ 0 & 1 & 0 \\ \sin\theta_i\cos\Theta_1 + \cos\theta_i\sin\Theta_1 & 0 & -\sin\theta_i\sin\Theta_1 + \cos\theta_i\cos\Theta_1 \end{pmatrix} \\
&= \begin{pmatrix} \cos\left(\Theta_1+\theta_i\right) & 0 & -\sin\left(\Theta_1+\theta_i\right) \\ 0 & 1 & 0 \\ \sin\left(\Theta_1+\theta_i\right) & 0 & \cos\left(\Theta_1+\theta_i\right) \end{pmatrix} \begin{pmatrix} 1 \\ 0 \\ 0 \end{pmatrix} \\
&= \begin{pmatrix} \cos\left(\Theta_1+\theta_i\right) \\ 0, \\ \sin\left(\Theta_1+\theta_i\right) \end{pmatrix}
\end{aligned}
$$
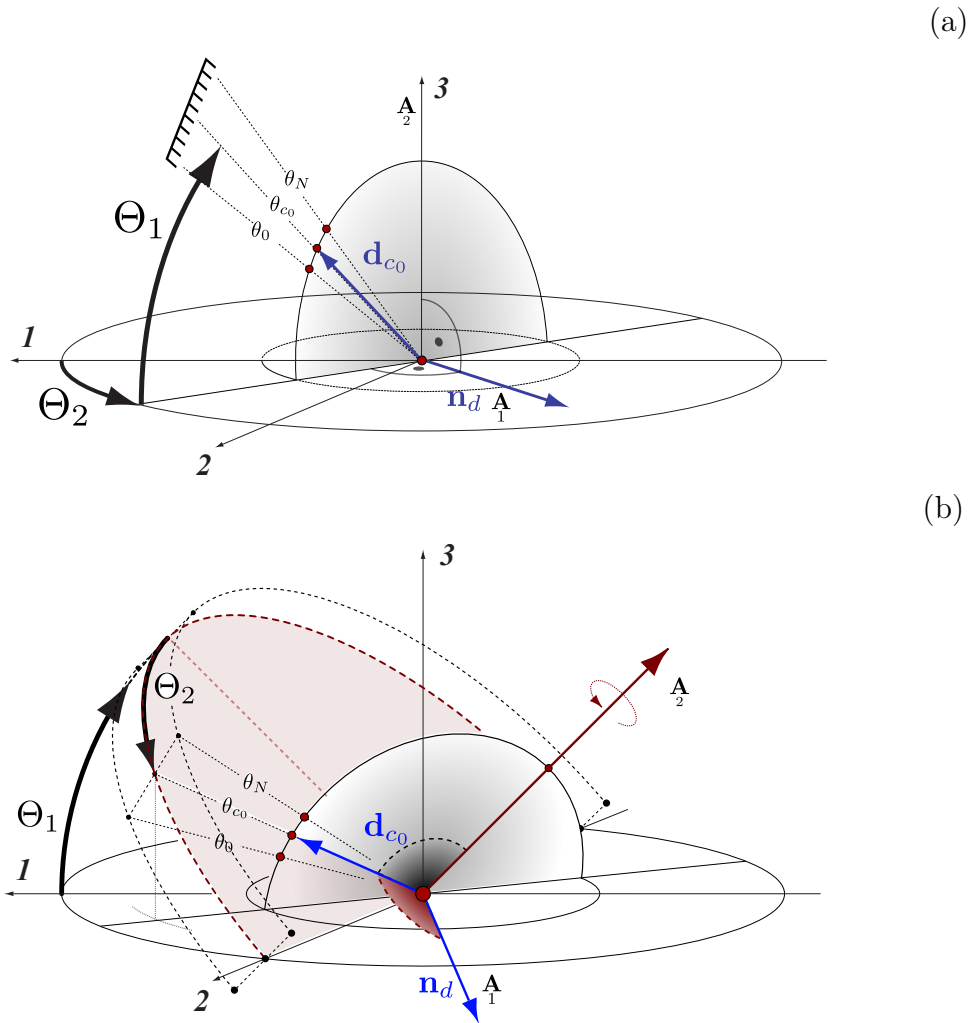
Figure 1.11: (a) Rotation of the detector for $\mathbf{m} = \{2, 1\}$, $\underset{1}{\mathbf{A}} = (0, 1, 0)$, $\underset{2}{\mathbf{A}} = (0, 0, -1)$. $\mathbf{d}_{c_0}$ behaves like a point detector and $\mathbf{n}_d$ stays in the x-y plane. The d_i stay on a circle in a plane defined by the orientation of $\mathbf{n}_d$ which gets tilted according to the axes configuration $\mathbf{m}$. (b) Rotation of the detector for $\mathbf{m} = \{1, 2\}$, $\underset{1}{\mathbf{A}} = (0, 1, 0)$, $\underset{2}{\mathbf{A}} = (0, 0, -1)$.

During a general rotation for Θ_1 and Θ_2 $\mathbf{n}_d$ gets tilted according to equation 1.29.

$$\mathbf{n}_d = \Lambda(\Theta_1, \Theta_2) \cdot \mathbf{n}_d^0$$

$$\mathbf{d}_i = D_d\left(\theta_i, \mathbf{n}_d^0\right) \cdot \Lambda(\Theta_1, \Theta_2) \cdot \begin{pmatrix} 1 \\ 0 \\ 0 \end{pmatrix} \tag{1.40}$$

Explicitely for $\mathbf{n}_d^0 = (0, 1, 0)$ and $\mathbf{m} = \{2, 1\}$ equation 1.40 can be written as

$$\mathbf{d}_i = \Lambda(\Theta_1 + \theta_i, \Theta_2) \cdot \begin{pmatrix} 1 \\ 0 \\ 0 \end{pmatrix}$$

$$
\begin{aligned}
\mathbf{d}_i &= \Lambda((\Theta_1 + \theta_i, \Theta_2), \{1, 2\}) \cdot \begin{pmatrix} 1 \\ 0 \\ 0 \end{pmatrix} \\
&= \begin{pmatrix} \cos(\Theta_1 + \theta_i) & 0 & -\sin(\Theta_1 + \theta_i) \\ 0 & 1 & 0 \\ \sin(\Theta_1 + \theta_i) & 0 & \cos(\Theta_1 + \theta_i) \end{pmatrix} \begin{pmatrix} \cos\Theta_2 & -\sin\Theta_2 & 0 \\ \sin\Theta_2 & \cos\Theta_2 & 0 \\ 0 & 0 & 1 \end{pmatrix} \begin{pmatrix} 1 \\ 0 \\ 0 \end{pmatrix} \\
&= \begin{pmatrix} \cos(\Theta_1 + \theta_i) & 0 & -\sin(\Theta_1 + \theta_i) \\ 0 & 1 & 0 \\ \sin(\Theta_1 + \theta_i) & 0 & \cos(\Theta_1 + \theta_i) \end{pmatrix} \begin{pmatrix} \cos\Theta_2 \\ \sin\Theta_2 \\ 0 \end{pmatrix} \\
&= \begin{pmatrix} \cos(\Theta_1 + \theta_i)\cos\Theta_2 \\ \sin\Theta_2 \\ \sin(\Theta_1 + \theta_i)\cos\Theta_2 \end{pmatrix}
\end{aligned}
$$

Chapter 2

Experimental Techniques

In this chapter the experimental methods applied in this work are introduced. First and foremost, x-ray diffraction techniques using monochromatic x-rays in various experimental geometries are presented, which were the main experimental tools applied throughout this work. These diffraction experiments are supported by optical and atomic force microscopy investigations, which were carried out to determine the morphology of the investigated samples.

In the present section the notation of several angles is changed from the form used in the derivations in Chap.1 to the more common form as found in literature, since, in the following, no more indexing of the angles is necessary. Therefore, the angle Θ_0 is labeled Θ and Θ_2 is labeled 2Θ.

2.1   X-Ray Specular Scan

In this type of experiment the angles 2Θ and Θ move coupled and therefore the incident angle α_i and the exit angle α_f are kept identical relative to a reference plane (i.e., the scattering plane). In practical experiments, where the x-ray source (e.g., a sealed tube, a beamline at a synchrotron light source) is generally fixed in space the detector is moved at twice the the speed (2Θ) of the sample Θ. By performing specular x-ray diffraction measurements information on lattice planes (hkl) perpendicular to the scattering plane is obtained.

Specular x-ray diffraction measurements, which are also frequently denoted as $\Theta/2\Theta$ scans in literature, are, for instance, the standard method of choice for powder samples. Strictly speaking, powder diffraction experiments are measurements in which the rotation of the sample around the angle Θ is obviously not necessary, because the grains of powder samples are statistically distributed in the x-ray beam.

Therefore, for a certain set of lattices planes (hkl) (corresponding to a certain 2Θ value, that is, detector position), the Laue equations are fulfilled independently of Θ. Figure 2.1 illustrates the diffraction conditions for a powder sample for a certain set of lattice planes.
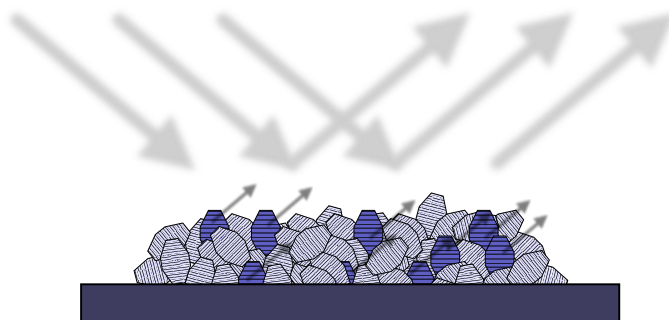
Figure 2.1: Schematic of a crystallite powder. The grains are statistically distributed in three dimensions and therefore the Laue conditions are fulfilled independently of the angle Θ during the scan.

However, this is no longer true for crystals grown on the surface of a substrate, as it is the case for crystalline organic films investigated in this work, where the detector is moved by 2Θ while the sample here is indeed rotated by the angle Θ being the half of 2Θ. Most importantly, epitaxial or textured films grown by vapor deposition or from solution can be investigated, which means that a preferential orientation of the crystallites in relation to the substrate plane can be determined. If the majority of crystallites in films grown on a substrate is preferentially oriented with respect to the substrate normal while they are azimuthally statistically oriented (i.e., in the form of a two-dimensional powder) this specific growth mode is denoted as *fiber texture*. This phenomenon is reported in an large number of studies on thin organic film growth, mostly on amorphous substrates (see, e.g., Ref. [4]). In Figure 2.1 a sketch of grains grown in a fiber-texture are shown.

Figure 2.2: Schematic of a fiber-textured film (2D-powder).

Figure 2.3: Schematic of a specular measurement. $2\Theta_0$ and Θ move coupled and therefore the incident angle α_i and exit angle α_f are equal during this (symmetric) scan. Therefore lattice planes (hkl) perpendicular to the xy-plane of the sample system are scanned. In the case of an ideal powder (see Figure 2.1) in the range of the scan all (hkl) contribute to the measured pattern. In the case of, e.g., a (00l) fiber textured film a series of (00l) peaks is observed in the pattern.

In general, the surface is aligned with the xy-plane of the sample system. As demonstrated in the previous chapter the components of the scattering vector during a specular scan are

$$
\begin{aligned}
q_x &= 0 \\
q_y &= 0 \\
q_z &= \frac{2\pi}{d} = \frac{4\pi}{\lambda}\sin\Theta_0 \\
\lambda &= 2d\sin\frac{2\Theta}{2}
\end{aligned}
$$

(2.1)

(2.2)

and enhanced scattering intensity is observed when the Laue conditions are fulfilled. A peak therefore identifies a certain lattice spacing with its associated reciprocal lattice vector $\mathbf{Q}_{hkl}$. In Figure 2.3 the scaling of the reciprocal vector during a specular scan is shown.

Bragg's equation 2.2 is a different representation of the diffraction condition (fully

equivalent to the Laue conditions), which is frequently used for determining the wavelength of a beam of unknown (or not exactly known) wavelength using a crystal of known crystal structure like, e.g., single crystalline silicon. This may become necessary if monochromatization at synchrotron light sources is not achievable with the desired accuracy.

The equations for the wave vectors during a specular scan are given by

$$
\mathbf{k}_0 = \frac{2\pi}{\lambda} \begin{pmatrix} \cos \alpha_i \\ 0 \\ -\sin \alpha_i \end{pmatrix}
$$

$$
\mathbf{k} = \frac{2\pi}{\lambda} \begin{pmatrix} \cos \alpha_f \\ 0 \\ \sin \alpha_f \end{pmatrix}
$$
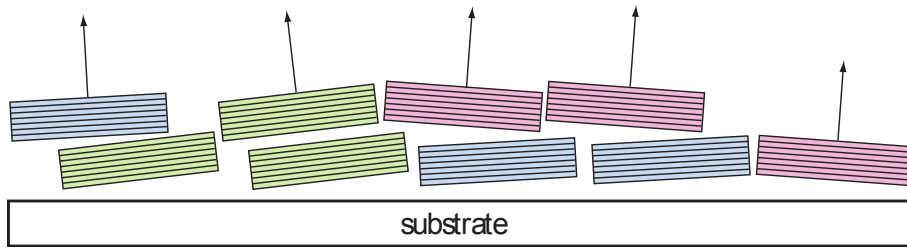
Figure 2.4: Crystallites in real thin films and their plane normals, which are not perfectly aligned. This deviation from ideality contributes to peak broadening of rocking curves of the respective Bragg peak. Image reproduced from [22]

2.2   X-Ray Rocking Curve

»The measurement of a rocking curve is performed such that the detector on the 2Θ circle is fixed to the center position $2\Theta_1^0$ of the Bragg peak under investigation, while the sample is tilted on the Θ circle ("rocked") in the vicinity of the Bragg angle Θ_1^0«[4]. In real thin films the lattice planes of, e.g., the fiber-texture, in laterally separated grains are in general distributed around their ideal positions (that is parallel to the substrate), as shown in Figure 2.4. In diffraction experiments on single crystals peak broadening due to imperfections of the crystal also occurs in rocking curves. To determine the extent of deviation from ideality the surface is, again, tilted for an angle ω relatively to the reference position, e.g., the surface. Then, ω is the deviation of the surface normal $\hat{\mathbf{n}}$ from the scattering vector. ω is in general the half of the scattering angle of the symmetric position $2\Theta_0$ relative to Θ. Thus, if $\Theta = \Theta_0$ this deviation is zero.

$$\omega \;\; = \;\; \Theta - \frac{2\Theta_0}{2} \qquad\qquad (2.3)$$

Note that for ω-angles exceeding $-\Theta_0$, and $+\Theta_0$ the incident beam or the detector would lie below the sample surface, respectively. In this case, no more scattering information from the sample can be obtained, and therefore the range of a rocking curve experiment is restricted to the range between $-\Theta_0$ and $+\Theta_0$. The width of the measured $I(\omega)$ peaks is proportional to the dislocation density within the film or the crystal. In the case of a single crystal, the rocking width is in general exceedingly low compared to that of a thin film sample.

The components of the scattering vector in terms of α_i and α_f are [18]:
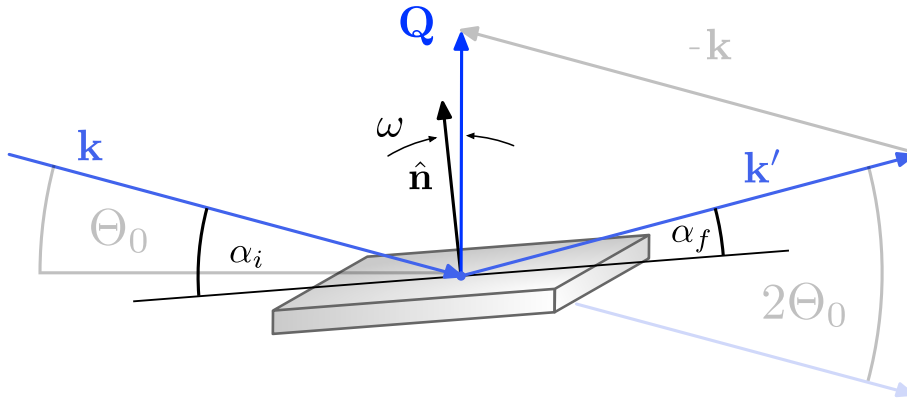
Figure 2.5: Schematic of a rocking curve measurement. The detector is set on a position $2\Theta_0$. Thus the scattering vector $\mathbf{Q}$ is constant (regarding both length and direction). The sample is "rocked" for Θ, and therefore the incident angle α_i and exit angle α_f are varied for ω relative to the surface. The resulting curve depends on the misalignment of the grains on the substrate. As a matter of principle, rocking curves of an ideal powder do not show enhanced intensity along Θ.

$$
\begin{aligned}
q_x &= \frac{2\pi}{\lambda} \left(\cos \alpha_f - \cos \alpha_i \right) \\
q_y &= 0 \\
q_z &= \frac{2\pi}{\lambda} \left(\sin \alpha_f + \sin \alpha_i \right)
\end{aligned}
$$

In terms of ω:

$$
\begin{aligned}
q_x &= |\mathbf{Q}| \sin \omega = \left(\frac{4\pi}{\lambda} \sin \frac{2\Theta_0}{2} \right) \sin \omega \\
q_y &= 0 \\
q_z &= |\mathbf{Q}| \cos \omega = \left(\frac{4\pi}{\lambda} \sin \frac{2\Theta_0}{2} \right) \cos \omega
\end{aligned}
$$
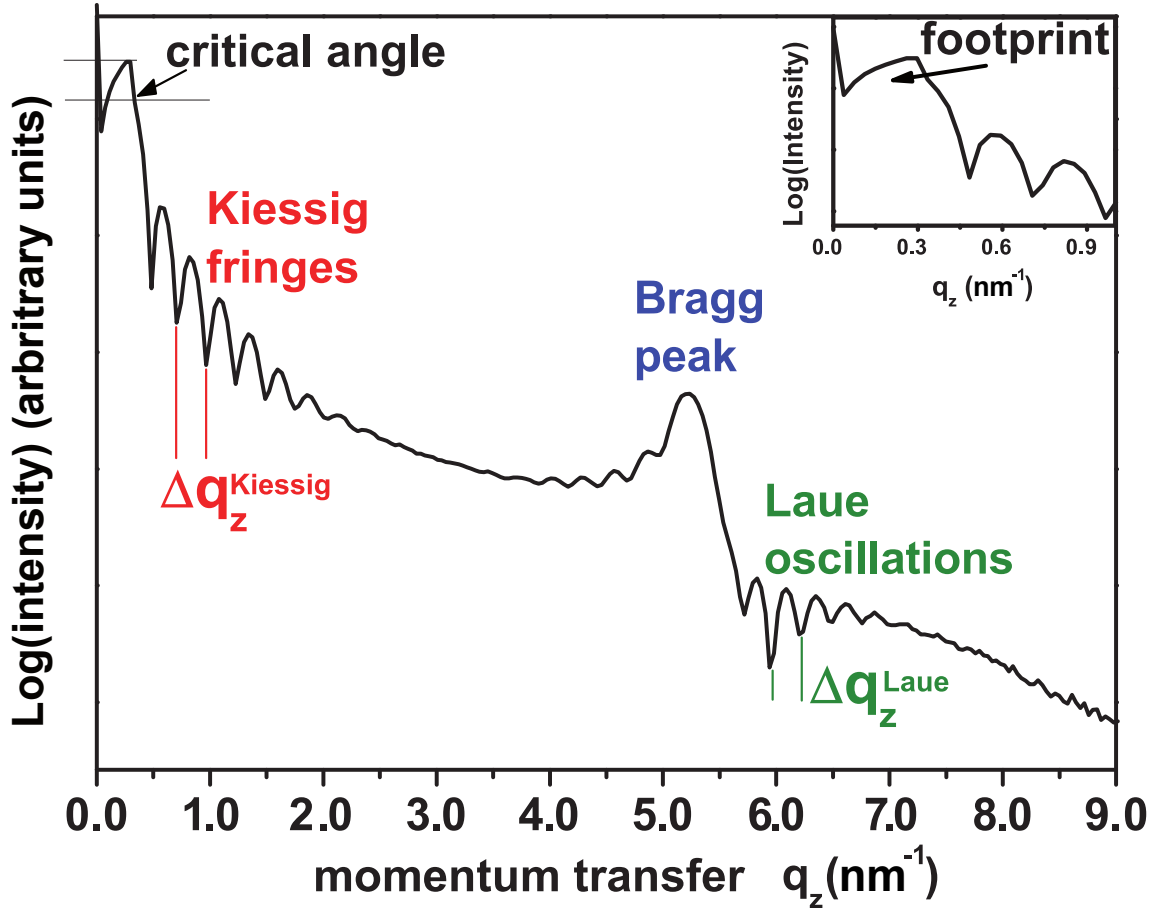
Figure 2.6: X-ray reflectivity scan on a thin film deposited on a certain substrate. The distance between two consecutive minima (or maxima) of the Kiessig fringes and Laue oscillations are illustrated. Inset: Low q_z-region demonstrating the footprint effect. (Image reproduced from [23])

2.3   X-Ray Reflectivity

X-Ray Reflectivity (XRR) is a suitable method for determining the average thickness D_L and roughness σ of surface layers and thin films. It makes use of reflection and refraction of radiation similar to optical ellipsometry. For more detailed explanations of the theoretical description of X-ray reflectivity and its application see for instance [4, 27, 18, 1].

Figure 2.6 shows a typical specular diffraction pattern of a thin film on a substrate in the regime of low momentum transfers q_z. The numerical values and ranges given in brackets are examples derived for the sample shown in Figure 2.6.

For values of q_z below a certain value (e.g., $q_z \sim 0.1\,nm^{-1}$) the pattern reveals high intensity with a fast decay upon increasing q_z that arises from contributions from the primary beam directly striking the detector, and, upon increasing q_z, being

shadowed by the rotating sample. Note that upon proper alignment of the sample $2\Theta = 0°$ and $\Theta = 0°$ and the sample shielding half of the x-ray beam. At a certain point ($q_z \sim 0.1\,nm^{-1}$) the intensity increases with increasing q_z. Here, the detector is moved out of the area of the primary beam and only contributions of primary-beam reflections from the sample surface are measured (still below the angle of total external reflection). At these low angles the projection of the beam (i.e., its footprint) exceeds the sample dimension, and this exceedance is reduced at increasing angles. This therefore leads to the observed deviation from a constant plateau behavior ($I(q_z) = const.$) in the region of the total external reflection. Upon further increase of q_z the footprint of the sample successively decreases, resulting in more x-rays being reflected at the sample surface and hitting the detector: An increase in intensity with increasing q_z is observed in this region. At a characteristic q_z ($\sim 0.3\,nm^{-1}$ in the Figure), that is the critical angle of the substrate, a sharp change in intensity is observed. Here, an additional small kink in the curves may be observed corresponding to the critical angle of the film material itself. For larger values of q_z the intensity finally follows the behavior $I(q) \sim q_z^{-4}$, which arises from Fresnel reflectivity [31]. In the following q_z range (~ 0.5 to $\sim 2\,nm^{-1}$ in Figure 2.6) pronounced oscillations are observed and arise from coherent interference effects (Kiessig fringes) of x-rays escaping from the thin film [18, 27]. For crystalline films at q_z values corresponding to the lattice spacing ($\sim 5\,nm^{-1}$) of the adsorbate steep increases of the intensity occur and Bragg peaks are observed. For highly crystalline films so-called Laue oscillations around the Bragg peaks can be found in addition, from which the crystal grain dimension perpendicular to the substrate surface can be estimated. For q_z values larger than the value for the Bragg peak $5\,nm^{-1}$ the intensity decreases down to background intensity. The approximate values of the layer thickness D_L can be deduced from the spacing of the Kiessig fringes [23]:

$$D_L \quad \sim \quad \frac{2\pi}{\triangle\, q_z^{Kiessig}}$$

where $\triangle\, q_z^{Kiessig}$ denotes the q_z-spacing of the fringes. A rough approximation for the crystal height is given by

$$h_{crystal} \quad \sim \quad \frac{2\pi}{\triangle\, q_z^{Laue}}$$

where $\triangle\, q_z^{Laue}$ denotes the q_z-spacing of the Laue oscillations [23].
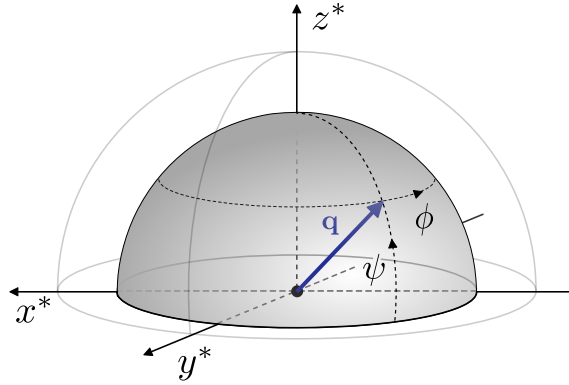
Figure 2.7: General geometry of the X-Ray Pole Figure Technique. Sequential variation of the tuple (ϕ, ψ) for ϕ between 0° and 360° and ψ between 0° and 90° allows mapping all accessible directions in a half sphere of radius $|\mathbf{q}|$ of reciprocal space.

2.4 X-Ray Pole figure

X-Ray Pole Figure Technique is the method of choice for determining the orientational distribution of crystallites *(i.e., its texture)*. A film comprising a large number of preferentially oriented crystallites is generally denoted as *well textured.*, in contrast, a powder sample comprising randomly distributed crystallites is denoted as *non textured.*

In general, in a diffraction experiment the scattering vector has to simultaneously equal a reciprocal lattice vector both in length and direction in order to observe enhanced diffraction intensity. Therefore, on using monochromatic x-ray radiation a certain set of net planes (hkl) of a single crystal in general does not lie parallel to the scattering vector $\mathbf{q}$ and the irradiation of the crystal with the x-ray beam does not lead to diffraction (Figure 2.7). Hence, the crystal has to be reoriented in a proper way in order to fulfill the scattering conditions. This can be done by rotating the sample around two perpendicular axes, frequently labeled as ϕ and ψ. Sequential variation of the tuple (ϕ, ψ) for ϕ between 0° and 360° and ψ between 0° and 90° results in a mapping of all accessible directions in the half sphere of radius $|\mathbf{q}|$ of reciprocal space (Figure 2.7).

With Θ and 2Θ set to positions, where the Bragg condition is fulfilled for a certain (hkl), peaks at tuples (ϕ, ψ) are observed according to the orientation of the single crystal or the crystallites in thin films. The representation of the tuples (ϕ, ψ) in stereographic projection is hence called *Pole Figure*. Figure 2.8 illustrates the experimental procedure described above..

The rotations of ϕ and ψ in a pole figure measurement are performed in the sample system. This therefore yields additional rotation matrices for the transformation
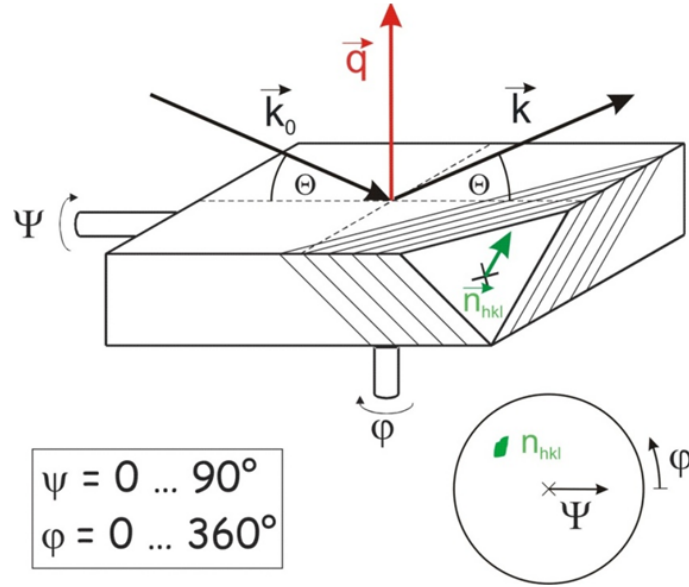
Figure 2.8: Θ, 2Θ and therefore the scattering vector are fixed in space during the measurement and define the inter-planar distance (corresponding to a certain (hkl)) under investigation. The single crystal is rotated along ϕ and ψ varying the position of $\hat{n}_{hkl}$. Diffraction occurs if the reciprocal lattice vector $\mathbf{Q}_{hkl}$ and the plane normal $\hat{n}_{hkl}$ are oriented parallel to each other. Image reproduced from [23]

from the laboratory system to the sample system. $\underset{\psi}{\mathbf{A}}$ is usually in the xy-plane and perpendicular to $\underset{\Theta}{\mathbf{A}}$; i.e., on the x-axis; $\underset{\phi}{\mathbf{A}}$ is perpendicular to both of them and, therefore, on the y-axis. Thus, the equation describing the scattering vector in terms of the scanning angles can be calculated from the given formula in the previous section:

$$\mathbf{q}^{\mathrm{S}} \;=\; \Lambda^{-1}\left(\mathbf{\Theta}, \psi, \phi\right) \Lambda\left(2\Theta\right) \mathbf{d}^{0}$$

2.5   X-Ray Grazing Incidence Diffraction (GID)

GID is the method of choice for investigating fiber-textured thin films (down to monolayer thickness) of unknown crystal structure due to its high surface sensibility [4, 18].

For textured films in specular geometry only few (and linearly dependent) reflexes are experimentally accessible, because in the case of fiber-textured films the grains are statistically distributed with respect to ϕ and well aligned with respect to the substrate. Therefore, a fiber-textured film represents a two-dimensional powder (Figure 2.9). To gain access to off-specular reflexes of a fiber-textured film, in principal x-ray pole figure technique can be applied. However, this experimental
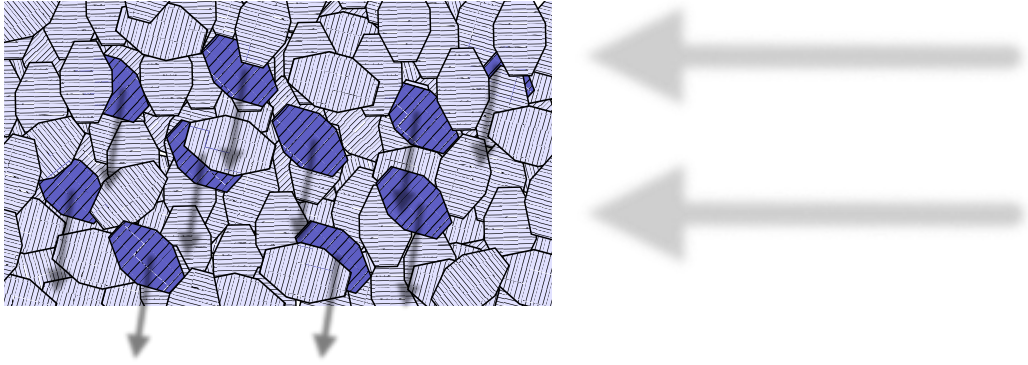
Figure 2.9: Schematic of diffraction of a 2D powder in GID geometry.

geometry has significant drawbacks concerning its surface sensitivity compared to GID, which, in principal, makes GID the method of choice for investigating fiber-textured thin films (down to monolayer thickness) of unknown crystal structure [4]. Here, the incidence angle ($\alpha_i = \Theta_0$) is set fixed at/below the critical angle α_c of total external reflection of the sample (note that α_c strongly depends on the substrate material used). Several sweeps of (Θ_1, Θ_2) then provide an intensity map that can be transformed into reciprocal space, yielding a *Reciprocal Space Map*. At certain tuples (Θ_1, Θ_2) within this map the Laue conditions are fulfilled and peaks corresponding to distinct (hkl) occur (Figure 2.10).

The components for the scattering vector $\mathbf{q}$ in the sample system can be calculated by

$$\mathbf{q}^{\mathrm{S}} = \Lambda^{-1}\left(\mathbf{\Theta}_0\right)\Lambda\left(\Theta_1, \Theta_2\right)\mathbf{d}^0$$

Due to the fact that the grains under investigation are statistically distributed with respect to the azimuthal angle ϕ in fiber-textured samples information on $\mathbf{q}$ is lost in an RSM experiment. The components of $\mathbf{q}$ reduce to two, i.e., $q_\parallel$ and q_z, as sketched in Figure 2.11. These two components are derived by:

$$
\begin{aligned}
q_\parallel &= \sqrt{q_x^2 + q_y^2} \\
q_x &= \mathbf{q}^{\mathrm{S}} \cdot \mathbf{e}_x \\
q_y &= \mathbf{q}^{\mathrm{S}} \cdot \mathbf{e}_y \\
q_z &= \mathbf{q}^{\mathrm{S}} \cdot \mathbf{e}_z
\end{aligned}
$$
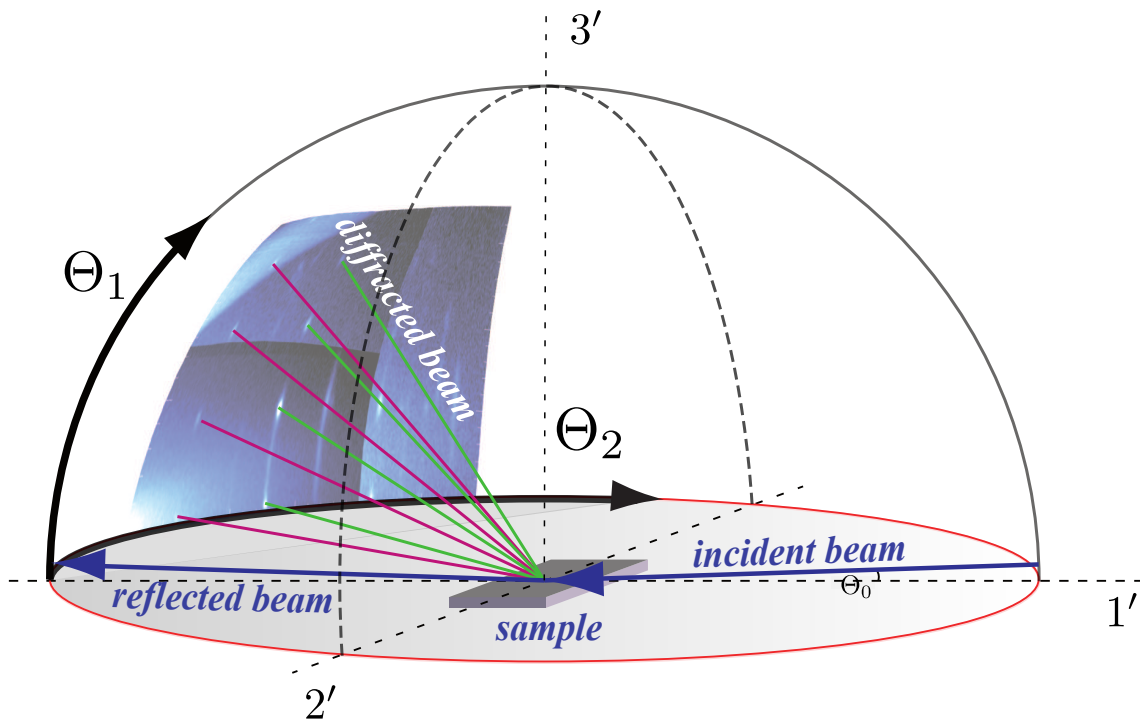
Figure 2.10: Schematic of a Grazing Incident Diffraction experiment. The majority of the incident x-ray intensity is totally reflected because of the grazing incident geometry with $\alpha_i < \alpha_c$. For a number of (hkl) in the fiber-textured film the diffraction conditions are fulfilled yielding at peaks in the reciprocal space map (picture taken from [23]).
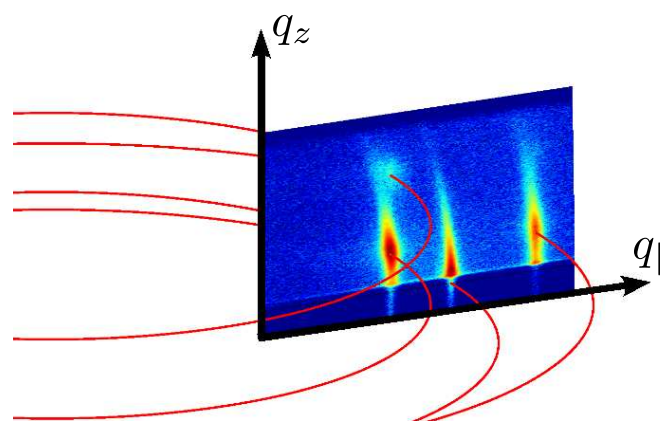
Figure 2.11: In fiber-textured films the reciprocal lattice degenerates into a set of rings around the fiber axis. This allows determining information on the whole lattice by a single planar cut ($q_\parallel$ and q_z) through the reciprocal space in terms of a reciprocal space map. (Image reproduced from [16])
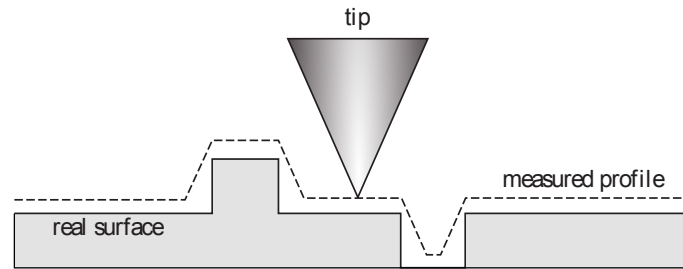
Figure 2.12: An atomically sharp tip scans over a surface. Measuring the forces in between allows to determine the three dimensional topology of the surface.The width of the tip primarily determines the measurement resolution of the device. This is sketched in the image above distinguishing between the real and the measured profile (dashed). (picture taken from [23])

where $\mathbf{e}_x$, $\mathbf{e}_y$, $\mathbf{e}_z$ are the base vectors of the z-axis in the sample system.

2.6 Atomic Force Microscopy (AFM)

Atomic force microscopy (AFM) is a very high-resolution method to map a surface in 3D with a hight resolution on the order of atmic scale. Forces between the atomic sharp tip and the substrate are measured and several mechanisms maintain that either the forces between surface and tip stay constant or the tip remains at a constant height over the surface. These forces are proportional to the local height of the sample. Therefore a three dimensional topographical maps of the surface can be produced[19, 3].

Chapter 3

Processing Techniques

Coating of surfaces is an important part of industrial and scientific processes. On one side to control / investigate the properties of the coating on the other side to obtain functional products in a wide field of applications. Techniques where solutions are involved often are applied in engineering and science, for reasons of easy processing, low costs, ... Especially in organic electronics and polymere science.

3.1 Solution Fabrication

In this manuscript fabrication of thin films from solution is the mainly applied preparation method in different varieties. As the solution parameters contribute to morphology and properties of the produced film some common definitions are introduced to assure reproducibility. The definitions are taken from "The Goldbook" the Compendium of Chemical Terminology[13, 6, 9].

A *solution* is a homogeneous mixture composed of two or more substances [9]. In this work it is dealt with a 2 component system; a solid material (*solute*) is dissolved in a liquid (*solvent*). The *concentration* characterizes the composition with respect to the amount of each component in the mixture. There are several ways to define the concentration, and therefore the used are listed below.

mass concentration (γ)**:** Mass of a constituent divided by the volume of the mixture.

mass-volume percentage $\left(\frac{wt}{V}\,\%\right)$**:** Mass concentration γ multiplied by 100

mass fraction (w)**:** Mass of a constituent divided by the total mass of all constituents in the mixture

mass percentage ($wt\,\%$)**:** Mass fraction w multiplied by 100

To determine the mass of the constituents a balance from "Acculab Lab" named "Balance ALC-110.4" was used. The stated values are correct to the endmost decimal place.

The solution preparation was performed always in the same manner. The weight of a glass bottle was measured without and with the solvent within. So the difference is the weight of the solvent. A separately weighted portion of the material was mixed with the solvent. The solution was stirred with a PTFE[1] coated magnetic stir bar for several hours. The concentration of the solution is given as mass-volume percentage in mg/ml. The volume of the solvent is calculated by multiplying the mass with the inverse of the density at room temperature $293K$.

A simple calculation example is given in table 3.1.

	THF	$unit$
ρ	0.889	g/cm^{-3}
m_S	0.828	g
V_S	0.93	ml
$solute$	0.001	g
$wt\,\%$	0.12	$\%$
$\frac{wt}{V}\,\%$	1.07	mg/ml

Table 3.1: Table with parameters to determine the concentration of a solution. Where ρ is the density , m_s the mass and V_s the volume of the solvent. The volume is calculated by the inverse of the density multiplied by the mass. ρ is taken at room temperature ($293K$). Mass percentage is abbreviated as $wt\,\%$. Mass-volume percentage as $\frac{wt}{V}\,\%$ stated in mg/ml.

---

[1]polytetrafluoroethylene (PTFE) is most well known by the DuPont brand name Teflon®

3.2 Dropcast

Dropcasting is a very simple but rough method to produce films or better film equivalent morphologies. The procedure simply consists of three steps: A drop of the solution is deposited on a substrate (1) where it disperses and the solvent evaporates (2) until no solvent is left and a dried film of the dissolved material remains (3). This is sketched in figure 3.1.
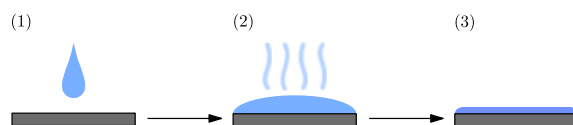
Figure 3.1: A drop of the solution is deposited on a substrate (1) where it disperses and the solvent evaporates (2) until no solvent is left and a dried film of the dissolved material remains (3).

The resulting film properties are only qualitative controllable.

- First the amount of remaining material on the substrate previously dissolved in the solvent determined by the concentration and amount of the solution applied.

- Second the evaporation time of the solvent determined by the vapor pressure of the solvent, ambient pressure and ambient temperature.

- Further geometrical factors as substrate size and tilt angel (e.g. horizontal alignment)

Both drying process as the processed film usually are macroscopic observeable with the eye or the microscope. This circumstance is very usefull to valuate the resulting film and get an overall feeling for the processes taking place. It's a good starting point for x-ray investigations according to texture and polymorphism.

The evaporation time of the solvent was controlled by covering the sample with glass spheres. To generate a protective atmosphere of solvent vapor and to reduce the amount of solvent escaping. Drying times in the range of 2 min to several hours could be realized.

3.3 Spincoating

Spin coating is a typical process to manufacture reproduceable and defined thin films in organic electronics and science [32, 31, 28, 10]. Filmthickness depends on several process variables; including spin speed, viscosity, drying rate, surface tension, . . .

In principle there are three main steps. A solution drop is deposited on a substrate (1) where it disperses due to the rotation of the substrate (2) until no solvent is left and a thin film of the dissolved material remains (3). A schematic of this process is shown in figure 3.2.
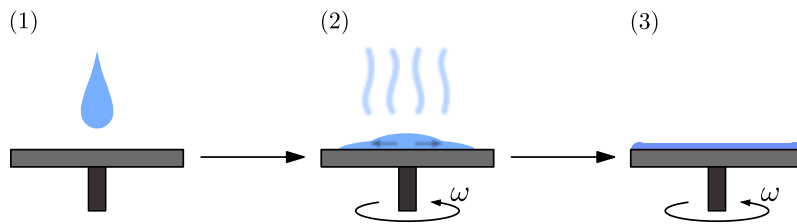
Figure 3.2: A solution drop is deposited on a substrate (1) where it disperses due to the rotation of the substrate (2) until no solvent is left and a thin film of the dissolved material remains (3).

Most common parameter used to control the film thickness h are spin speed ω and viscosity η. In a first approximation the relation for the filmthickness in terms of ω and η can be formulated as [10].

$$h = c_0 \, \eta^{c_1} \omega^{-c_3}$$

c_0 is proportional to the molecule extensions. The fast rotation generates centrifugal forces resulting in a radial flow. h and spin speed ω are related by a power law of the form $h \propto \omega^{-c_3}$ and therefore reducing the thickness. The flow is hindered by viscous forces which are determined by the solution and increases the film thickness i.e. $c_1 > 0$. The absolute values depend on the used system [32]. The spin speed determines the velocity of the process affecting the evaporation rate and drying time. The viscosity amongst others is a function of the concentration $\mu(c)$ [32, 11, 21]. For dilute solutions even a linear relationship is reported [32] .

The film thickness at a certain spin speed therefore is controllable by varying the concentration. With this two parameters a sequence of increasing layer thickness is produceable as applied for experiments described below. A close up of the principle processes is shown in Figure 3.3.
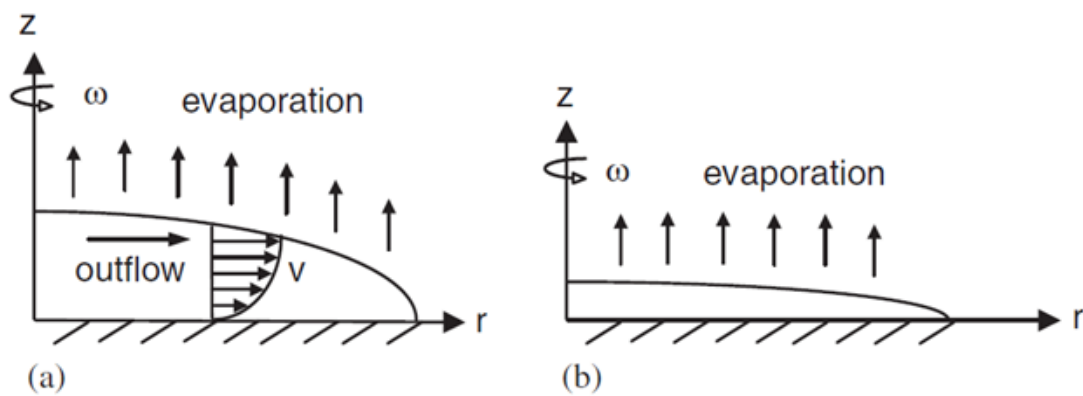
Figure 3.3: Close up of the spin coating process. During the rotation the fluid disperses due to centrifugal forces. The flow is hindered by viscous forces which are determined by the solvent (a). A thin lubric film remains and the remaining solvent evaporates aided by rotation (b). Image reproduced from [32].

Chapter 4

The Materials

4.1 Substrate

As base material for the substrates (100) cutted thermal oxidized silicon wafers were used. The wafers were cutted in to small pieces of about $1,5 \times 1,5\,cm$ and afterwards cleaned in an ultra sonic isopropanol bath for about 2 hours. After the bath they were blown clear with CO_2. This procedure was applied to all substrates to minimize contamination by unmeant particles on the surface.

Figure 4.1 shows the low q specular diffraction pattern of the cleaned substrate. For q_z values smaller than $0.1\,nm^{-1}$ the pattern reveals high intensity with a strong decay as the q_z is increasing and arises due to contributions from the direct beam striking the detector. At $q_z = 0.1\,nm^{-1}$ the intensity increases with increasing q_z. At this q_z values the detector is moved out of the area of the primary beam and only contributions from the sample surface are measured. The projection of the beam (footprint) at this shallow angles exceeds the sample dimension. This results in a deviation of the plateau behavior ($I(q_z) = const.$) in the region of the total external reflection. As q_z is increasing the footprint of the sample decreases resulting in more X-rays being able to be reflected at the sample surface and hit the detector; an increase of intensity with increasing q_z is noted. At $q_z \sim 0.29\,nm^{-1}$ a sharp change in the intensity is observed and belongs to the critical angle of the silicon substrate. For q_z values larger than the $0.29\,nm^{-1}$ the intensity follows the typical $I(q) = q_z^{-4}$ arising from the Fresnel reflectivity. In the q_z range from 0.5 to $2\,nm^{-1}$ fast oscillations are noted and arise from the coherent interference (Kiessig fringes) of x-rays escaping from the Si–SiO_x. For q_z - values larger than $2.42\,nm^{-1}$ the intensity decreases until the background at $3.5\,nm^{-1}$ is reached. The layer thickness of the used silicon substrates is $\sim 80\,nm$. Determined by a fit of the XRR pattern shown in the figure 4.1.
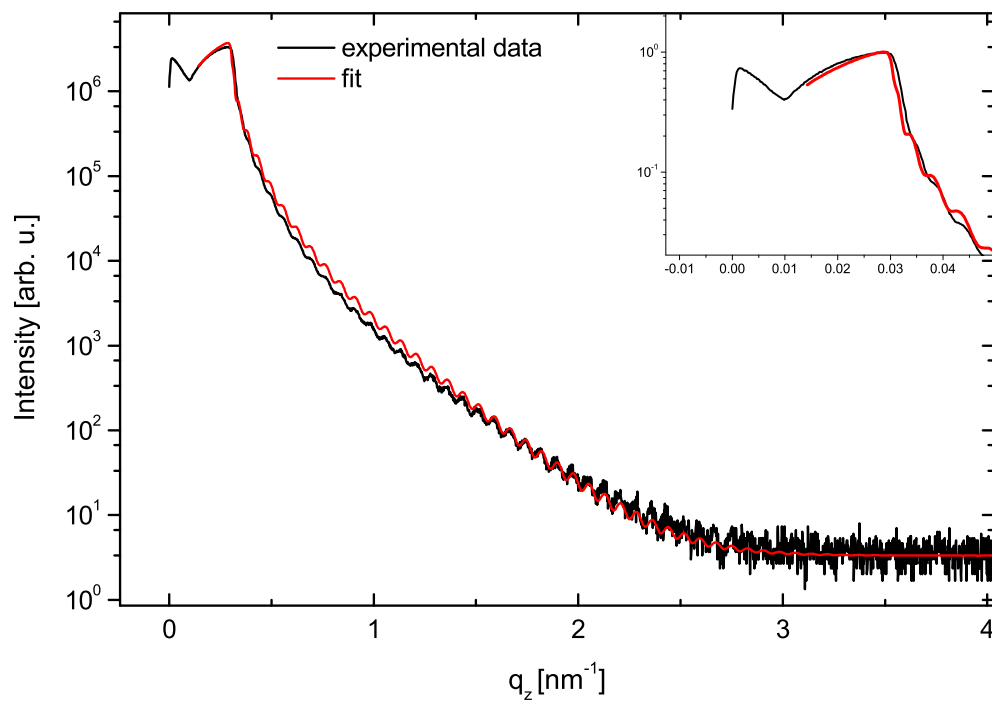
Figure 4.1: X-Ray reflectivitiy pattern on the cleaned substrate to determine SiO_x-layer thickness

The fit was performed with the program WinGixa in version 1.102.

4.2 DH3T

Dihexyl-terthiophene (DH3T) is a rodlike small molecule with the molecular formula $C_{24}H_{32}S_3$. It consits of a rigid aromatic core of 3 thiophene and 2 flexible hexyl side chains. The structural formula is shown in figure 4.2
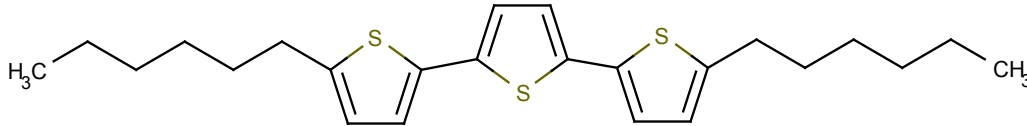
Figure 4.2: Structural formula

. The length of the flat molecule is approximately[1] $\sim 2.8\,nm$ and has a molecular weight of about $\sim 416.716\,(g/mol)$. As powder it is dark green and tends to create needle like structures. It consistens is kind of slippery similar to graphite. It has a dipolmoment of about 0.6 Debye1[2] with its direction normal to long axis and along the flat core. It is hydrophobic and lipophilic. A transition from the crystalline state to a liquid crystalline state is observed at 52°C and melting of the material was detected at 82°C [5].

Its unit cell parameters in the a-phase are $a_1 = 2.394\,nm$, $a_2 = 0.565\,nm$, $a_3 = 5.240\,nm$ with a non orthogonal angle between $\alpha_2 = \angle(a_1, a_3) = 97.817°$. So the unit cell Volume is $V_{UC} = 6.9925\,nm^3$. The packing of its single crystal (a-phase) is shown in figure 4.3.

---

[1]The length of a hexyl-chain is approximately: $(0.15 + n \cdot 0.127)\,nm$. A terthiophene has a length of approximately $1.03\,nm$[5].

[2]Private conversation: Georg Heimel (Humboldt Universität, Institut für Physik, SMS)
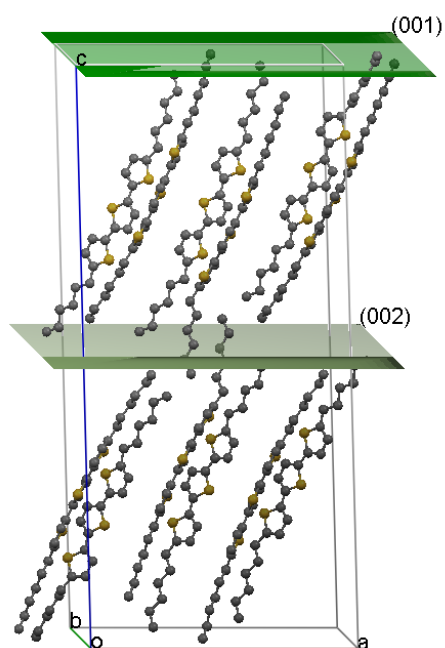
Figure 4.3: Molecular packing of DH3T in the single crystal (a-phase).

Chapter 5

Experimental Results

5.1 Dropcast

5.1.1 Fitting

A reflection profile $I(2\Theta)$ in general can be written as

$$I(2\Theta) = I_0 f(2\Theta - 2\Theta_0, 2\omega, \dots)$$

The fitting is performed with $2\Theta\,[°]$ as independent variable[4].

XRR Peaks of XRR pattern in this section are fitted with a Gaussian profile, because only the peak position and relative heights are taken into account. Data analysis were performed with the program MagicPlot © 2010 (MagicPlot.com). The used model function 5.1 uses the fitting parameters amplitude I_0, the peak position $2\Theta_0$ and the Half Width Half Maximum ω.

The Gaussian distribution function is usually written with the power of the Standard Deviation σ^2 as denominator in the exponential term.

$$I = I_B + \frac{A}{\sigma\sqrt{\frac{\pi}{2}}} e^{-\frac{(2\Theta - 2\Theta_0)^2}{2\sigma^2}}$$

The data is manually baseline corrected so the background I_B is not needed and $\frac{A}{\sigma\sqrt{\frac{\pi}{2}}}$ gets I_0 instead and can be seen as the amplitude. The remaining equation now is:

$$I = I_0 \exp\left[-\frac{(2\Theta - 2\Theta_0)^2}{2\sigma^2}\right]$$

ω is calculated by

$$\omega \;=\; \sqrt{2\ln 2}\,\sigma$$

and therefore the model function with ω as denominator is:

$$\sigma^2 \;=\; \frac{\omega^2}{2\ln 2}$$

$$I \;=\; I_0\,\exp\left[-\ln 2\,\frac{(2\Theta - 2\Theta_0)^2}{\omega^2}\right] \tag{5.1}$$

$$I\,(2\Theta) \;=\; I_0\,f_G\,(2\Theta - 2\Theta_0, \omega) \tag{5.2}$$

Following tables in this section contain Full Width Half Maximum 2ω because it is more common. 2ω is calculated by

$$2\omega \;=\; 2\cdot\omega \tag{5.3}$$

XRD & Rocking   Peaks of XRD an rocking curves shown in this section are fitted with a PSEUDO-VOIGT function. Data analysis was performed with the program TOPAS and fityk[1]. The PSEUDO-VOIGT function is a weighted superposition of CAUCHY f_C and GAUSS f_G functions.

$$f_{pV}\,(2\Theta) \;=\; \eta\,f_C\,(2\Theta) + (1-\eta)\,f_G\,(2\Theta)$$

The weight parameter η determines the amount of Cauchy share in the combined profile [4]. With

$$f_C\,(2\Theta) \;=\; \left[1 + \frac{(2\Theta - 2\Theta_0)^2}{\omega^2}\right]$$

$$f_G\,(2\Theta) \;=\; \exp\left[\frac{-\ln 2\,(2\Theta - 2\Theta_0)^2}{\omega^2}\right]$$

---

[1] http://www.unipress.waw.pl/fityk/

solvent	THF	
ρ	0.889	g/cm^{-3}
DH3T	0.001	g
m_S	0.828	g
V_S	0.93	ml
$wt\,\%$	0.12	$\%$
$\frac{wt}{V}\,\%$	1.07	mg/ml

Table 5.1: Parameters for calculating the concentration of the used solution. It was used for sample (0011),(0012) and (0013). ρ...density of solvent, m_S... mass of solvent, V_s... volume of solvent, $wt\,\%$... mass percentage, $\frac{wt}{V}\,\%$... mass-volume percentage. The used solvent was Tetrahydrofuran(THF).

5.1.2 Evaporation Rate

A series of drop casted films was prepared by variation of the evaporation rate of the solvent. While under ambient conditions the drop volume dried within two minutes, the evaporation time of the solvent could be delayed to 600 minutes by using a protective atmosphere of the solvent.

The sample preparation was performed the same way for all treated in this section except the evaporation time. 8 drops where deposited on the substrate in a way that all of the surface was covered. The elusion of the solvent was hindered by subsequentially more glass domes covering the sample. Principally four stages where used and are denoted as P I, P II, P III and P IV . When using Tetrahydrofuran[2] (THF) resulting in an evaporation time t_e of $\sim 2\,min$, $\sim 12\,min$, $\sim 30\,min$, $\sim 130\,min$ respectively. The roman numerals represent increasing coverage while increasing. To determine an approximate evaporation time the time was recorded from the deposition till the end of the evaporation process. The end point was defined as the moment where no liquid could be seen with the eye anymore and changes of the morphology could be observed. The resulting structures were analyzed by x-ray techniques and optical light microscopy.

5.1.2.1 Preparation I

The shown results in this subsection where obtained from the sample with the identification number (0011). It was produced from a solution with a concentration of $1.07\,mg/ml$. One dome was put half over the sample resulting in an evaporation time of two minutes $t_e \sim 2\,min$. The necessary parameters to evaluate the concentration are given in table 5.1.

---

[2]ROTIDRY® $\geq$99,9 % ($\leq$50 ppm H2O) , CAS-number [109-99-9]
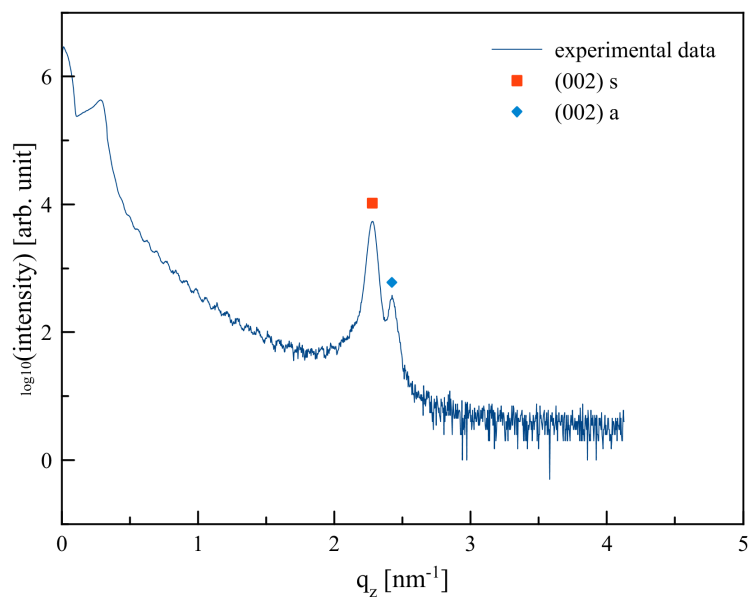
(a)
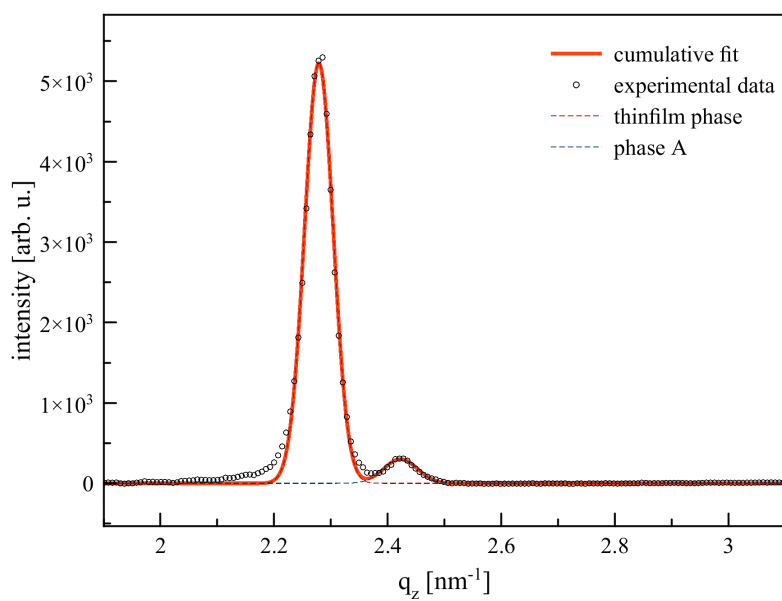
(b)

Figure 5.1: X-ray reflectivity scan on drop-casted film prepared by method P I. (a) logarithmic plot (b) linear plot with fitted curves

XRR   Figure 5.1(a). shows a XRR pattern of the dropcasted film with sample number (0011) and an evaporation time of $\sim 2\,min$. At $q_z = 0.24\,nm^{-1}$ a small kink in the curves is observable which corresponds to the critical angle of the D3HT film. In general, a more pronounced critical angle for homogeneous films are observed and allows for a highly accurate determination of the density of the material. However, as the critical angle for this film is not clearly defined in Fig.1.1 indicates a layer formation which is not homogeneous over the entire film which will be further discussed below. In the q_z range from 0.5 to $2\,nm^{-1}$ fast oscillations are noted, other oscillations in this q_z range are not observed indicating again a non uniform film formation of the drop casted D3HT film. At q_z values larger than $2\,nm^{-1}$ a steep increase of the intensity occurs and two Bragg peaks can be identified revealing the presents of highly crystalline D3HT with the peak position at $2.28\,nm^{-1}$ and $2.42\,nm^{-1}$. For the evaluation of the Bragg peaks Gaussian fits to the experimental data are applied (Fig. 5.1(b)). The data is corrected for the Fresnel reflectivity. A fit consisting of two simultaneous Gaussian distribution functions is required to fit the experimental data. The extracted peak position and the full width at half maximum values for each Bragg peak is summarized in Table 5.2. The first Bragg peak reveal a peak position at $2.28\,nm^{-1}$ corresponding to a real space lattice plane distance of $2.76\,nm$ which is close to the maximal theoretical extension of a DH3T molecule of $2.8\,nm$; see section 4.2. This suggests that the D3HT molecules arrange in a up right standing morphology with the long molecular axis nearly perpendicular to the sample surface and is classified as the surface mediated *thin-filmphase* (s-phase) as will be further discussed below. The Bragg peak with the maximum at $2.42\,nm^{-1}$ corresponds to a real space lattice plane distance of $2.6\,nm$ revealing the existence of a second crystalline phase with DH3T molecules nearly perpendicular to the sample surface. The thiophene units, the alkyl chains or the entire molecule has to be tilted slightly away from the surface normal on account of the reduced normal extension. The corresponding phase is classified as the $(002)^a$ reflex from the *alpha phase* (a-phase) and is known from the single crystal solution described in section 4.2. The evaluation of the peaks reveal similar peak width for the thin film phase and the alpha phase within the film; for details see table (5.2).

phase	$q_z^0\,(nm^{-1})$	$\pm(nm^{-1})$	$2\omega\,(n, m^{-1})$	$\pm(nm^{-1})$	$I_0\,(arb.\,u.)$	$\pm(arb.\,u.)$
s	2.28	0.01	0.06	0.01	5230	60
a	2.42	0.01	0.07	0.01	301	8

Table 5.2: fitting parameters from data shown in figure 5.1

The width 2ω corresponds to the crystallite extension [4], i.e. the number of net planes along the surface normal. This suggests that the crystallite size of the two

phases are comparable. The intensity of the Bragg peak corresponds to the amount of crystallites within the sample and reveal a 17 times more intense Bragg peak for the thin film phase compared to the alpha phase. This strongly suggests that the number of crystallites are strongly dominant within the film. However, an exact evaluation of the crystallite size is strongly hindered by the absence of proper low q_z standard that would allow to identify the line broadening within a diffraction pattern due to the experimental setup in use.

(a)

(b)

(c)
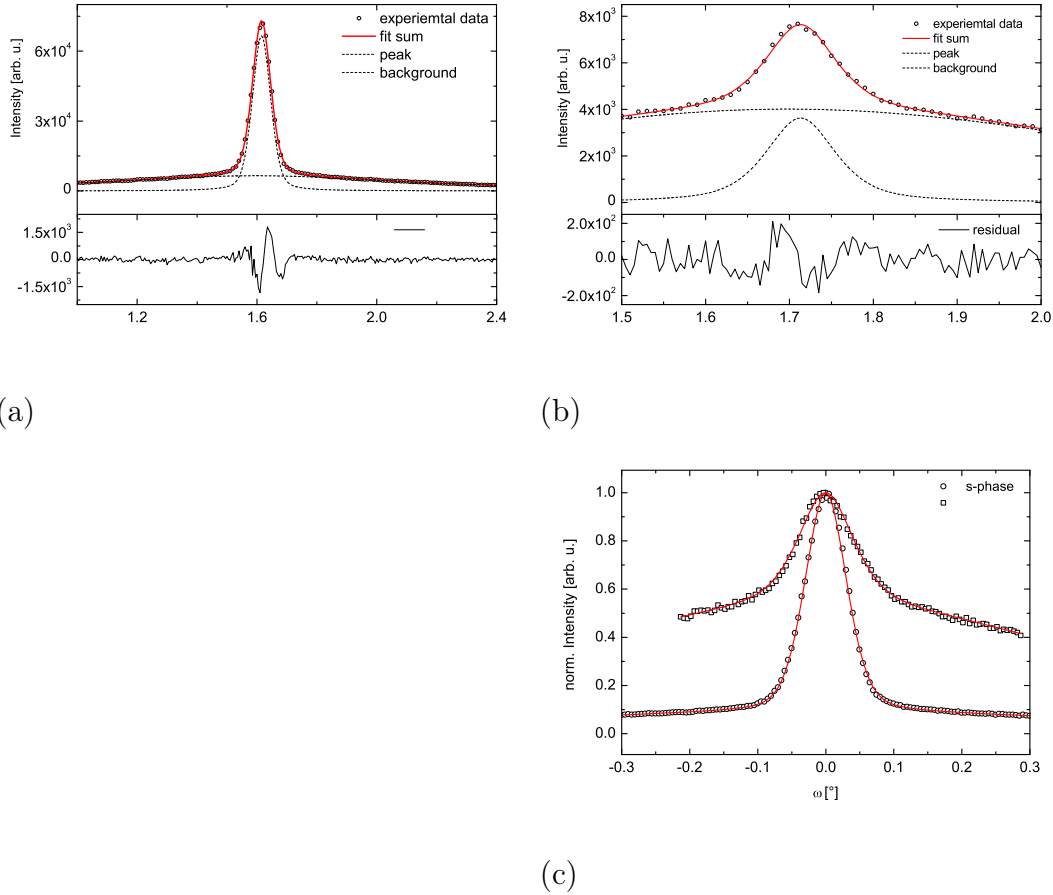
Figure 5.2: X-ray rocking scan on drop-casted film with an evaporation time of about $2\,min$. (a) s-phase (b) a-phase (c) normalized and corrected according equation 2.3.

Rocking Curve   The 2Θ circle was fixed to the centroid position $2\Theta_0$ of the Bragg peak $(002)^a$, and $q_z = 2.28\,nm^{-1}$ respectively, while the sample is tilted on the Θ circle in the vicinity of the Bragg angle Θ_0. The achieved rocking curves or ω-scans for the two phases are shown in Figure 5.2(a) and (b). The rocking curves $I_{rc}(\omega)$ are symmetric around $\omega = 0$ for both the s- and a-phase, i.e. the majority of crystallites is preferentially oriented with respect to the substrate normal and are therefore *fiber textured.* The best fit of the patterns reveals a FWHM of $2\omega_s = 0.07°$ for the s-phase

type	phase	Θ_0 [°]	$\pm\Theta_0$	2ω [°]	$\pm 2\omega$	η	$\pm\eta$	I_0 [arb.u.]	$\pm I_0$	I_U [arb.u.]	$\pm I_U$
PV	s	1.62	0.01	0.07	0.01	0.30	0.01	66500	160	6510	80
PV	a	1.71	0.01	0.1	0.01	0.60	0.15	3600	190	4000	170

Table 5.3: List of fitted peaks from rocking scans shown in 5.2. Where Θ_0 is the centroid position the Θ circle, 2ω the FWHM, η the weight parameter, I_0 the amplitude and I_U the maximum of the Background,.

and $2\omega_a = 0.1°$ for the a-phase. Compared to the a-phase the s-phase has a smaller 2ω and therefore is more well textured. Additionally the ratio of background to amplitude is a hundred time smaller even the specular peak is 17 times higher. This is clearly represented in Figure 5.2(c).

XRD   At a higher scanning range additional higher order reflection peaks are observed in the the pattern (figure 5.3).
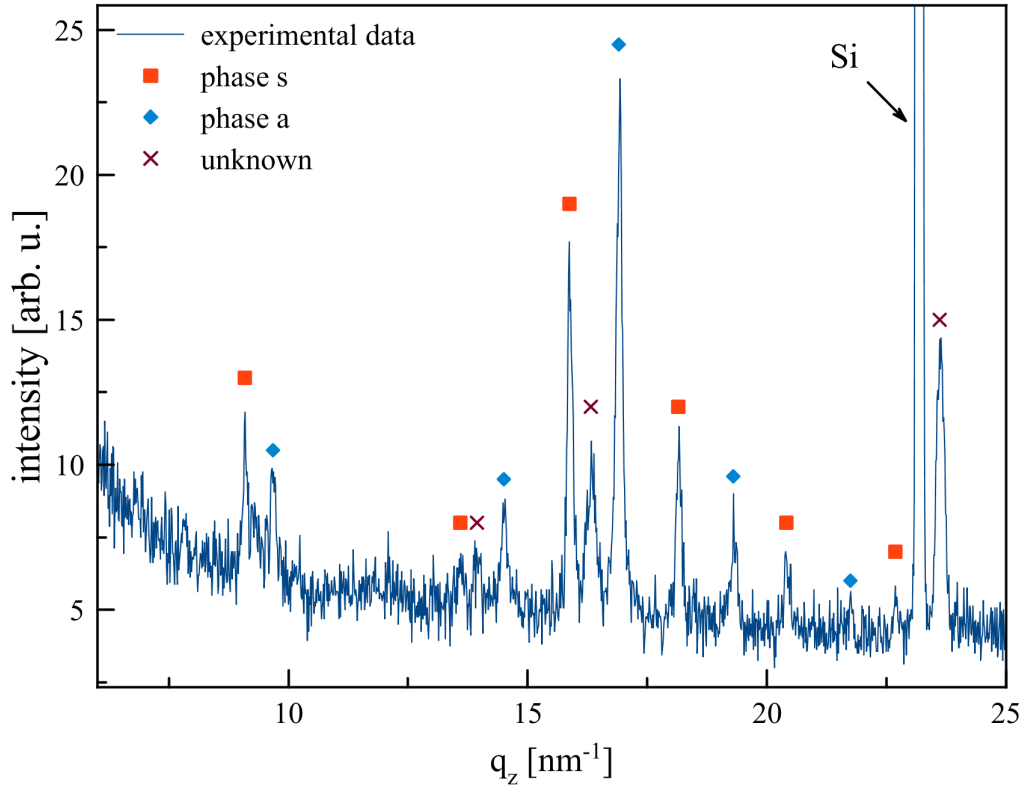
Figure 5.3: X-ray Diffraction (XRD) specular scan on a drop-casted film with an evaporation time of $\sim 2\,min$. Higher order reflection peaks of both the s-phase and the a-phase are observed. The marks sign the assigned phase. A red square indicates a peak of the s-phase and a blue diamond of the a phase. Peaks with unknown derivation are signed with a red cross..

Except three peaks all occurring peaks could be assigned. The list of the fitted peak positions and dedicated (hkl) is shown in table 5.4. The Bragg peak with the maximum at $23.156\,nm^{-1}$ is not a feature deriving from the film but belongs to the $Si(400)$ of the substrate. Arising from the higher harmonic content $(\lambda = 0,770299\,)$ of the incident beam. When multiplying the calculated lattice plane spacings d_{00l} with their multiple n_x one obtains the according distance for the (001) reflex. They should be ideally equal since its value is defined by the lattice plane spacing but they differ for different n_x. This reveals from an miss alignment called height error $\triangle\,2\Theta$ [4]. The sample is at a position with distance b below or above the optimal position and therefore a shift of the peak position occurs. The height error is decreasing with increasing Θ by $\triangle\,2\Theta = -\frac{2b\cos\Theta}{R}$ where R is the distance between detector and center of rotation. Taking into account the height error the lattice spacing is $d_{001} = (2.770 \pm 0.001)\,nm$. Defined by its peak position $q_z = (2.268 \pm 0.001)\,nm$.

Figure 5.4 shows the measured and simulated peaks[3] of the single crystal structure introduced in chapter 4. The intensities are normalized to the strongest reflex.
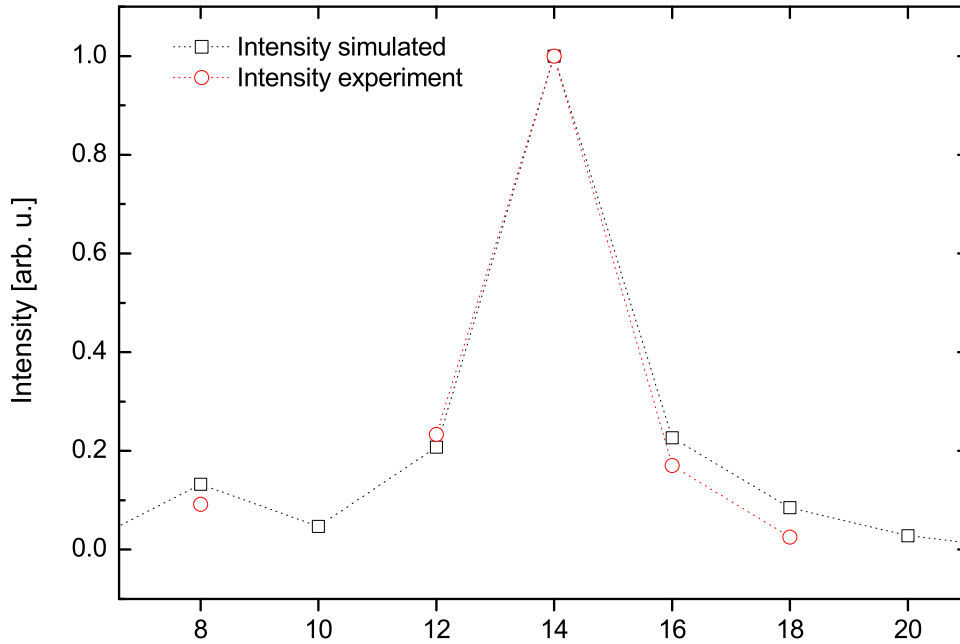
Figure 5.4: Comparison of simulated intensities from crystal structure and measured intensities where L is the L'th order. The intensities are normalized relative to the $(0\,0\,14)$ reflection.

---

[3]Simulation was done with the program POWDER CELL in Version 2.3.

Type	$2\Theta\,(°)$	Area	phase	$q_z\,(nm^{-1})$	$d\,[nm]$	$n_s\left(\frac{q_z}{27.77}\right)$	$n_s \cdot d\,[nm]$	$n_a\left(\frac{q_z}{25.96}\right)$	$n_a \cdot d\,[nm]$	$n_b\left(\frac{q_z}{25.46}\right)$	$n_b \cdot d\,[nm]$
PV	12.79	11	s	9.087	0.691	4.0	2.766	3.8		3.7	
PV	13.62	8	a	9.675	0.649	4.3		4.0	2.598	3.9	
PV	19.18	5	s	13.592	0.462	6.0	2.774	5.6		5.5	
PV	19.68	6	?	13.941	0.451	6.1		5.8		5.6	
PV	20.48	19	a	14.502	0.433	6.4		6.0	2.600	5.9	
PV	22.45	44	s	15.876	0.396	7.0	2.770	6.6		6.4	
PV	23.09	29	?	16.322	0.385	7.2		6.7		6.6	
PV	23.92	83	a	16.905	0.372	7.5		7.0	2.602	6.9	
PV	25.71	24	s	18.150	0.346	8.0	2.769	7.5		7.4	
PV	27.37	14	a	19.299	0.326	8.5		8.0	2.605	7.8	
PV	28.98	8	s	20.411	0.308	9.0	2.771	8.4		8.3	
PV	30.93	2	a	21.749	0.289	9.6		9.0	2.600	8.8	
PV	32.30	3	s	22.689	0.277	10.0	2.769	9.4		9.2	
PV	32.99	1293	Si	23.156	0.271	10.2		9.6		9.4	
PV	33.66	55	?	23.615	0.266	10.4		9.8		9.6	

Table 5.4: List of fitted peaks of the pattern shown in 5.3.

The good agreement supports the assumption that the a-phase is the same phase as the known structure.
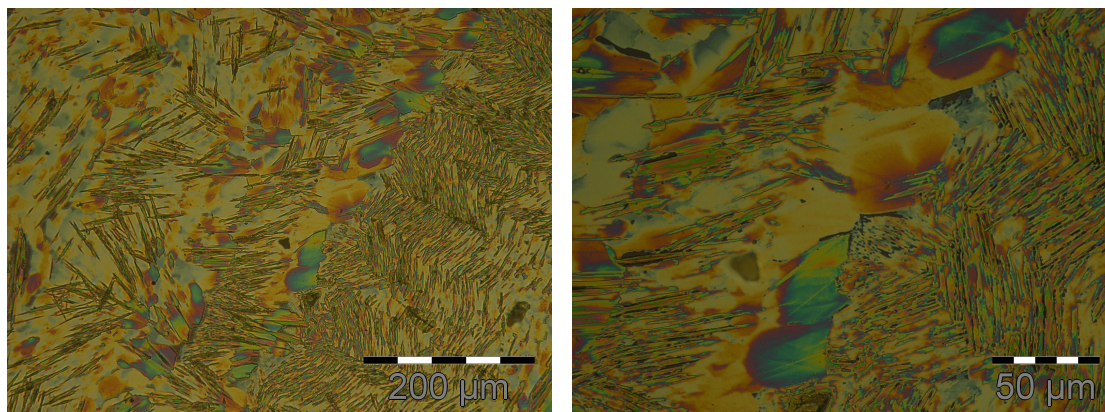
(a)   (b)

Figure 5.5: Pictures revealed from optical light microscopy of sample (0011) with (a) 20x magnification (b) 50x magnification. There are small needles and large flat areas

Optical Light Microscopy   The crystallites on the substrate show a needle like morphology and large flat areas (figure 5.5). The drying process works like this. The solution at the start is like a big fat drop covering the whole substrate. As the solvent evaporates this spheroid drop gets smaller until its kind of flat. Then it starts drying from the borders to the center and a round disk gets smaller and smaller. On some positions the drop remains and after a short time rapidly gets smaller. The crystallization process at this stage is very fast and happens within some seconds. It was not possible to distinguish between when the flat areas appear and at which stage the needles grow. This indicates a very high solubility of the material since most of the solvent volume allready has vanished before a structure is visible. Additionally the crystallites tend to have a preferred direction according to the fluid flow (figure 5.5(b)).

5.1.2.2 Preparation II

The shown results in this subsection where obtained from the sample with the identification number (0012). It was produced from then same solution like above with a concentration of $1.07\,mg/ml$. One dome was put fully over the sample resulting in an evaporation time of $t_e \sim 12\,min$. The necessary parameters to evaluate the concentrations are given in table 5.1.

XRR In difference to the pattern from sample (0011) a fit consisting of three simultaneous Gaussian distribution functions are required to fit the experimental data shown in figure 5.6.
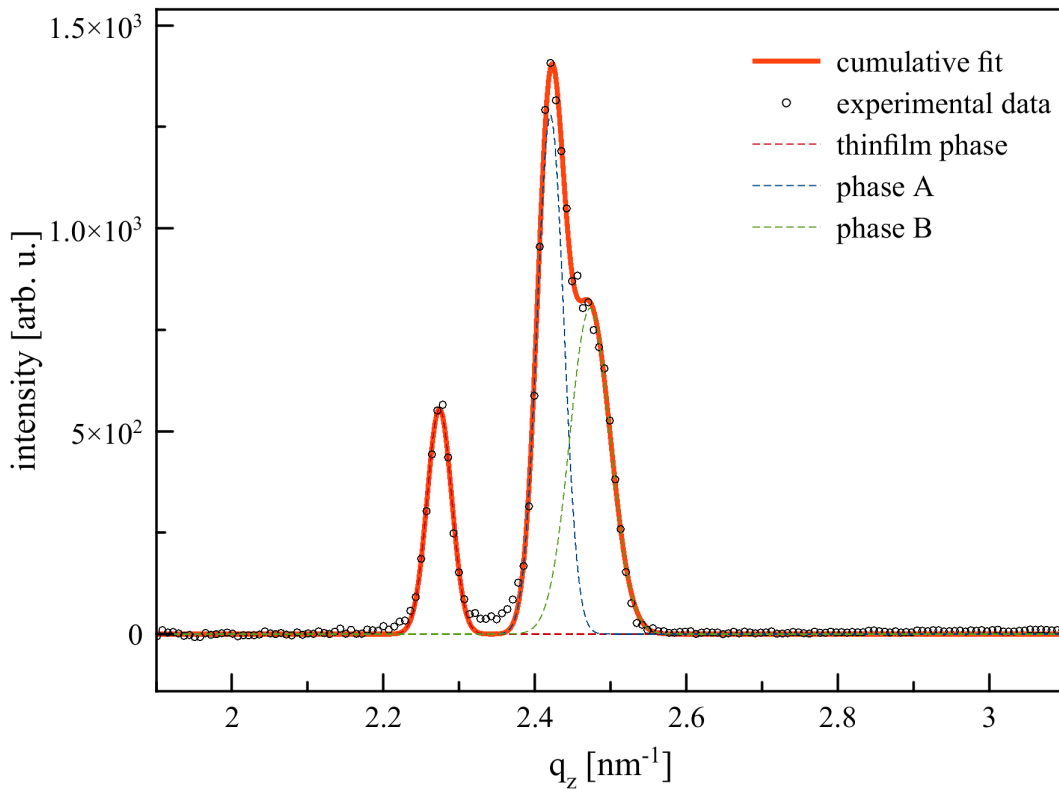
Figure 5.6: P II

The first Bragg peak reveals a peak at position $q_z = 2.28\,nm^{-1}$ corresponding to a real space lattice plane distance of $2.77\,nm$ which is relay close to the maximal theoretical extension of a DH3T molecule of $2.8\,nm$; see section 4.2. And is identified as the s-phase. The Bragg peak with the maximum at $2.42\,nm^{-1}$ is again the $(002)^a$ reflex from the *alpha phase* (a-phase). The new additional phase now defined by its peak position at $q_z = 2.48\,nm^{-1}$, from now on is named b-phase. The extracted

peak position and the full width at half maximum values for each Bragg peak is summarized in Table 5.5.

phase	q_z^0 (nm^{-1})	$\pm(nm^{-1})$	2ω (nm^{-1})	$\pm(nm^{-1})$	I_0 $(arb.\,u.)$	$\pm(arb.\,u.)$
s	2.27	0.01	0.04	0.01	556	12
a	2.42	0.01	0.04	0.01	1279	26
b	2.48	0.001	0.06	0.01	803	12

Table 5.5: fitting parameters from data shown in figure 5.6

The evaluation of the peaks reveal similar peak width for the a- and s-phase but is slightly higher for the new b-phase. Compared to the sample (0011) the amplitude of of the s-phase got smaller and even the width. The grain size is proportional to the width and the amplitude to the overall scattering volume. Therefore the grains got bigger but less. In figure 5.7 there are few to now flat areas any more, indicating that this "flat" morphology can be connected to the s-phase.
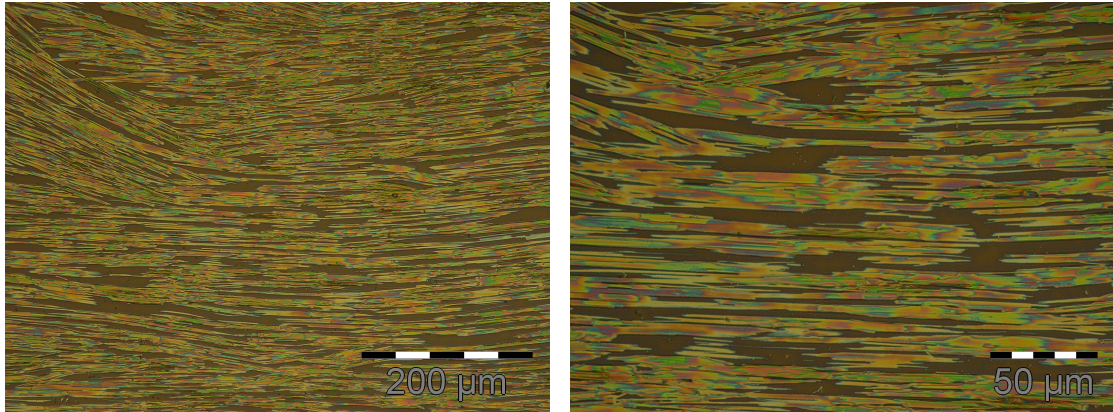
(a)   (b)

Figure 5.7: Pictures revealed from optical light microscopy of sample (0012) with (a) 20x magnification (b) 50x magnification. There are still needles but nearly no flat areas.

The a-phase amplitude instead got much higher and the width smaller. As mentioned above the intensity of the Bragg peak corresponds to the amount of crystallites within the sample and reveal a 2 times more intense Bragg peak for the a-phase compared to the s-phase. This suggests that the area containing crystallites in the a-phase now is bigger. So we should see less of the flat areas and more of something else. There are more needle like structures, but it is not obvious to which phase the needle belong. The drying process was the same as described for the sample (0011).

5.1.2.3 Preparation III

The shown results in this subsection where obtained from the sample with the iden-
tification number (0013). It was produced from then same solution like above with
a concentration of $1.07\,mg/ml$. Two domes were put over the sample resulting in
an evaporation time of $t_e \sim 30\,min$. The necessary parameters to evaluate the
concentrations are given in table 5.1.

The pattern from sample (0013) shows similar features as obtained for sample (0012)
(figure 5.8).
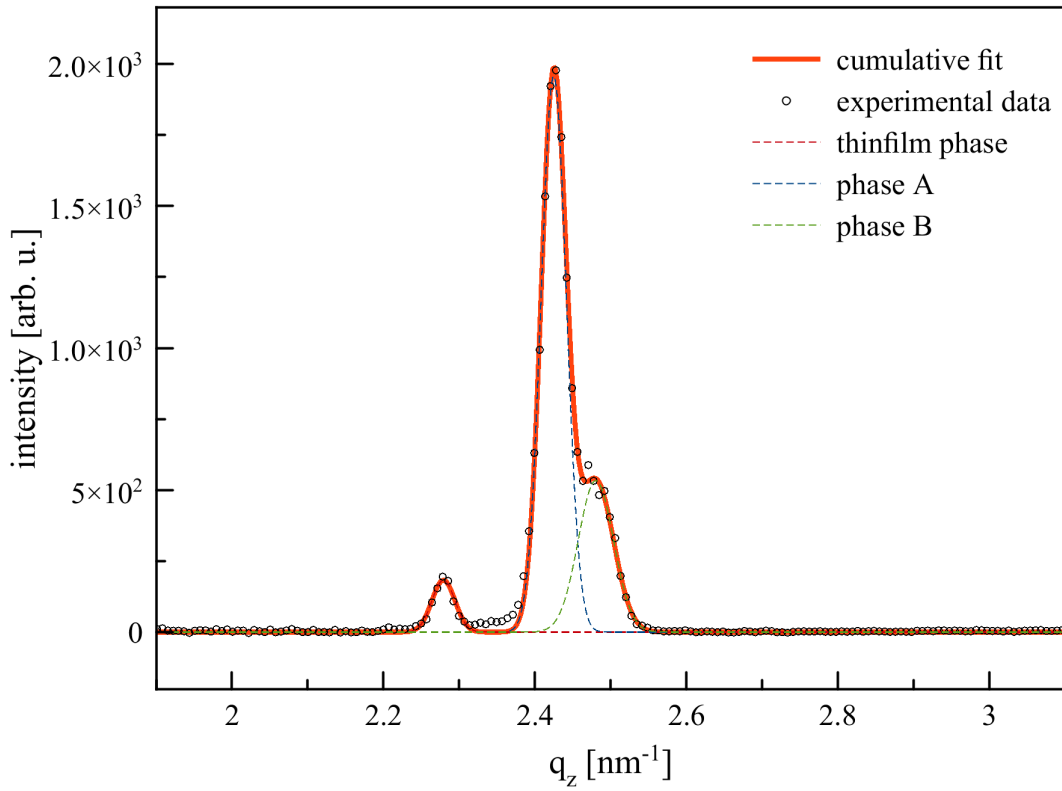
Figure 5.8: P III

The extracted peak position and the full width at half maximum values for each
Bragg peak is summarized in Table 5.6.

phase	$q_z^0\,(nm^{-1})$	$\pm(nm^{-1})$	$2\omega\,(nm^{-1})$	$\pm(nm^{-1})$	$I_0\,(arb.\,u.)$	$\pm(arb.\,u.)$
s	2.28	0.01	0.04	0.01	183	15
a	2.42	0.01	0.04	0.01	1960	17
b	2.48	0.01	0.06	0.01	534	13

Table 5.6: fitting parameters from data shown in figure 5.8

Again three peaks where observered and are identified as the s-phase, a-phase and b-phase.

The evaluation of the peaks reveal equal peak width for the a-phase, b-phase and s-phase compared to the previous produced. Compared to the sample (0012) the amplitude of the s-phase again got smaller. The a-phase amplitude instead got much higher and now is 11 times more intense compared to the s-phase. There are more and bigger needle like structures, and one could assume that the a- or b-phase is connected to the needle like structure.

The drying process was different from the previous one. The solution on the substrate at the start again was like a big fat drop covering the whole substrate. As the solvent evaporates this spheroid drop gets smaller until its flat. On the opposite it doesn't start drying from the borders to the center but stays flat. The liquid surface went silver and stayed in this state for a some time. At a sudden on some few positions the surface got some sparkles. This lasted for some time. Then a area in the middle of the sample went dry and the regions of the border stayed wet. Then after some time another crystallization process started. Needles started to grow at randomly distributed spots and grew straight forward in a direction each on a line. This went as fast as described for sample (0011). This behavior indicates that some part of the material stays dissolved until a critical concentration is reached and then the needles start to grow. The resulting structures are shown in figure 5.9.
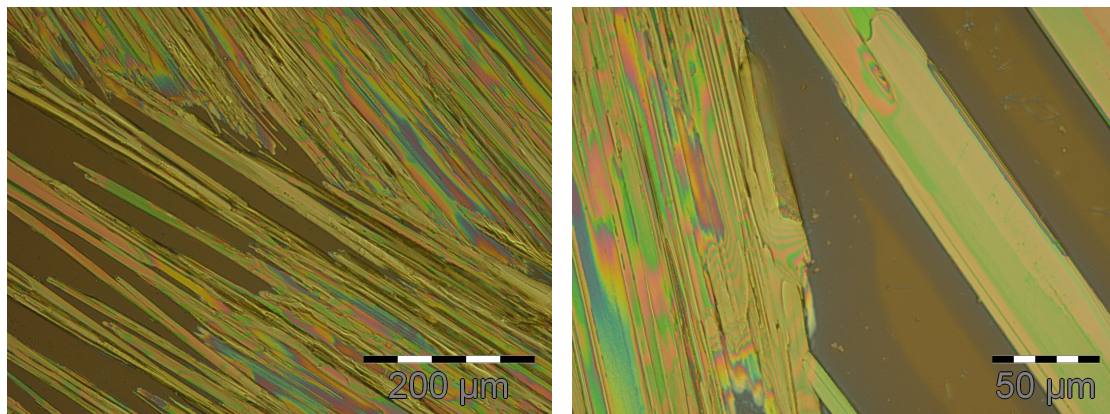
(a)   (b)

Figure 5.9: Pictures revealed from optical light microscopy of sample (0012) with (a) 20x magnification (b) 50x magnification. The crystallites are big needles and nearly no large flat areas. Additionally small spots are visible.

5.1.2.4   Preparation IV

The shown results in this subsection where obtained from the sample with the iden-
tification number (0025). It was produced from a solution with a concentration of
$0.92\,mg/ml$. Two domes were put over the sample and an additional PTFE gas-
ket was applied resulting in an evaporation time of $t_e \sim 130\,min$. The necessary
parameters to evaluate the concentrations are given in table 5.7.

$solvent$	THF	
ρ	0.889	g/cm^{-3}
$DH3T$	0.0012	g
m_S	1.165	g
V_S	1.31	ml
$wt\,\%$	0.10	$\%$
$\frac{wt}{V}\,\%$	0.92	mg/ml

Table 5.7: Parameters for calculating the concentration of the used solution for sam-
ple (0025). ρ …density of solvent, m_S … mass of solvent, V_s … volume of solvent,
$wt\,\%$ … mass percentage, $\frac{wt}{V}\,\%$ … mass-volume percentage. The used solvent was
Tetrahydrofuran(THF).

In the pattern revealed from the measurements on the sample (0025) shown in
figure 5.10 only two peaks are observeable. The amplitude connected to the s-phase
is completely vanished.

(a)   (b)
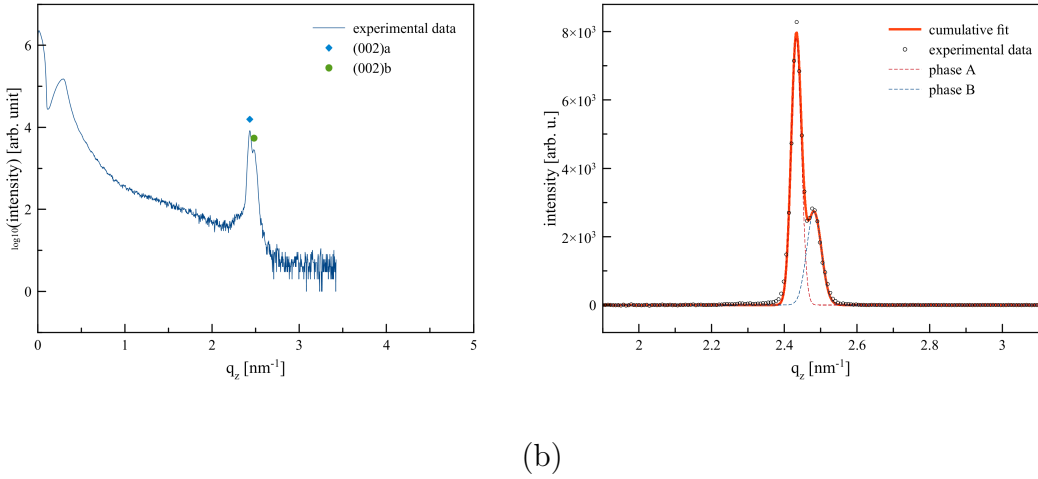
Figure 5.10: X-ray reflectivity scan on drop-casted film prepared from THF solution
of sample (0025). (a) logarithmic plot (b) linear plot with fitted curves.

The additionally intensity increase of the a-phase and the b-phase indicate that
subsequently reducing the processing speed / evaporation time results in a larger

scattering volume from phase a and b. The extracted peak position and the full
width at half maximum values for each Bragg peak is summarized in Table 5.8.

phase	$q_z^0\,(nm^{-1})$	$\pm(nm^{-1})$	$2\omega\,(n,m^{-1})$	$\pm(nm^{-1})$	$I_0\,(arb.\,u.)$	$\pm(arb.\,u.)$
a	2.43	0.01	0.03	0.01	7849	36
b	2.48	0.01	0.06	0.01	2726	28

Table 5.8: Fitting parameters from data shown in figure 5.10

Additonally to the vanishing of the s-phase amplitude an new feature can be observed
(figure 5.10(b)). In the range between $0.5\,nm^{-1} - 3\,nm^{-1}$a curvature occurs. This
long oscillation reveals from the coherent interference (Kiessig fringe) of a very thin
layer. The length of the fringe is approximately $2.2\,nm^{-1}$ revealing in an rough
estimation of the layer thickness of approximately $\sim 2.8\,nm$. This is in the region of
the extension of an upright standing molecule. Though the minimum of the fringe
is not good pronounced indicates that the layer doesn't fully cover the substrate
surface.

At a higher scanning range additional higher order reflection peaks are observed in
the pattern (figure 5.11).
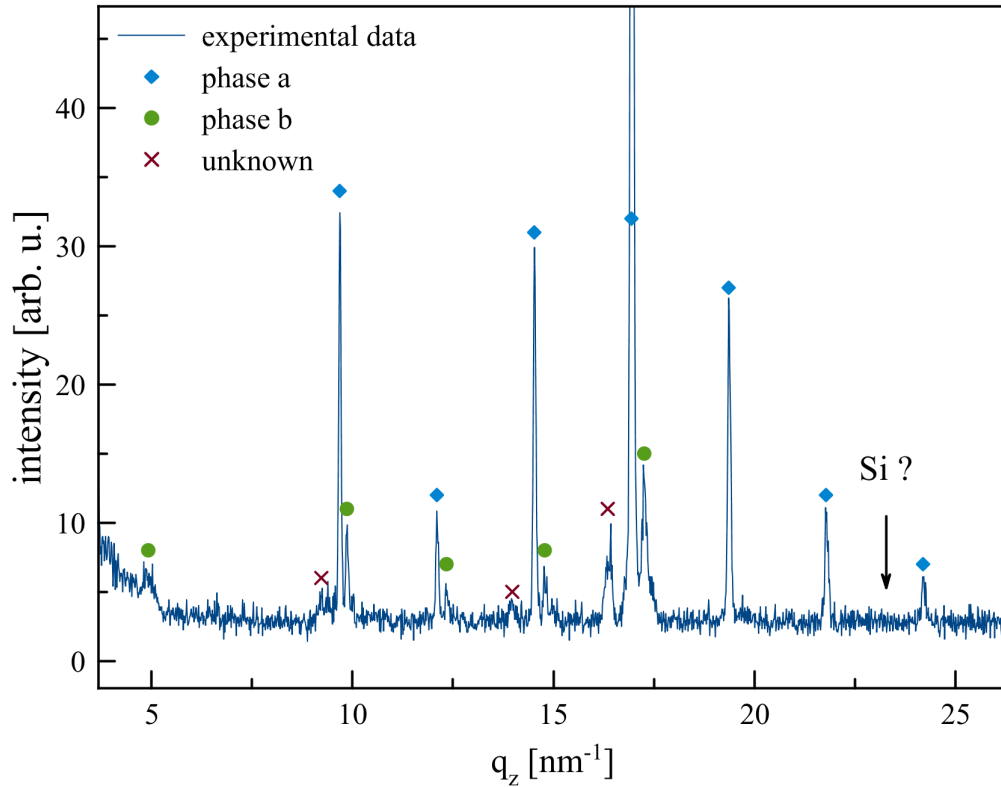
Figure 5.11: X-ray diffraction pattern of the drop-casted films no sample (0025). The marks are set on the theoretical positions of the according phase. .

The list of the fitted peak positions and dedicated (hkl) is shown in table 5.9. The Si(400) peak is absent because of a small missalignment and is not strongly affecting the qualitative results.

The drying process was different from the previous ones. The solution on the substrate at the start again was like a big fat drop covering the whole substrate. As the solvent evaporates this spheroid drop gets smaller until its flat. On the opposite to the previos samples no part was drying. So the substrate seem to be wetted completely, taking into account that we now have a thin layer on the substrate. The liquid surface went silver and stayed in this state for a long time. At a sudden on some few positions the surface got some sparkles. This lasted for some time. And then suddenly another crystallization process started. Big needles started to grow at randomly distributed spots and grew straight forward in a direction each on a line. This went as fast as described for sample (0011). This behavior indicates that some part of the material stays dissolved until a critical concentration is reached and then the needles start to grow. The resulting structures are shown in figure 5.12.

Type	$2\Theta\,(°)$	Area	phase	$q_z\,(nm^{-1})$	$d\,[nm]$	$n_s\left(\frac{q_z}{27.77}\right)$	$n_s \cdot d\,[nm]$	$n_a\left(\frac{q_z}{25.96}\right)$	$n_a \cdot d\,[nm]$	$n_b\left(\frac{q_z}{25.46}\right)$	$n_b \cdot d\,[nm]$
PV	6.91	21	b	0.492	12.773	2.2		2.03		1.99	25.546
PV	12.99	6	?	0.922	6.811	4.1		3.81		3.74	
PV	13.63	40	a	0.968	6.490	4.3		4.00	25.962	3.92	
PV	13.89	11	b	0.986	6.372	4.3		4.07		4.00	25.489
PV	17.06	11	a	1.210	5.193	5.3		5.00	25.963	4.90	
PV	17.40	5	b	1.234	5.092	5.4		5.10		5.00	25.462
PV	19.73	5	?	1.398	4.496	6.2		5.77		5.66	
PV	20.51	39	a	1.452	4.327	6.4		6.00	25.961	5.88	
PV	20.88	8	b	1.478	4.250	6.5		6.11		5.99	25.501
PV	23.13	12	?	1.635	3.843	7.2		6.76		6.63	
PV	23.97	228	a	1.694	3.709	7.5		7.00	25.963	6.86	
PV	24.43	35	b	1.726	3.641	7.6		7.13		6.99	25.484

Table 5.9: List of fitted peaks in the pattern shown in 5.11.The sample was prepared with method P IV that yields to a drying time of about 3 hours.
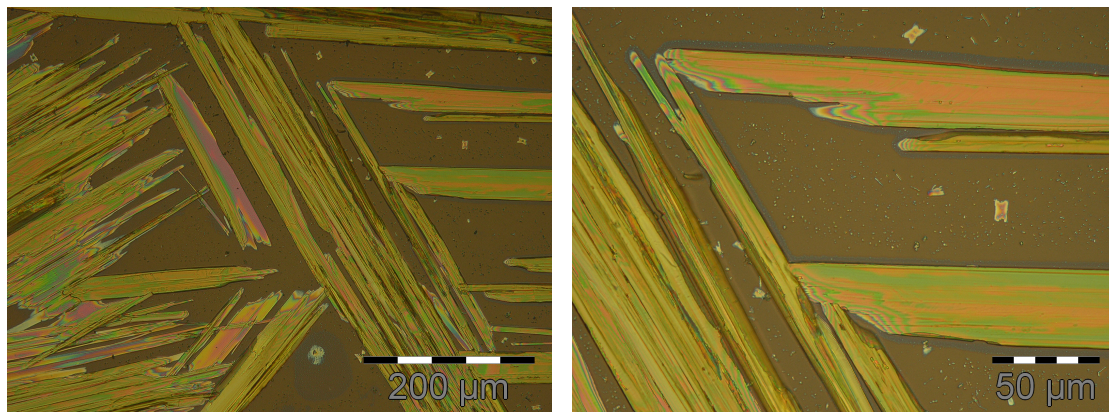
(a)   (b)

Figure 5.12: (a) 20x (b) 50x

5.1.2.5   Discussion

The experimental results above show that the molecule DH3T at least form three different types of crystallographic phases. These phases are clearly identified by specular x-ray diffraction considering the 002 Bragg peaks denoted with s, a and b for the three different phases. The a - phase can be related to the phase observed in the single crystal as the Bragg peak positions (figure 5.3) and the according intensities (figure 5.4) are very close to the theoretical values.

The results indicate that preparation of the films has a strong impact on the formation of specific polymorph phases. Comparing the results summarized in table 5.10 indicates that at high evaporation rates the s - phase appears, while at low evaporation rates the a–phase and the b-phase is formed (figure 5.13).
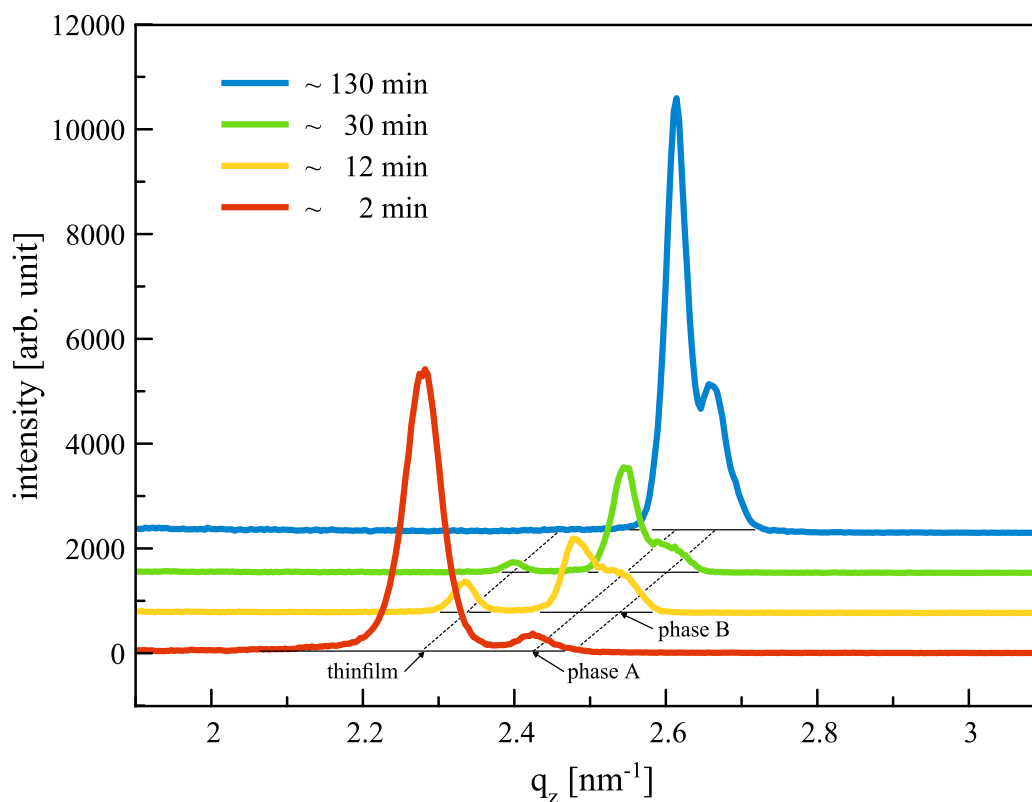
Figure 5.13: : X-ray diffraction specular scans on drop-casted films prepared by different evaporation time of the solvent

Preparation	time	$I_0(s-phase)$	$I_0(a-phase)$	$I_0(b-phase)$
P I	~ 2 min	523	30	0
P II	~ 12 min	56	128	80
P III	~ 30 min	18	196	54
P IV	~ 130 min	0	785	273

Table 5.10: Amplitudes resulting from different evaporation time of the solvent. Solvent used and amount of solution is the same for sample prepared by method P I to P IV, so amplitude of each phase can be compared. The structure factor is not known so comparing intensities between different phase is not allowed. 5.13

Further more the spendable material remaining on the substrate is nearly the same for all contemplated samples. Therefore the vanishing of the s-phase while decreasing the processing speed strongly indicates that the transition from the dissolved state to the a-phase and b-phase needs more time relative to the s-phase. Therefore the a-phase and the b-phase are assigned as *stable bulk* structures. Contrariwise a faster reduction of degree of freedom results in more contribution of s-phase grains within the film. The s–phase is somehow different; obviously it appears in connection with fast processing. The s – phase is formed in case of "fast" drop casting. It is assumed that the crystallization processes during the "fast" processing take place far from the thermodynamic equilibrium state compared with slow growth from solution. Therefore, it can be suggested that the s-phase represents a *metastable* crystal structure.

The drying process also is affected by the time the system has to settle since the liquid flow during the evaporation series changes. It is suggested that the wetting behavior changes caused by molecules adsorbed on the substrate surface and therefore changes the surface energy. This *weeting layer* causes a better wetting and the liquid covers larger areas. As a result a long oscillation occurs in the XRR pattern.

The morphologies of the four different films are depicted in Figure 5.14. For all four samples the crystallites show typically a needle like morphology. The size of the crystals increases with the evaporation time of the solvent from fine needle like structures with a width from few μm up to $40\,\mu m$, for the samples with evaporation time 2 min. and 130 min., respectively. The length of the needles increases from several tenth of μm up to the mm regime. The large flat like areas dominating in (a) are getting less and smaller through the series . That indicates that this morphology can be identified as the s-phase. For the a-phase and b-phase there is no clear difference in the morphology of these two different polymorph phases observed.
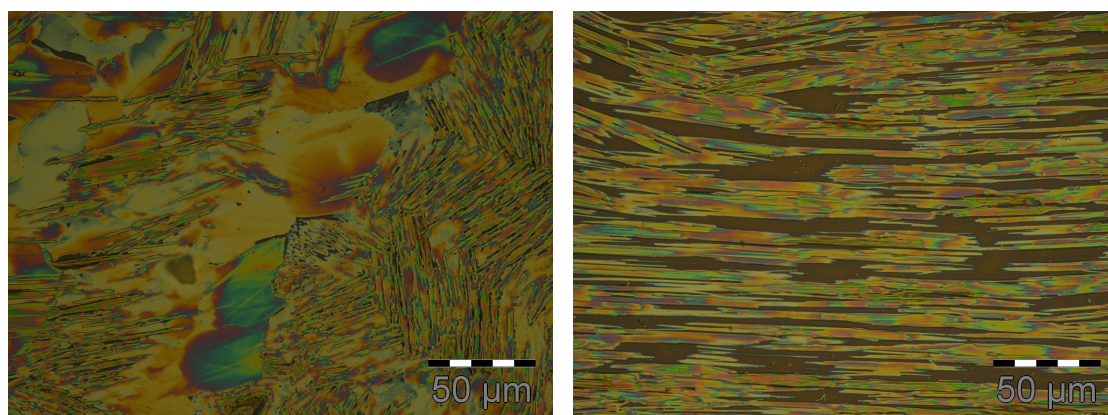
(a) $2\,min$

(b) $12\,min$
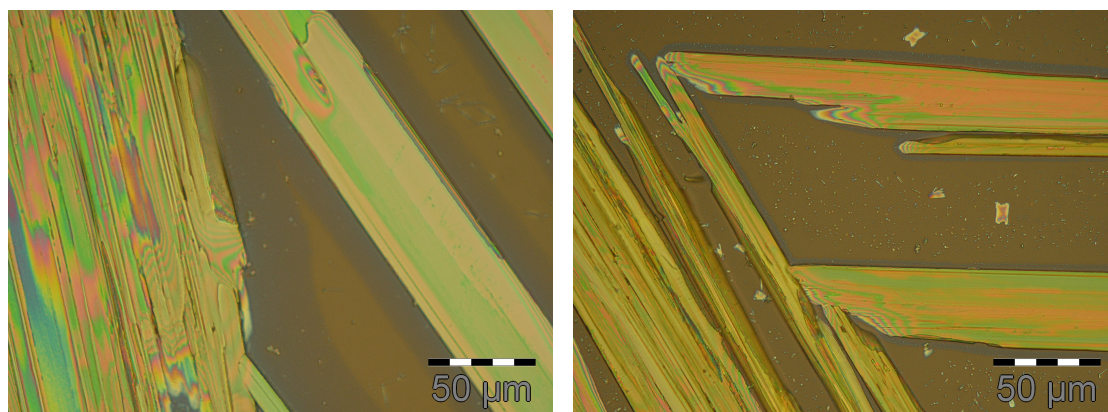
(c) $30\,min$

(d) $130\,min$

Figure 5.14: Optical light microscopy of drop casted films prepared by different times of solvent evaporation
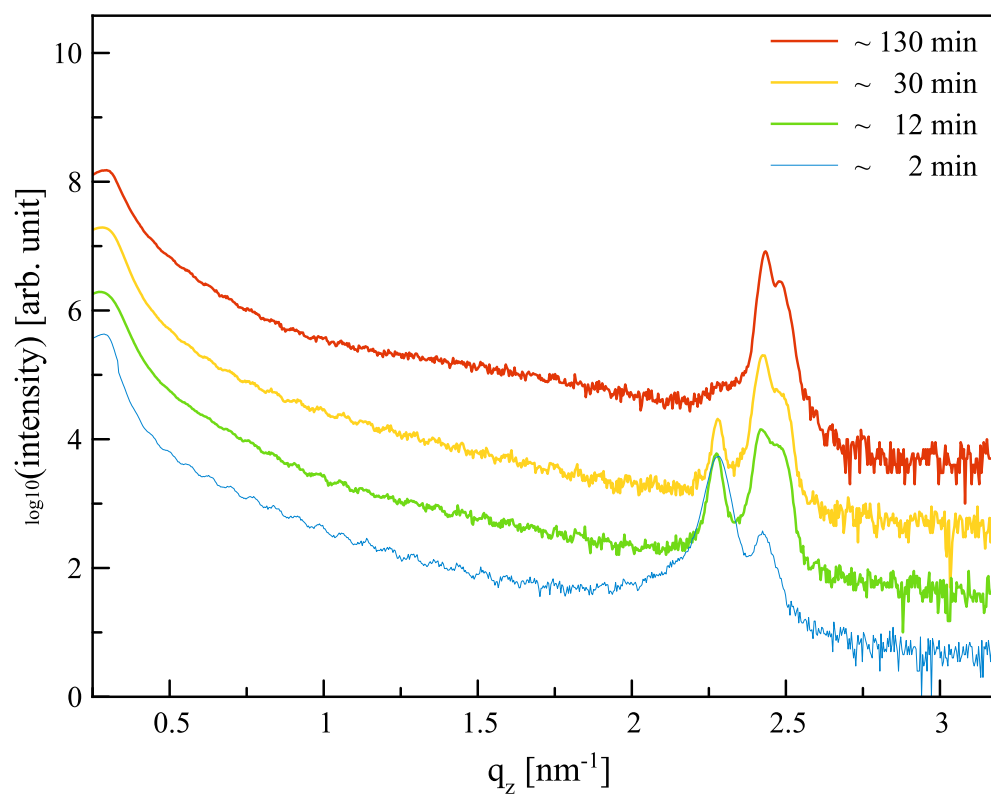
Figure 5.15: : X-ray reflectivity scans on drop-casted films prepared by drop casting. Different evaporation time of the solvent generates different polymorphs of DH3T. The faster the processing the more Thinfilm phase appears and vice verse.

5.2 Spincoating

In the previous subsection a dependents of the evaporation rate was indicated. To falsify this a method like spin coating was applied. During the spin coating process the solvent evaporates in subseconds. Additionally the film forming properties of DH3T on the fast removement of the solvent is investigated on these films.

DH3T is dissolved in THF with concentrations ranging from $0.2\,mg/ml$ to $2.8\,mg/ml$ to obtained different film thickness as mentioned in section 3.3. Thin films were produced with the same spin parameters for all samples; the initial spin speed was 1000 rpm for 9 s followed by 1500 rpm for 30 s. Spin Coater in charge was the KW-4A manufactured by CHEMAT TECHNOLOGY.

5.2.1 Spincoated DH3T films

The measured x-ray reflectivity curves of the pure substrate and the various spin coated DH3T films are shown in Figure 5.16. The fast oscillation in the experimental curves are oscillations occurring due to the thermal grown oxide of the silicon wafer with a layer thickness of $120\,nm$. At a concentration of $0.21\,mg/ml$ the reflectivity curve shows a clear low frequent oscillation indicating the formation of a defined thin layer. As the concentration is increased to $0.66\,mg/ml$ the low frequency oscillation is vanished and the presence of a Bragg peak at $q_z = 2.28\,nm^{-1}$ is noted; the d-spacing calculated from the the peak position reveals $d = 2.755\,nm$ which correspond to the 002 reflection of the thin film phase of DH3T. For concentration higher than $0.21\,mg/ml$ the peak intensity increased with increasing concentration suggesting the formation of more extended DH3T crystallites on the silicon wafer. For the two most concentrated solutions, additional Laue oscillation next to the Brag peak are observed. Laue oscillation in general are only observed in films with a narrow crystallite extension distribution, i.e. most of the crystallites have similar size. Note that there are no indicators that another phase is present within the films.
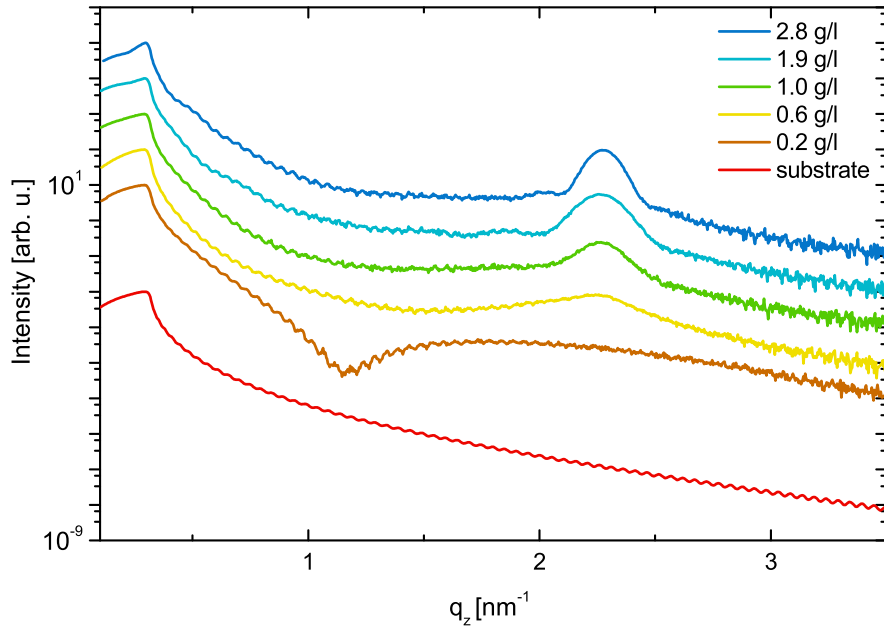
Figure 5.16: XRR spectra for the silica substrate and the spincoated DH3T film produced from various concentrations. The curves are shifted for clarity.

5.2.2   Fitting

For the evaluation of the XRR curves model fits with the Parratt's formalism are used according to [31]. The reflectivity is calculated by taking into account the electron density of the substrate and the electron density distribution of the DH3T film. The DH3T film was modeled as standing molecules with alkyl chains and thiophene units separated along the substrate surface normal. The coverage of each layer was taken into account by multiplying the common basis of the DH3T layer by a factor ranging from 0 to 1. The experimental data together with the best fits are shown in Figure 5.17. For the DH3T films a good agreement of the fits and the experimental data is observed. The revealed fits are shown in figure 5.17.
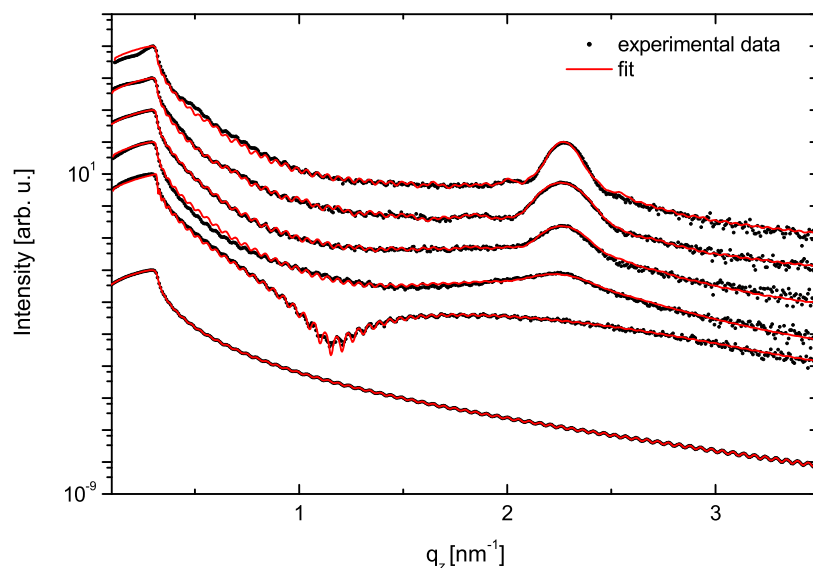
Figure 5.17: (a) X-ray reflectivity of different thin films of the molecule dihexyl-terthiophene (DH3T) together with best model fits. Films are prepared by spin coating from tetrahydrofuran solutions with concentrations of 2.79 mg/ml, 1.91 mg/ml, 1.09 mg/ml, 0.66 mg/ml and 0.21 mg/ml (from top to bottom). The lowest curve represents a scan on a plane substrate. Curves are shifted for clarity.

5.2.2.1   Substrate

As base material for the substrates (100) cutted thermal oxidized silicon wafers were used. The wafers were cutted in to small pieces of about $1,5 \times 1,5\,cm$ and afterwards cleaned in an ultra sonic isopropanol bath for about 2 hours. After the bath they were blown clear with CO_2. This procedure was applied to all substrates to minimize contamination by unmeant particles on the surface. This was checked by AFM. The results are shown in figure 5.19. A fit of the reflectivity curve shown in figure 5.18 revealed a layer thickness of $\sim 120\,nm$ of the thermal grown oxide on the silicon wafer.
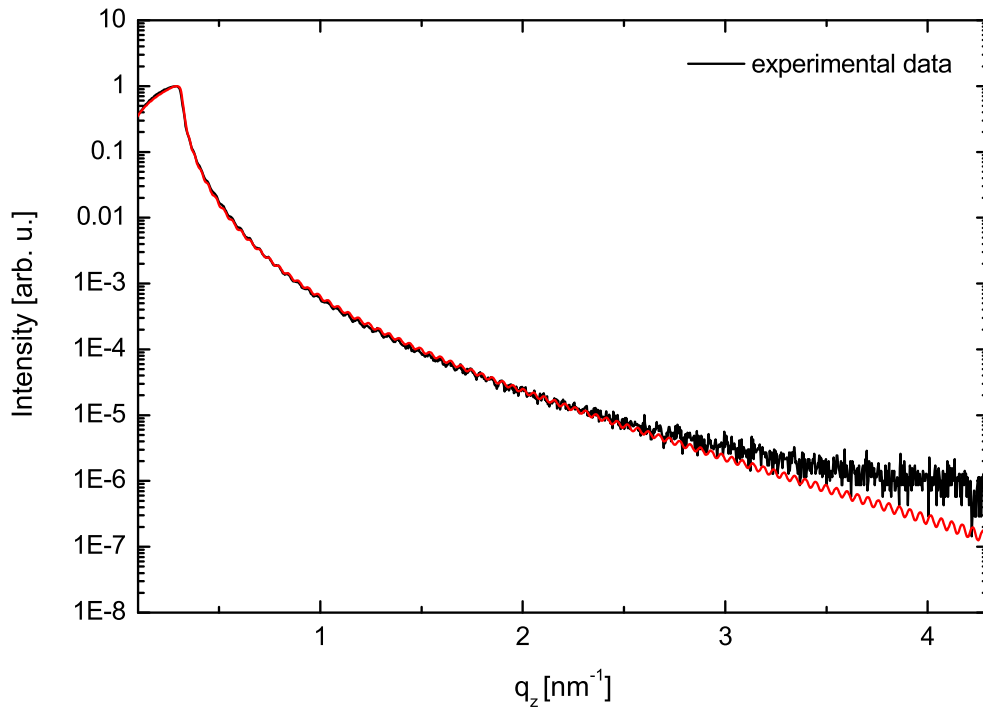
Figure 5.18: X-ray reflectivity scan on plane substrate

(a)   (b)
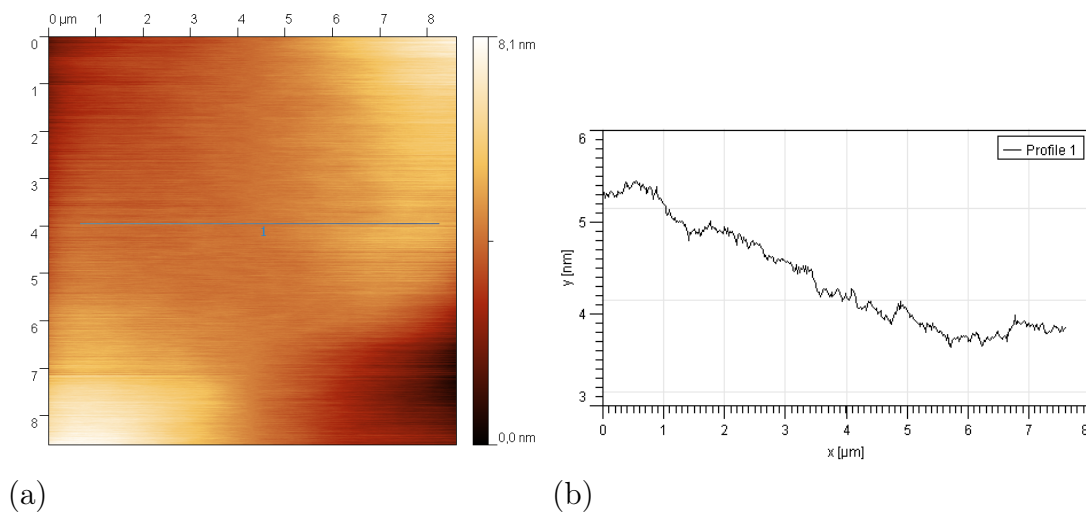
Figure 5.19: AFM image of pure substrate (a) and a corresponding heigth profile.

5.2.2.2 DH3T Thin Films

For the film produced from the 0.21mg/ml solution one layer was sufficient to fit the experimental data (figure 5.20). The coverage of this layer was 0.85 compared to a

fully covered layer (see Fig.5.17).
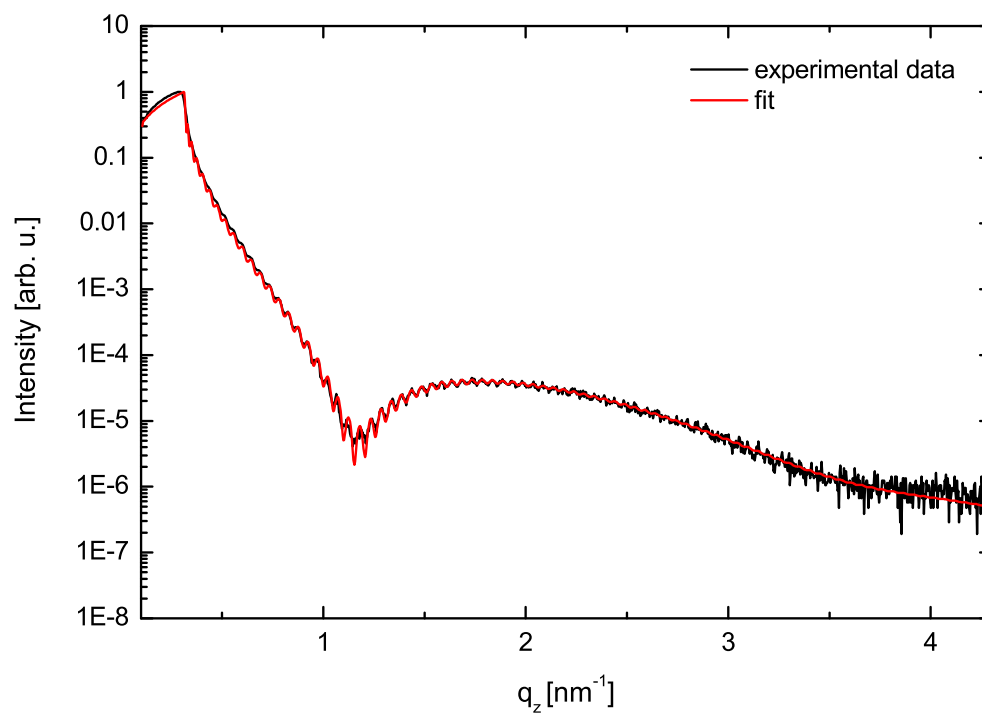
Figure 5.20: X-ray reflectivity scan on spin-coated film from $0.2\,mg/ml$ DH3T/THF

This corresponds to the AFM image of this film and is shown in figure 5.21.

(a)

(b)

(c)

(d)
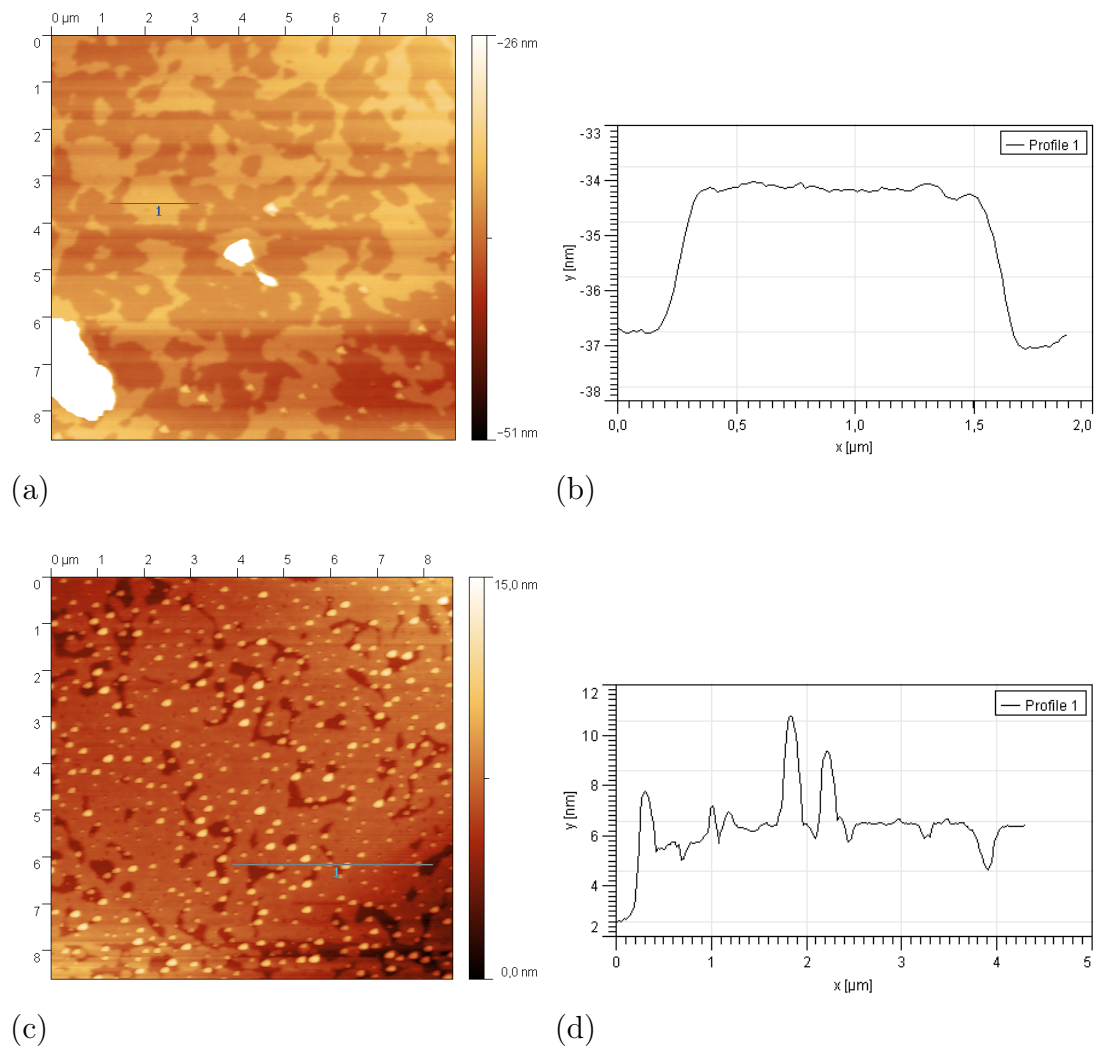
Figure 5.21: AFM image of the thinfilm produces from the $0.2\,mg/ml$ solution. (a) was mapped in the center area and (c) in the region of a boarder. (b) and (d) represent the line profile marked in the map.

The stepheight of the islands is in accordance with the d-spacing of the 002 reflection of DH3T thin film phase. The size distribution of the island and the island separation are randomly. For the sample produced from the $0.2\,mg/ml$ solution the layer closeset to the silicon substrate on top of the wetting layer was around 0.85. So it is nearly covering the whole substrate surface.

As the concentration is increased more layers had to be introduced to be able to fit the experimental data. In addition a wetting layer of $1.5\,nm$ and an electron density similar to the bulk DH3T had to be introduced between the DH3T film and the silicon wafer to achieve reasonable agreements of the fit and the experimental data. The resulting fitparameter are shown in table 5.11. The maximal number of layers required for the fit increased with increasing concentration; 8 layers were

$c\,(g/l)$	n	$h\,(nm)$	S_C
0.2	1	2.77	0.85
0.6	8	22.2	0.83
1.0	12	33.2	0.95
1.9	13	36.0	0.99
2.8	21	58.1	1.00

Table 5.11: Best fit results from the according pattern. c as the concentration, n the needed layers for the fit and the resulting thickness h, and S_c as the coverage.

required for the 0.66 mg/ml sample and 21 layers for the 2.8mg/ml sample. For the subsequent layers the coverage was decreasing; i.e with increasing height of an island the layer gets smaller. This corresponds to the AFM image shown in figure 5.22.

(a)   (b)
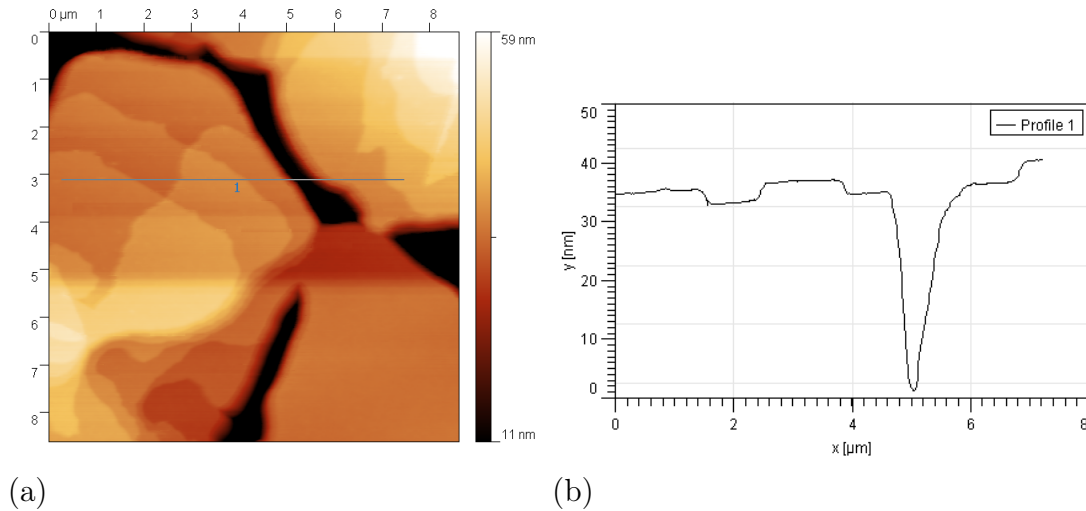
Figure 5.22: AFM image of the thinfilm produced from the 2.8 mg/ml solution. (a) Mapped in the center area. (b) represents the line profile marked in the map.

A full coverage for the first layer was present for the highest concentration of 2.8mg/ml.
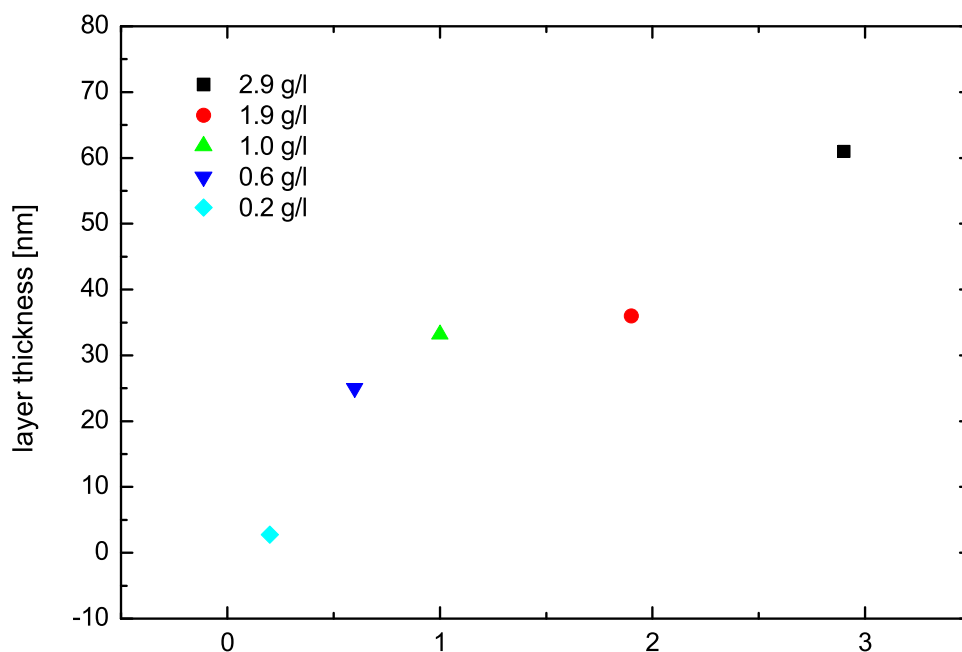
Figure 5.23: Evaluated film thickness resulting from spincoated films prepared from different concentrated solutions.

The relation between film height and concentration is shown in figure 5.23 and seems to be linear. This can be explained when taking into account that the remaining liquid film thickness before the evaporation is only determined by properties of the solvent due to the low concentration. Therefore the amount of remaining material is proportional to the concentration.

Grazing Incidence Diffraction (GID)   Figure 5.24 shows a GID map of a spin coated film with solution concentration of $4\,mg/ml$. The defined peaks indicate good in plane ordering of the molecules and that they are well fiber textured. A good first guess for the unitcell parameters is $a_1 = 3.056\,nm^-1, a_1 = 2.228\,nm^-1$ $a_3 = 5.560\,nm^-1$ and $\alpha_1 = \alpha_2 = \alpha_3 = 90°$. Assuming a herring bone structure reveals 64 molecules in the unit cell. So the average molecule distance in the direction of $a_1^s = 0.764\,nm$, $a_2^s = 0.557\,nm$ and $a_3^s = 2.78\,nm$.

Additionally features of the a-phase occur marked with red dots in figure 5.24.
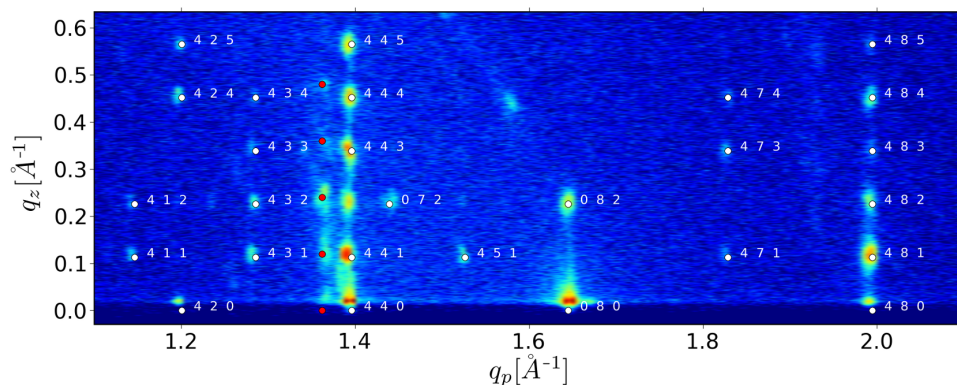
Figure 5.24: Indexed reciprocal space map of a spincoated film produced from a solution with concentration of about $4\,mg/ml$. The white spots mark the peaks of the thin film phase. Red spots mark peaks from the a-phase. The (442) peak is not marked for better readability.

5.2.2.3   Discussion

The XRR and AFM results reveal the formation of a sub monolayer structure of DH3T for a concentration of $0.21\,mg/ml$ in THF with the used spin parameters of $1000\,rpm$ for $9\,s$ and $1500\,rpm$ $30\,s$. The stepheight of the islands and the Bragg peak position is in accordance with the d-spacing of the 002 reflection of DH3T thin film phase. The size distribution of the island and the island separation are random and untypical for the film formation of small molecules at an interface. Especially if films are vacuum deposited a fractal type growth of the islands is observed with common size and separation distribution for all islands (See Fig. 5.25 left). This effect is usually addressed to limited molecule diffusion on the surface during the film deposition. However the DH3T film show remarkably similarities to solution deposited wetting structures of polymers. An example of F8T2 spin coated from xylene is shown in Fig. 5.25(right) revealing the formation of island with non common size and separation distribution. During the spin coating process the solvent evaporation occur fast resulting in spontaneous immobilization of the DH3T molecules and limit the molecule diffusion drastically. The arrangement of the molecules to adjacent molecules therefore is strongly determined by the solvent evaporation process and a structure similar to a wetting structure of a polymer film occurs.

As the concentration of DH3T in THF is increased the film morphology changes. The initial monolayer formation is exchanged by 3 dimensional terrace like structures. The step height is the same as for the monolayer regime revealing the same crystalline structure is present in the thicker films and the monolayer film. The XRR and the AFM images reveal a decrease in the coverage with increasing separation of the layer
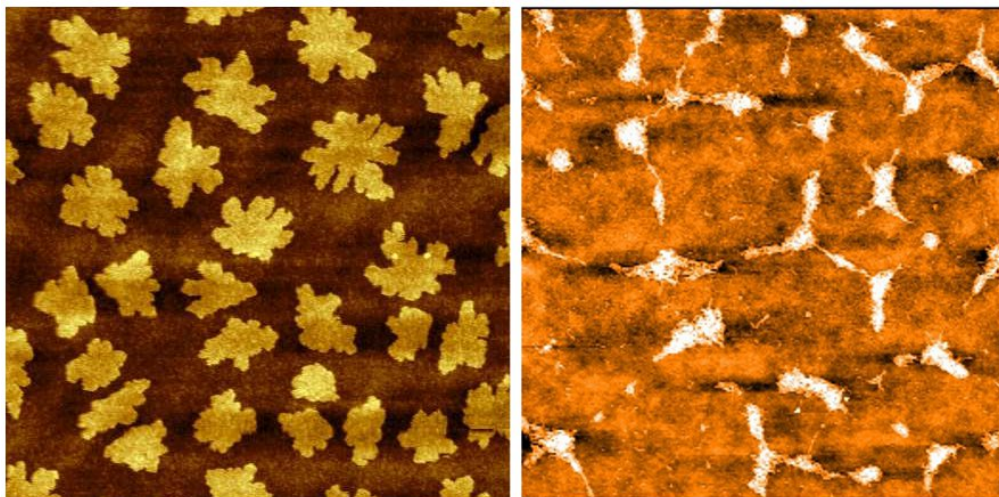
Figure 5.25: AFM height image of vacuum deposited pentacene islands in the sub monolayer regime (left). AFM height image of solution deposited polymer film in the sub monolayer regime (right). Images taken from [31].

to the silicon substrate surface. Such a growth behavior is typical for small molecules growth and reflects the limited diffusion of molecules during the deposition. A molecule that is intially adsorbed at a terrace surface is able to diffuse to a certain extend on top of this terrace. As a terrace edge acts as an diffusion barrier the molecule favors to stay on this terrace and crystallize with other molecules present at the terrace.

As the spin casting process is fast a equilibrium structure is hardly achieved. Therefore it is even more surprisingly that on the time scale of the spincasting process structures similar to vacuum deposited films occur indicating the highly favorable formation of crystalline domains in DH3T. For a more detailed study of the initial nucleation process and the influence of the solvent on the film morphology additional measurements are required with systematic exchange of solvents (with different wetting behavior, vapor pressures and boiling points) and the spin parameters. This will then allow to identify the relevant time scales that are relevant for the film forming process of spin coated thin films. For the use of DH3T in thin film transistor applications, for instance, the film morphology required are fully closed homogeneous layers that allow for a continuous channel formation which can be expected to be achievable with a optimization of the spin casting process.
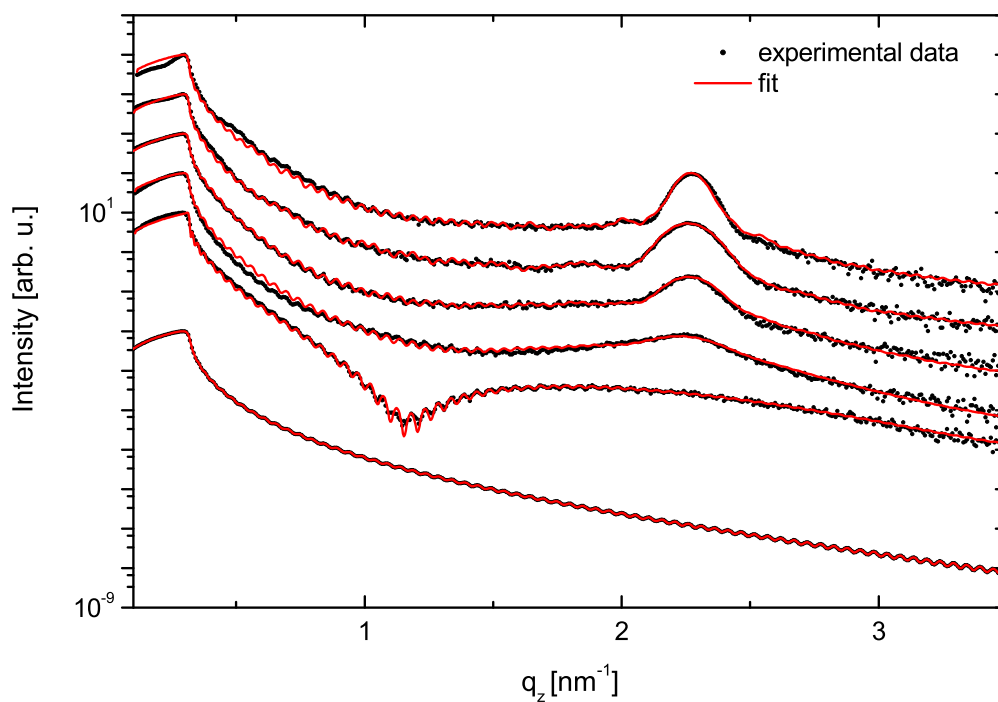
Figure 5.26: As the concentration of DH3T in THF is increased the film morphology changes. The absence of fringes indicate that the initial monolayer formation (second line from bottom) is exchanged by 3 dimensional structures.

(a)   (c)
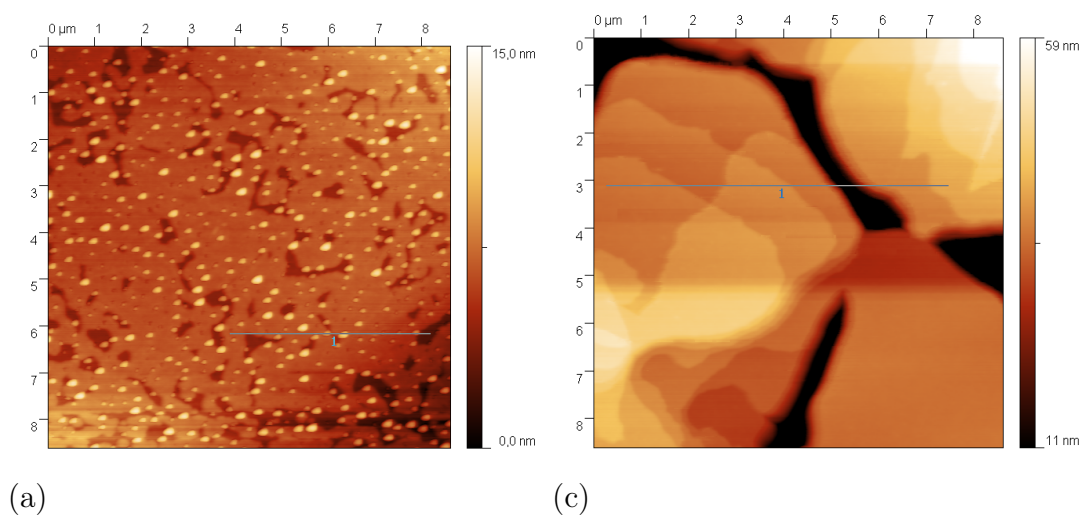
Figure 5.27: AFM images of spincoated thinfilms processed from (a) $0.2\,g/l$ and (b) $2.9\,g/l$ solution.

Chapter 6

Overall Discussion and Conclusion

Polymorphism in organic thin films has large influence to the performance of organic electronic devices, since fine details of the molecular packing change the intermolecular overlap and therefore the electronic band structure considerably [14]. Nearly all prominent organic electronic materials show polymorphism, which is not restricted to polymers or small molecules [8]. Generally, conjugated molecules with flexible units and complex molecular conformation show a large tendency to form different types of crystal structures [2]. But also simple and rigid molecules – like pentacene – can show distinct polymorphism [15].

Several thermodynamic parameters but also kinetic factors influence the formation of polymorph crystal structures in organic thin films [24]. The growth of pentacene on a silicon oxide surface starts with the formation of a monolayer of up-right standing molecules. On top of this monolayer the nucleation of crystals starts [30]. Crystallographic polymorphism appears only due to small differences in the molecular packing like the tilt angle of the molecules or the herringbone angle of the aromatic units [17]. The reason for the formation of a thin film phase is not fully clear. The dependence of its appearance is discussed in terms of substrate temperature during the thin film deposition but also in terms of supersaturation during the thin film growth [20].

The results shown in chapter 5 indicate that preparation speed of films has also a strong impact on the formation of specific polymorph phases. Table 5.10 indicates that at high evaporation rates the s - phase appears, while at low evaporation rates the a–phase and the b-phase is formed. This results suggests two important parameters for the formation of a *thin thin film* phase. One parameter is the presence of a surface during the crystallization process. The other parameter is correlated with the available time for the organic molecules to adapt its proper conformation and align within the crystalline order. This is in principle compareable to low

temperatures of the substrate at physical vapor deposition, where the movement of the crystallites is "frozen" when hitting the substrate [20]. A similar dependence was reported for spincoated conjugated polymeres where the spin speed was varied [12, 8]. Higher spin speed leads to higher evaporation rates during the processing and therefore describes a similar behavior.

Bibliography

[1] Jens Als-Nielsen and Des McMorrow. *Elements of Modern X-ray Physics*. Wiley, 1 edition, January 2001.

[2] Joel Bernstein. *Polymorphism in Molecular Crystals*. Clarendon Press, May 2002.

[3] G. Binnig, C. F. Quate, and Ch. Gerber. Atomic force microscope. *Physical Review Letters*, 56(9):930, March 1986.

[4] Mario Birkholz, Paul F. Fewster, and Christoph Genzel. *Thin film analysis by X-ray scattering*. Wiley-VCH, 2006.

[5] Nicolas Boucher, Julie Leroy, Sergey Sergeyev, Eric Pouzet, Vincent Lemaur, Roberto Lazzaroni, J?r?me Cornil, Yves Henri Geerts, and Michele Sferrazza. Mesomorphism of dialkylterthiophene homologues. *Synthetic Metals*, 159(13):1319–1324, July 2009.

[6] J. G. Calvert. Glossary of atmospheric chemistry terms (Recommendations 1990). *Pure and Applied Chemistry*, 62(11):2167–2219, 1990.

[7] Gerd Czycholl. *Theoretische Festkörperphysik*. Springer Berlin Heidelberg, Berlin, Heidelberg, 2008.

[8] Dean M. DeLongchamp, Brandon M. Vogel, Youngsuk Jung, Marc C. Gurau, Curt A. Richter, Oleg A. Kirillov, Jan Obrzut, Daniel A. Fischer, Sharadha Sambasivan, Lee J. Richter, and Eric K. Lin. Variations in semiconducting polymer microstructure and hole mobility with Spin-Coating speed. *Chemistry of Materials*, 17(23):5610–5612, November 2005.

[9] M. B. Ewing, T. H. Lilley, G. M. Olofsson, M. T. Ratzsch, and G. Somsen. Standard quantities in chemical thermodynamics. fugacities, activities and equilibrium constants for pure and mixed phases (IUPAC recommendations 1994). *Pure and Applied Chemistry*, 66(3):533–552, 1994.

[10] Sunil A. Gupta and Rakesh K. Gupta. A parametric study of spin coating over topography†. *Industrial & Engineering Chemistry Research*, 37(6):2223–2227, June 1998.

[11] N. K. Halder, B. K. Chatterjee, and S. C. Roy. The change of viscosity with concentration of suspended particles and a new concept of gelation. *Journal of Physics: Condensed Matter*, 9:8873, 1997.

[12] X. T. Hao, T. Hosokai, N. Mitsuo, S. Kera, K. K. Okudaira, K. Mase, and N. Ueno. Control of the interchain ?-? interaction and electron density distribution at the surface of conjugated poly(3-hexylthiophene) thin films. *The Journal of Physical Chemistry B*, 111(35):10365–10372, 2007.

[13] IUPAC, A. D. McNaught, and A. Wilkinson. IUPAC. compendium of chemical terminology, 2nd ed. (the "Gold book"). *Blackwell Scientific Publications*, 1997.

[14] Oana D. Jurchescu, Devin A. Mourey, Sankar Subramanian, Sean R. Parkin, Brandon M. Vogel, John E. Anthony, Thomas N. Jackson, and David J. Gundlach. Effects of polymorphism on charge transport in organic semiconductors. *Physical Review B*, 80(8):085201, 2009.

[15] Christine C. Mattheus, Anne B. Dros, Jacob Baas, Auke Meetsma, Jan L. de Boer, and Thomas T. M. Palstra. Polymorphism in pentacene. *Acta Crystallographica Section C*, 57(8):939–941, 2001.

[16] Armin Moser. *Crystal Structure Determination from Two-Dimensional Powders*. Mastersthesis, University of Technology Graz, Institute of Solid State Physics, Graz, 2008.

[17] Dmitrii Nabok, Peter Puschnig, and Claudia Ambrosch-Draxl. Cohesive and surface energies of pi -conjugated organic molecular crystals: A first-principles study. *Physical Review B*, 77(24):245316, June 2008.

[18] Ullrich Pietsch, Václav Holý, and Tilo Baumbach. *High-resolution X-ray scattering from thin films to lateral nanostructures*. Springer, 2004.

[19] Ron Reifenberger and Arvind Raman. *ME 597/PHYS 570: Fundamentals of Atomic Force Microscopy (Fall 2009)*. September 2009.

[20] Ricardo Ruiz, Devashish Choudhary, Bert Nickel, Tullio Toccoli, Kee-Chul Chang, Alex C. Mayer, Paulette Clancy, Jack M. Blakely, Randall L. Headrick, Salvatore Iannotta, and George G. Malliaras. Pentacene thin film growth. *Chemistry of Materials*, 16(23):4497–4508, November 2004.

[21] Ir. R. Rutgers. Relative viscosity and concentration. *Rheologica Acta*, 2(4):305–348, December 1962.

[22] Ingo Salzmann. *Structural order in epitaxially grown oligo-phenylene thin films on metallic surfaces*. PhD thesis, University of Technology Graz, Institute of Solid State Physics, Graz, 2003.

[23] Ingo Salzmann. *Structural and energetic properties of pentacene derivatives and heterostructures*. PhD thesis, Humboldt-Universität zu Berlin, Mathematisch-Naturwissenschaftliche Fakultät I, December 2008. [Online: Stand 2010-11-02T14:32:08Z].

[24] K. Sato. Polymorphic transformations in crystal growth. *Journal of Physics D: Applied Physics*, 26:B77, 1993.

[25] Dieter Schwarzenbach. *Crystallography*. Wiley, 1 edition, April 1997.

[26] U. Shmueli. Reciprocal space in crystallography. In H. Fuess, Th Hahn, H. Wondratschek, U. Müller, U. Shmueli, E. Prince, A. Authier, V. Kopský, D. Litvin, M. Rossmann, E. Arnold, S. Hall, B. McMahon, and U. Shmueli, editors, *International Tables for Crystallography Volume B: Reciprocal space*, volume B of *International Tables for Crystallography*, pages 2–9. Springer Netherlands, 2001. 10.1107/97809553602060000549.

[27] Metin Tolan. *X-Ray Scattering from Soft-Matter Thin Films: Materials Science and Basic Research*. Springer, April 1999.

[28] A. Weill and E. Dechenaux. The spin-coating process mechanism related to polymer solution properties. *Polymer Engineering & Science*, 28(15):945–948, 1988.

[29] Christian Weissmantel and Claus Hamann. *Grundlagen der Festkörperphysik*. Wiley-VCH, 4 edition, January 1999.

[30] O. Werzer, B. Stadlober, A. Haase, M. Oehzelt, and R. Resel. Full x-ray pattern analysis of vacuum deposited pentacene thin films. *Eur. Phys. J. B*, 66(4):455–459, 2008.

[31] Oliver Werzer. *Structure and Morphology of Thiophene based Polymers and Pentacene for organic electronics: an X-ray based study*. PhD thesis, 2007.

[32] P. Yimsiri and M.R. Mackley. Spin and dip coating of light-emitting polymer solutions: Matching experiment with modelling. *Chemical Engineering Science*, 61(11):3496–3505, June 2006.

Deutsche Fassung:
Beschluss der Curricula-Kommission für Bachelor-, Master- und Diplomstudien vom 10.11.2008
Genehmigung des Senates am 1.12.2008

EIDESSTATTLICHE ERKLÄRUNG

Ich erkläre an Eides statt, dass ich die vorliegende Arbeit selbstständig verfasst, andere als die angegebenen Quellen/Hilfsmittel nicht benutzt, und die den benutzten Quellen wörtlich und inhaltlich entnommene Stellen als solche kenntlich gemacht habe.

Graz, am …………………………… 10.11.2010   …………………………………………..
                                                    (Unterschrift)

Englische Fassung:

STATUTORY DECLARATION

I declare that I have authored this thesis independently, that I have not used other than the declared sources / resources, and that I have explicitly marked all material which has been quoted either literally or by content from the used sources.

10.11.2010
…………………………   …………………………………………..
        date   (signature)